博士論文

Experimental Study on the Rare Decays
$K_L^0 \to \mu e$ and $K_L^0 \to ee$

（稀崩壊 $K_L^0 \to \mu e$ 及び $K_L^0 \to ee$ の実験的研究）

赤城　卓

平成３年

(1)

Experimental Study on the Rare Decays $K_L^0 \to \mu e$ and $K_L^0 \to ee$

(稀崩壊$K^0_L \to \mu e$及び $K^0_L \to ee$の実験的研究)

Department of physics, Tohoku University

Takashi Akagi

Doctor of Scinece

1991

Abstract

We have searched for the rare decays $K_L^0 \to \mu e$ and $K_L^0 \to ee$ using the K0 beam line of the KEK 12GeV Proton Synchrotron. The K_L^0 decays were observed with a detector consisting of two symmetric arms along the beam line. Each arm consisted of a spectrometer and particle identification counters. The $K_L^0 \to \pi^+\pi^-$ decay events were acquired simultaneously using the same detector for normalization. Track candidates were reconstructed in the off-line analysis. In order to eliminate pions decaying to muons in the spectrometer and reject the background unassociated with K_L^0 decays, selection criteria for track and event qualities were applied to the reconstructed events. Particle identification was further applied to the all selected events. The sensitivities for the decays $K_L^0 \to \mu e$ and $K_L^0 \to ee$ were determined by the number of $K_L^0 \to \pi^+\pi^-$ events correcting for the acceptance differences obtained from a Monte Carlo calculation, the particle identification efficiencies calibrated using the semileptonic K_L^0 decays, the pion absorption rate, and the dead time difference.

We observed no $K_L^0 \to \mu e$ event in the fiducial region. Thus, the upper limit of the $K_L^0 \to \mu e$ branching ratio at the 90% confidence level was determined to be 9.4×10^{-11} with a systematic error of 3%. A few background events near to, but outside the fiducial region came from the decay $K_L^0 \to \pi e \nu$ with the pion decaying to a muon in the spectrometer, whose influence on the fiducial region was sufficiently small at the sensitivity of this experiment. There was one ee event in the fiducial region. The event was at the tail end of the background distribution which mainly came from the decay $K_L^0 \to e^+e^-e^+e^-$ and could not be distinguished from it at a sensitivity level of one event. Therefore, the upper limit of the $K_L^0 \to ee$ branching ratio at the 90 % confidence level was determined to be 1.6×10^{-10}.

Contents

Introduction

At present, the Standard Model is the most reliable theory in particle physics which describes the strong and electroweak interactions between three (or more) identical generations of quarks and leptons. All experimental results obtained so far agree with the predictions of the Standard Model. However, there are several problems which cannot be solved by the Model, the number of generations, quark mixing angles, the origin of fermion masses, and the gauge hierarchy problem. They must be introduced as the parameters by hand and be determined by experiments. Many physicists have proposed many new models to solve the problems. Some of these models predict a lepton flavor changing process for rare K decay, $K_L^0 \to \mu e$ at an experimental sensitivity of 10^{-11} while it is forbidden in the Standard Model at the sensitivity level of 10^{-25}. Therefore, the observation of the lepton flavor changing process, $K_L^0 \to \mu e$ may lead one to introduce a new model beyond the Standard Model, such as the Horizontal gauge model.

From this potential interests in the K physics, we have performed an experiment to search for the decay $K_L^0 \to \mu e$ using the 12-GeV proton synchrotron at National Laboratory for High Energy Physics (KEK). The experiment is called E137, and 17 members collaborated from 4 institutes, KEK, University of Tokyo, Kyoto University and Tohoku University. This experiment was proposed and approved in 1985. The first engineering run was carried in 1987, and the physics run started in 1988 and ended in 1990. This thesis is written based on the entire data set taken from 1988 to 1990.

This thesis is organized as follows: In chapter 1, the author describes why a search for the decay $K_L^0 \to \mu e$ is interesting. Experimental apparatus is explained in chapter 2. In chapter 3, data analysis of how to find and fit tracks and determine the criterion of particle identification is described. In chapter 4, sensitivities of $K_L^0 \to \mu e$ and $K_L^0 \to ee$ are derived, and results on $K_L^0 \to \mu e$, ee and $\mu\mu$ are shown. The background source and limit

to $K_L^0 \to \mu e$ and $K_L^0 \to ee$ are discussed in chapter 5. Finally, in chapter 6, conclusion is given and future prospects are discussed.

Chapter 1

Physical Background

1.1 Physics Motivation

The lepton flavor changing process, $K_L^0 \rightarrow \mu e$ is forbidden by the Standard Model with massless neutrinos. Even if neutrinos are not massless and lepton generations have mixing like quarks, the decay $K_L^0 \rightarrow \mu e$ at the one loop level as shown in Figure 1.1 is highly suppressed to the order of 10^{-26}[1] due to the current upper limits on the masses of the three neutrinos. Even with the assumption of a massive neutrino for the fourth generation, the decay is estimated to be the order of 10^{-25}[1], which is far below the experimentally possible sensitivity. Therefore, the observation of the decay $K_L^0 \rightarrow \mu e$ at a sensitivity of 10^{-11} provides evidence for new models, such as the Left-right symmetric model[1][2], new interactions among generations[3], the technicolor model[4] and the composite model[5]. All of these models predict the branching ratio of the decay $K_L^0 \rightarrow \mu e$ might be as large as 10^{-11} to 10^{-12} as summarized in Table 1.1, and the

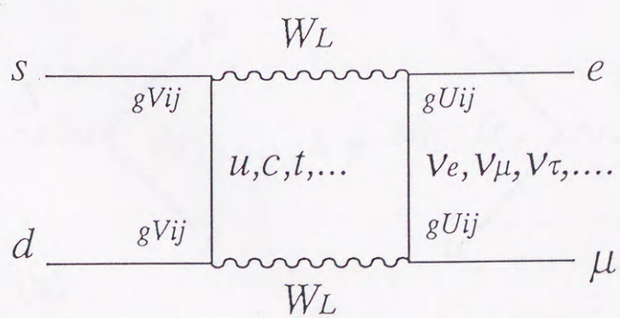

Figure 1.1: The decay $K_L^0 \rightarrow \mu e$ via neutrino mixing in the Standard Model. V_{ij} and U_{ij} denote the mixing matrix elements of the quarks and leptons, respectively.

models	predictions
Left-right symmetric model	$< 2 \times 10^{-13}$
Multi Higgs doublets	$10^{-13} \sim 10^{-10}$
Horizontal gauge symmetry	$> 10^{-10}$
Extend Technicolor theory	$10^{-12} \sim 10^{-11}$
Composite models	$\sim 10^{-11}$
supersymmetry and superstring	possible

Table 1.1: The branching ratios of $K_L^0 \to \mu e$ predicted by non-standard models

outlines of these models are given in Appendix A.

When we take the horizontal gauge symmetry[6] as the simplest model for example, the decay $K_L^0 \to \mu e$ can be induced by a new gauge boson which connects the first and second generations as shown in Figure 1.2(a). Using this scheme, we can estimate the gauge boson mass mediating the decay $K_L^0 \to \mu e$. In order to compensate uncertainties from effects of the strong interaction in the decay process, we compare the decay $K_L^0 \to \mu e$ to the weak decay $K^+ \to \mu^+ \nu$ caused by the weak boson as shown in Figure 1.2(b). Here we assume the $V - A$ coupling from the two possible coupling types−pseudoscalar type and $V - A$ type. If we neglect the mass difference between K_L^0 and K^+ and the electron mass, the phase space factor is the same for the decay width (Γ) of two diagrams. Then, the ratio of the two decay widths can be written as follows;

$$\frac{\Gamma(K_L^0 \to \mu e)}{\Gamma(K^+ \to \mu\nu)} = \frac{(g_X^2/M_X^2)^2}{(g_W^2 \sin\theta_c/M_W^2)^2} , \tag{1.1}$$

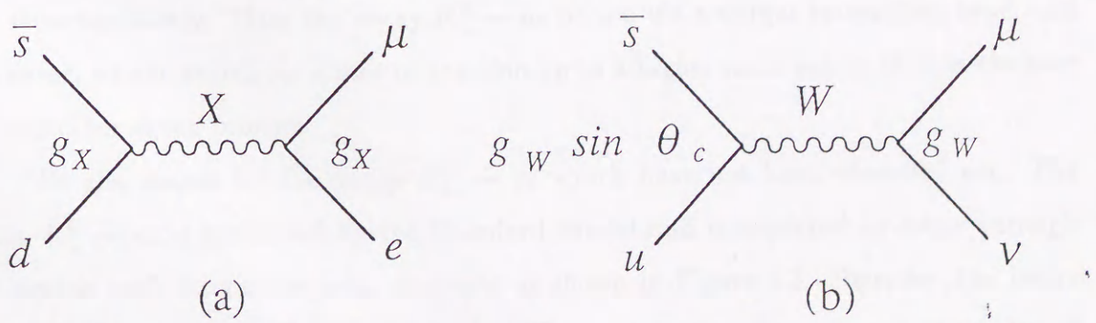

Figure 1.2: Comparison of the decays (a)$K_L^0 \to \mu e$ via a new interaction and (b)$K^+ \to \mu^+ \nu$ via the weak interaction.

where g and M stand for the coupling constants and masses, and the subscripts W and X denote the weak interaction and the new interaction, respectively. The θ_c is the Cabibbo mixing angle between s and d quark. Using the relations of the branching ratio (B), the lifetime (τ) and the decay width (Γ), $B = \tau\Gamma$, M_X is obtained by

$$M_X = 221TeV \cdot \frac{g_X}{g_W} \cdot \left(\frac{10^{-12}}{B(K_L^0 \to \mu e)} \right)^{1/4}, \tag{1.2}$$

where $B(K^+ \to \mu\nu) = 63.5\%$, $\tau(K_L^0)/\tau(K^+) = 4.19$, $\sin\theta_c = 0.220$ and $M_W = 81.0GeV$ are used. With the assumption of $g_X \simeq g_W$, the observation of $K_L^0 \to \mu e$ at a sensitivity of 1×10^{-11} would require a mass of $124TeV$ for the horizontal gauge boson. It should be noted that searching for the decay $K_L^0 \to \mu e$ to a sensitivity of 10^{-11} is equivalent to searching for effects of a new particle with the mass of $100TeV$ which cannot be directly produced by any existing or planned accelerators.

We can also consider other lepton flavor changing processes in μ decays such as $\mu^+ \to e^+\gamma$, $\mu^+ \to e^+e^-e^+$ and $\mu^+e^- \to \mu^-e^+$. Upper limits of their branching ratios could put a constraint on the mass of the horizontal gauge boson. However, it should be noticed that the type of interaction in the μ decays is different from that in the decay $K_L^0 \to \mu e$. If a generation number is assigned to each of the three generation[6], the net generation number in μ decays is not conserved, while it is in the decay $K_L^0 \to \mu e$. There is another possible lepton flavor changing process in K decays, $K^+ \to \pi^+\mu^+e^-$. It is similar to the decay $K_L^0 \to \mu e$ in conserving the net generation number in the decay process, but it differs in the type of coupling. The decay $K^+ \to \pi^+\mu^+e^-$ can occur through the V coupling. However, the gauge boson mass estimated from the observation of the decay $K^+ \to \pi^+\mu^+e^-$ is two-thirds as large as that from the decay $K_L^0 \to \mu e$ at the same sensitivity. Thus, the decay $K_L^0 \to \mu e$ occurs via a unique interaction type, and moreover, we can search for a new interaction up to a higher mass region than is the case for any other decay process.

We also search for the decay $K_L^0 \to ee$ which have not been observed yet. The decay $K_L^0 \to ee$ is permitted by the Standard Model and is expected to occur through the electro-weak interaction with diagrams as shown in Figure 1.3. However, the decay rate for $K_L^0 \to ee$ is smaller than that for $K_L^0 \to \mu\mu$ by roughly a factor of $(m_e/m_\mu)^2$ due to the helicity suppression. The branching ratio of the decay $K_L^0 \to ee$ is predicted to be the order of 10^{-12}[7] using the branching ratio of the decay $K_L^0 \to \mu\mu$. Therefore,

a positive signal for the decay $K_L^0 \to ee$ at the sensitivity of the order of 10^{-11} would imply the existence of a new interaction which includes a mechanism to avoid the helicity suppression such as is the case for the left-right symmetric model (Figure 1.4).

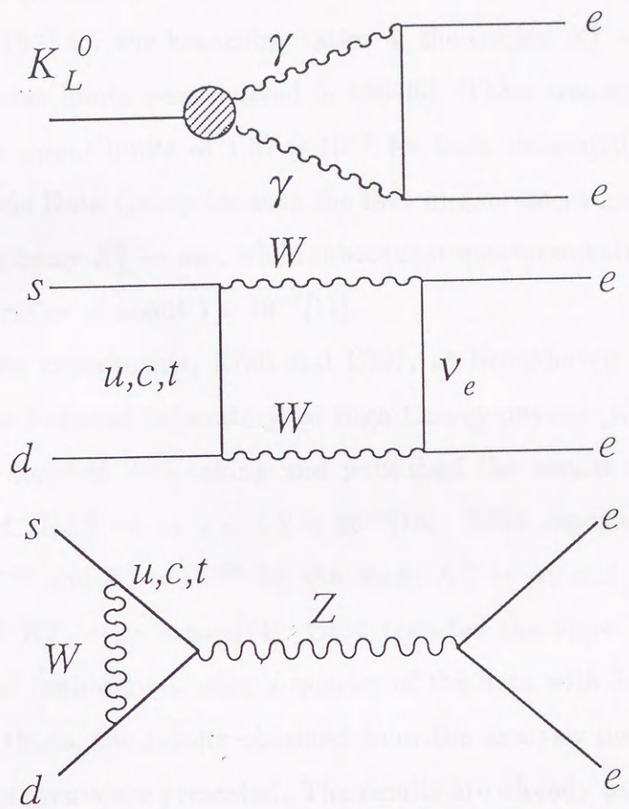

Figure 1.3: $K_L^0 \to ee$ via the electroweak interaction.

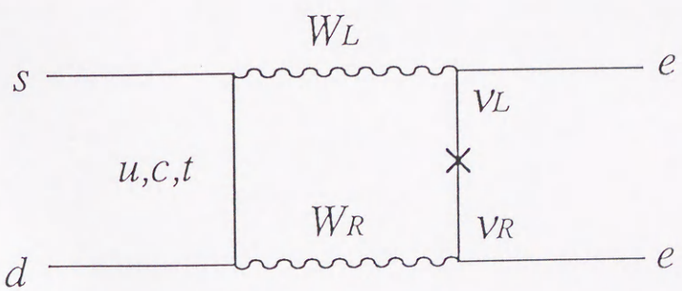

Figure 1.4: The decay $K_L^0 \to ee$ in the left-right symmetric model.

1.2 Previous Experiments

There were several experiments to search for the decay $K_L^0 \to \mu e$ and $K_L^0 \to ee$. Figure 1.5 shows the upper limits for $K_L^0 \to \mu e$ given by the previous experiments as a function of time (in years). The Particle Data Group in 1986 gives upper limits of 6×10^{-6} and 2×10^{-7} for the branching ratios of the decays $K_L^0 \to \mu e$ and $K_L^0 \to ee$, respectively[8]. These limits were derived in 1967[9]. There was an experiment in 1971 which reported an upper limits of 1.57×10^{-9} for both decays[10], but they were not cited by the Particle Data Group because the first measurement gave the upper limit of 1.82×10^{-9} for the decay $K_L^0 \to \mu\mu$, while subsequent measurements had obtained values for the branching ratios of about 1×10^{-8}[11].

In 1980's, two experiments, E780 and E791, at Brookhaven National Laboratory (BNL) and E137 at National Laboratory for High Energy physics (KEK) were performed. E780 has already finished data-taking and published the results of $B(K_L^0 \to \mu e\ ) < 1.9 \times 10^{-9}$[12] and $B(K_L^0 \to ee\ ) < 1.2 \times 10^{-9}$[13]. E791 reported in 1989 the upper limits of 2.2×10^{-10} and 3.2×10^{-10} for the decay $K_L^0 \to \mu e$ and $K_L^0 \to ee$ using their 1988 data with 87 $K_L^0 \to \mu\mu$ events[14]. E137 reported the upper limits of 4.2×10^{-10} and 5.4×10^{-10} for both decays using a quarter of the data with 54 $K_L^0 \to \mu\mu$ events in 1989[15]. In this thesis, the results obtained from the analysis the entire data of E137 with 179 $K_L^0 \to \mu\mu$ events are presented. The results are already published in Ref.[16].

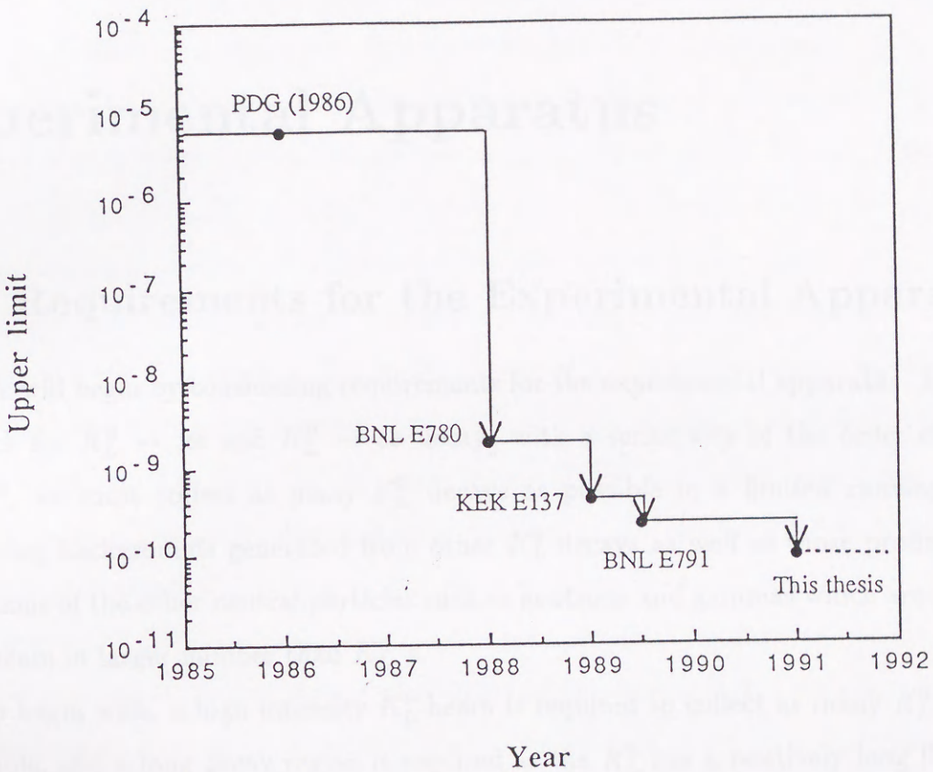

Figure 1.5: History of upper limits for $K_L^0 \to \mu e$ branching ratio

Chapter 2

Experimental Apparatus

2.1 Requirements for the Experimental Apparatus

We will begin by considering requirements for the experimental apparatus. In order to search for $K_L^0 \to \mu e$ and $K_L^0 \to ee$ decays with a sensitivity of the order of 10^{-11} to 10^{-12}, we must collect as many K_L^0 decays as possible in a limited running time, suppressing backgrounds generated from other K_L^0 decays as well as those produced by interactions of the other neutral particles such as neutrons and gammas which are present in the beam in larger number than K_L^0 's.

To begin with, a high intensity K_L^0 beam is required to collect as many K_L^0 decays as possible, and a long decay region is required as the K_L^0 has a relatively long life time with $c\tau = 15.5m$. Furthermore, the detector should have a large acceptance for detecting decay particles. These requirements lead to a high counting-rate environment for the detector with a large sensitive area. Then, each detector element needs to have a high-speed response and to be subdivided into small segments to decrease the counting rate of each counter. The electronics also should have an excellent timing resolution to reduce the rate of accidental coincidences. A simple and effective triggering scheme is needed to record rare decay candidates selectively and to reject the dominant decay modes such as semileptonic K_L^0 decays. In spite of these precautions, the number of triggers and the data size are still large, and a high-speed online data-taking system including a fast online computer is desirable.

A high intensity K_L^0 beam includes a large number of neutral particles such as neu-

trons and gammas. They would produce hadrons interacting with gas atoms in the decay chamber and lead to undesired background to K_L^0 decays. Therefore, the neutral particle beam should be well collimated along the beam line to suppress them. Furthermore, the neutral particles produce accidental hits in the detectors due to interactions. Then, a good collimator system and a two arm detector system with a gap for the beam pipe, through which the neutral particles pass downstream, are desirable. The well collimated beam is led downstream by a beam pipe thus escaping the detector system.

Next, we must design our detectors to suppress backgrounds to the decay $K_L^0 \to \mu e$. The major source of background for $K_L^0 \to \mu e$ is the decay $K_L^0 \to \pi e \nu$, the branching ratio of which is 38.7%. Most of the events due to this mode have low πe effective mass and large missing momentum due to the finite momentum of the neutrino, but in the limit $p_\nu \to 0$, the πe effective mass approaches the K_L^0 mass. There are two main processes contributing from this source. One is the case in which the pion is misidentified as a muon. Due to the misidentification, the effective mass of the μe system in the limit $p_\nu \to 0$ should be less than the K_L^0 mass minus $16 MeV/c$. Other background comes from the decay $K_L^0 \to \pi e \nu$ followed by the decay $\pi \to \mu \nu$. In the limit that the muon is boosted in the forward direction, the effective mass of μe should be less than the K_L^0 mass minus $8.4 MeV/c$. In order to eliminate such backgrounds, an excellent mass resolution is required. In the present experiment, it is essential to reduce the material in the spectrometer as much as possible, because the particle momentum is relatively low and the effect of multiple Coulomb scattering is dominant in the resolution.

There are two rare, but severe, background sources which can give μe effective masses close to the K_L^0 mass. One of these is $K_L^0 \to \pi e \nu$ followed by $\pi \to \mu \nu$ decay. This may be a problem if a pion decays in the magnet and emits a muon in the direction opposite to the momentum kick leading to mismeasurement of the track momentum, and the effective mass of μe may come close to the K_L^0 mass. In order to remove this background, it is essential to measure the momentum of the track redundantly, and a double-stage spectrometer system is desirable. Another possible background source is double misidentification for the decay $K_L^0 \to \pi e \nu$. If the pion is misidentified as an electron and the electron is misidentified as a muon, the effective mass of μe can fall on the K_L^0 mass. Good particle identification, in particular electron identification, is required

to reject this higher order background.

Finally we must know the sensitivities for the decays $K_L^0 \to \mu e$ and $K_L^0 \to ee$. There is a useful decay mode, $K_L^0 \to \pi^+\pi^-$, which has a branching ratio of 0.203%. Since the decay $K_L^0 \to \pi^+\pi^-$ has similar kinematics to the decays $K_L^0 \to \mu e$ and $K_L^0 \to ee$, they are collected simultaneously using the same detector system. Therefore, they should have similar detection efficiencies, and most of the systematic uncertainties in detection efficiencies could be cancelled by taking ratios between the yields of the decays $K_L^0 \to \mu e$ or ee and those of the decay $K_L^0 \to \pi^+\pi^-$. Moreover, we can obtain sufficiently large number of $K_L^0 \to \pi^+\pi^-$ events with a sensitivity of the order of 10^{-11} to check the tracking efficiency, the resolution, and so on.

2.2 Neutral Beam Line

This experiment was carried out using a neutral beam line, K0, which was newly constructed for this experiment in the East Counter Hall of KEK 12GeV Proton Synchrotron (KEK-PS). A layout of the beam line in the counter hall is shown in Figure 2.1. Figure 2.2 shows an elevated view of the K0 beam line. The primary proton beam was extracted from the main ring during $0.5sec$ in every cycle of $2.6sec$ length. Neutral beams were produced at 0 degree to the primary proton beam for the first three quarters of the running period (0° production), and at 2 degrees for the last quarter period (2° production). The average intensity of the primary proton beam impinging on a copper target $120mm$ long and $10mm$ in diameter was about 1.2×10^{12} protons per pulse (ppp) for 0° production and 2.0×10^{12} ppp for 2° production. The intensity was monitored by the secondary emission chamber (SEC) in front of the Cu target. Primary protons and secondary charged particles were swept out in the vertical direction by four bending magnets called B23, 24, 25, and 26. The vertical plane was chosen as the bending plane of the magnet since the spectrometer system was set in the horizontal plane, thus minimizing the background. The beam dump was made of tungsten and brass blocks and placed in the lower part of the gap of the third magnet B25.

The produced neutral beams were collimated by two brass collimators and transmitted to the vacuum decay chamber. The first collimator was set in the third bending magnet and limited the neutral beam to a $7mrad$ angle. The solid angle of the beam was

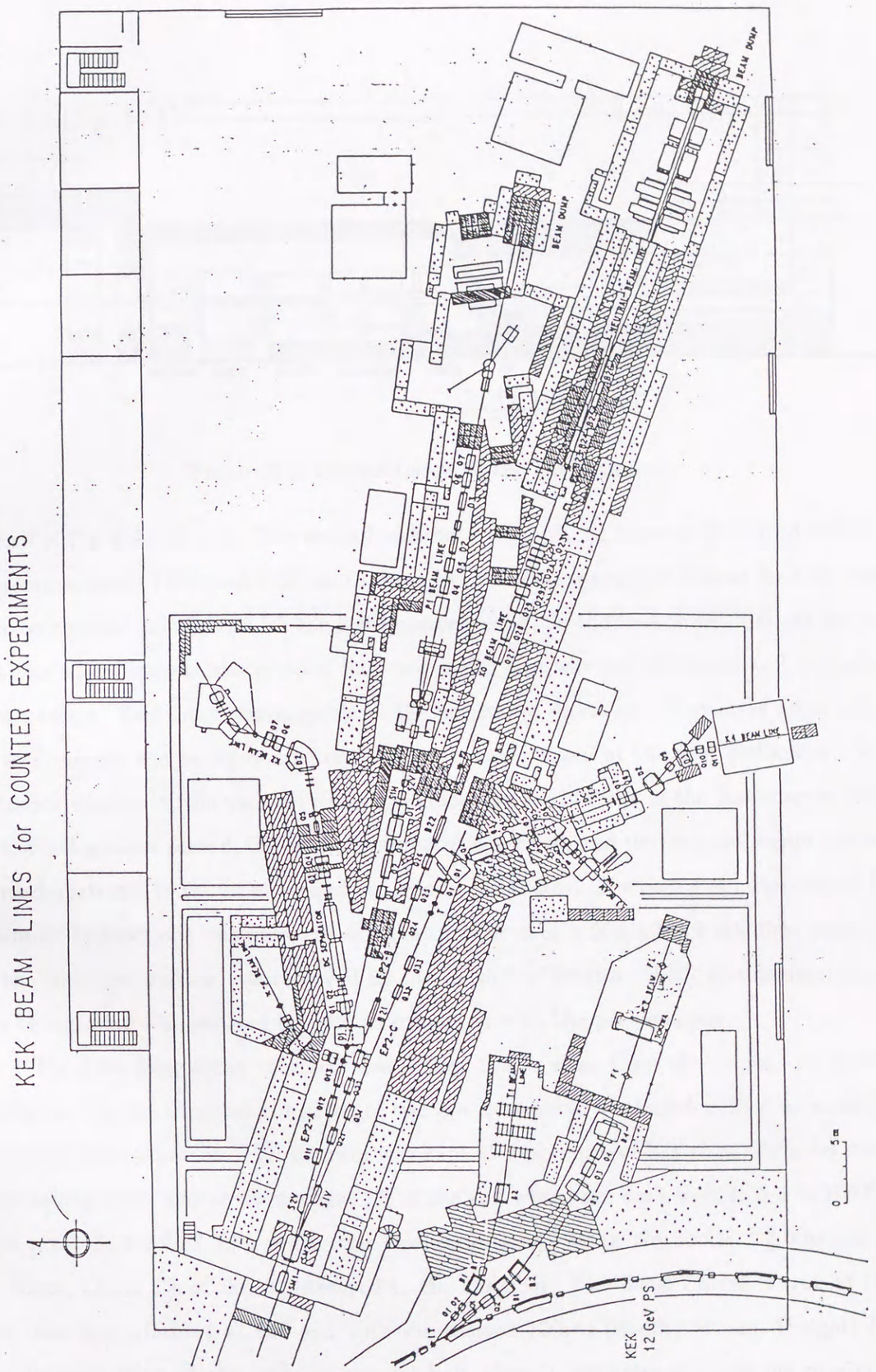

Figure 2.1: Layout of the beam line in the east experimental hall at the KEK PS.

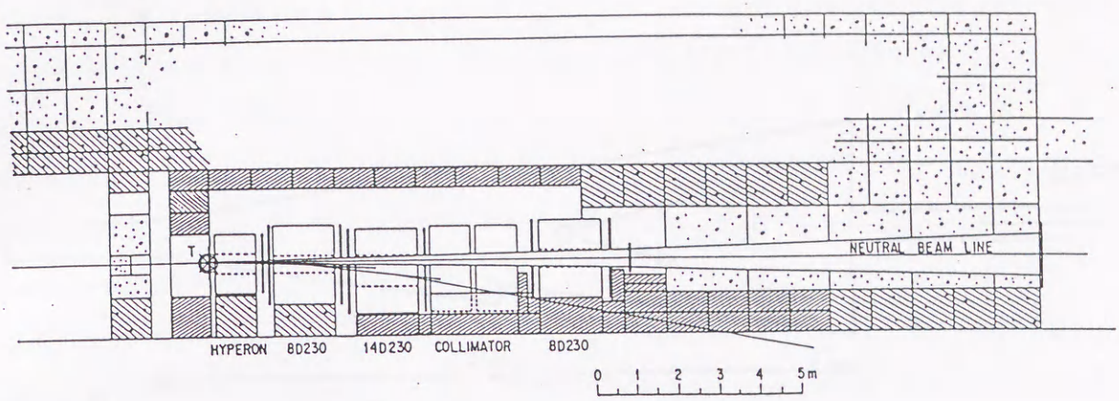

Figure 2.2: Elevated view of the K0 beamline.

then $7 \times 7 \times \pi = 154 \mu str$. The second collimator was placed between the third and last bending magnets (B25 and B26) and subtended a half-cone angle of $9 mrad$ for first three quarters period and $7 mrad$ for the last quarter period. In the first three quarters period, the second collimator was divided into two parts; one was set upstream and the other downstream. Each part was movable in the horizontal direction. They were adjusted so as to minimize the background from the beam halo caused at the first collimator. The entrance window of the vacuum decay chamber was set in front of the last magnet B26. In the last quarter period, the second collimator was fixed, and the vacuum region was extended upstream to the front face of the second collimator. The background produced by beam-air interactions was reduced, and that produced at a $50 \mu m$ thick stainless steel foil of the entrance window was removed by the second collimator. With this configuration, the background was reduced by 30% as compared with the previous one.

The $10m$ long decay chamber was placed $10.5m$ away from the target. As shown in Figure 2.3, the chamber consisted of two $5m$ long parts connected with a hook-shape to reduce halo neutrons. The vacuum was kept at a pressure of less than $50 Pa$ for most data-taking time, except for the first 7% of the run where the data were taken at $100 Pa$. The pressure reached $4 Pa$ under the best conditions. With the mean K_L^0 lifetime of $51.7 nsec$, about 8% of the K_L^0 decayed in the chamber. The decay chamber has, at the end, two exit windows at the end with dimensions $100 cm$ (width) $\times 76 cm$ (height) for the decaying K_L^0 particles and one circular hole $40 cm$ in diameter to allow the surviving

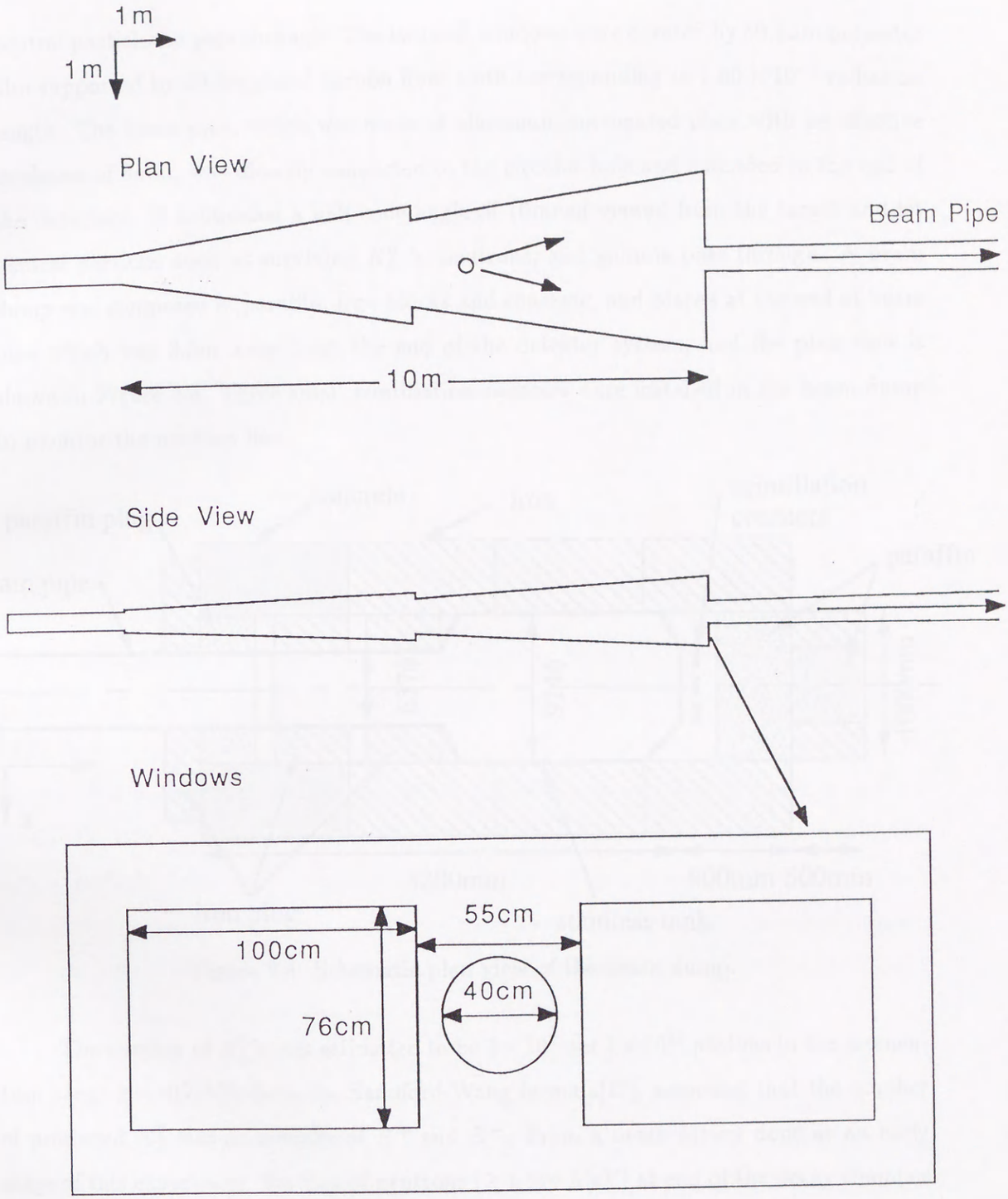

Figure 2.3: Schematic view of the vacuum decay chamber.

neutral particles to pass through. The two exit windows were covered by $50.8\mu m$ polyester film supported by $60.8mg/cm^2$ carbon fiber cloth corresponding to 1.60×10^{-3} radiation length. The beam pipe, which was made of aluminum corrugated plate with an effective thickness of $5mm$, was directly connected to the circular hole and extended to the end of the detectors. It subtended a half-cone angle of $10mrad$ viewed from the target and let neutral particles such as surviving K_L^0 's, neutrons, and gamma pass through. A beam dump was composed of paraffin, iron blocks and concrete, and placed at the end of beam pipe which was $3.5m$ away from the end of the detector system, and the plan view is shown in Figure 2.4. Three small scintillation counters were installed in the beam dump to monitor the neutron flux.

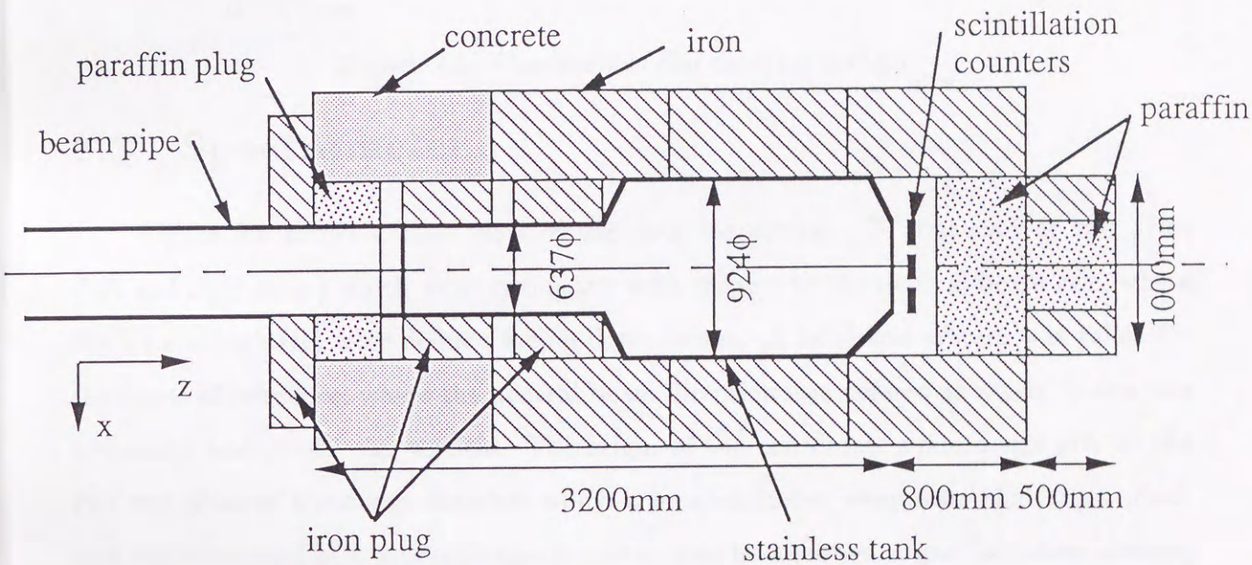

Figure 2.4: Schematic plan view of the beam dump.

The number of K_L^0's was estimated to be 3×10^7 per 1×10^{12} protons in the momentum range $2 \sim 8GeV/c$ from the Sandford-Wang formula[17], assuming that the number of produced K_L^0 was an average of K^+ and K^-. From a beam survey done at an early stage of this experiment, the flux of neutrons ($\geq$ a few MeV) at end of the decay chamber was measured to be $(4 \sim 10) \times 10^8/10^{12}$protons and the flux of high-energy gammas ($\geq$ 100MeV) to be $4 \times 10^8/10^{12}$protons.

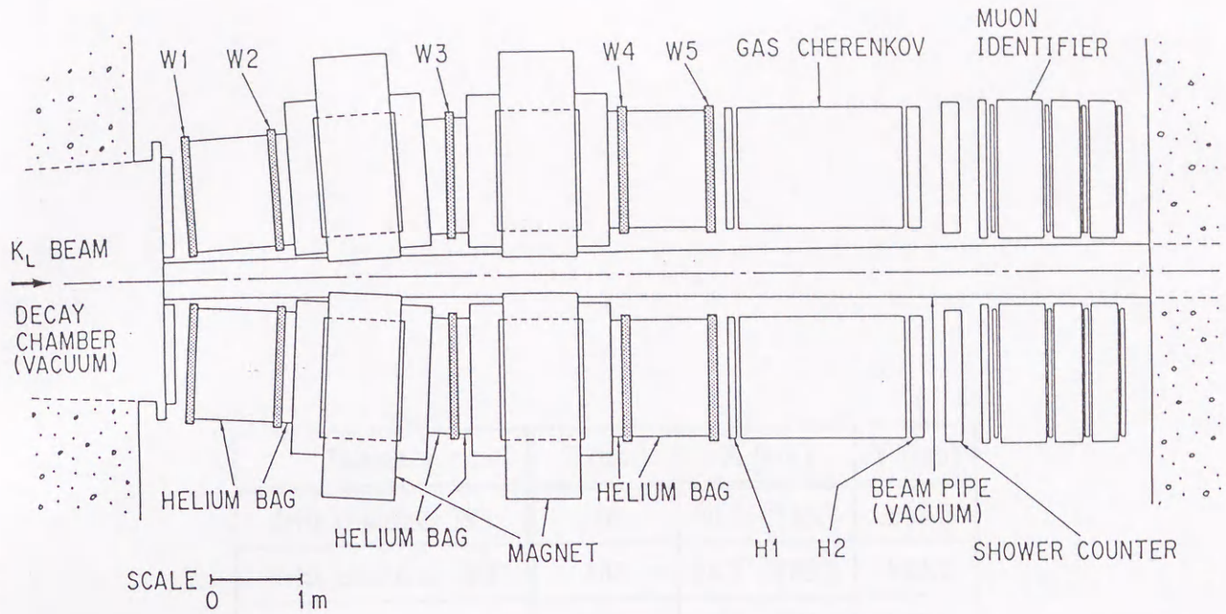

Figure 2.5: Plan view of the detector system.

2.3 Spectrometer

Figure 2.5 shows a plan view of the detector system. It consisted of two arms (left and right arms) which were symmetric with respect to the neutral beam line, where left(L) and right(R) were defined facing downstream. A left-hand system was taken for the frame of reference, where the neutral beam direction was defined as z-axis, x-axis was horizontal and y-axis was vertical. The origin of the coordinate system was put on the exit end plane of the decay chamber which is located $20.5m$ away from the target. Each arm was composed of a magnetic spectrometer, two hodoscopes, a gas Čerenkov counter, an electromagnetic shower counter, and a muon identifier. Table 2.1 gives the z position and x-y coordinates covered by each detector element.

The spectrometer had two magnets and five drift chambers. In order to minimize the multiple scattering by material in the spectrometer, the four spaces between the drift chambers are filled with helium bags which were made of $65\mu m$ thick aluminized polyethylene film. The total radiation length up to W5 was 9.97×10^{-3} including the exit window of the decay chamber. Table 2.2 shows the radiation length and nuclear interaction length for the detector elements.

Detector	Z (cm)	X (cm)	Y (cm)
drift chamber W1	40	30.5 - 145.7	±43.2
drift chamber W2	135	35.7 - 150.9	±43.2
upstream magnet	225	44.2 - 174.2	±50.0
drift chamber W3	320	49.7 - 164.9	±57.6
downstream magnet	415	47.5 - 177.5	±50.0
drift chamber W4	505	54.7 - 169.9	±57.6
drift chamber W5	600	54.7 - 169.9	±57.6
hodoscope H1	620	54.9 - 170.1	±57.6
gas Cherenkov CH	646 - 812	47.4 - 177.6	±75.1
hodoscope H2	820	52.5 - 172.5	±70.0
shower counter EM	850 - 868	48.3 - 176.7	±76.0
muon identifier MU1	900	45.0 - 177.0	±81.0
muon identifier MU2	962	45.0 - 177.0	±81.0
muon identifier MU3	1003	41.0 - 181.0	±84.0
muon identifier MU4	1044	41.0 - 181.0	±84.0

Table 2.1: Setup of detectors.

Material	Radiation length (10^{-3})	Nuclear interaction length (10^{-3})	Nuclear collision length (10^{-3})
decay chamber ($< 0.4\ Torr$, $10\ m$)	< 0.017	< 0.007	< 0.010
exit window	1.60	0.79	1.13
air ($23\ cm$)	0.76	0.31	0.45
drift chamber W1	1.08	0.27	0.39
helium bag	0.44	0.39	0.53
drift chamber W2	1.08	0.27	0.39
helium bag	0.61	0.64	0.85
drift chamber W3	1.08	0.27	0.39
helium bag	0.61	0.64	0.85
drift chamber W4	1.08	0.27	0.39
helium bag	0.44	0.39	0.53
drift chamber W5	1.17	0.31	0.45
Total	< 9.97	< 4.56	< 6.35

Table 2.2: Radiation length, nuclear interaction length, and nuclear collision length up to W5

2.3.1 Magnet

The four dipole magnets were identical, and the aperture was $1.3m \times 1m$. The center of the first one in each arm was placed at $z = 2.15m$ with an inclination of $50mrad$ and the second was set at a distance of $1.9m$ from the first. All magnets had the same field and same polarity such that a negative particle in the left arm or a positive one in the right arm would have to be bent inward to be detected. The total integrated field strength was $0.79Tm$ in each arm, corresponding to a transverse momentum kick of $238MeV/c$. The maximum transverse momenta for the decays $K_L^0 \rightarrow \mu\mu$, $K_L^0 \rightarrow \mu e$ and $K_L^0 \rightarrow ee$ are 225, 238 and 249, respectively. Therefore, the momentum directions of leptons decaying in the direction nearly transverse to the K_L^0 beam were almost parallel to the z-axis after traversing the magnetic field. The three dimensional magnetic field was carefully measured in meshes of intervals of $5cm$ in x, y and z coordinates over the spectrometer area using Hall probes after setting up the magnet system. The probe was temperature-controlled to maintain a measurement accuracy of less than $1Gauss$. Figure 2.6 shows the y-component of the field at the center of the magnet aperture as a function of the z coordinate. During the data acquisition, the field strength at the pole face in each magnet was monitored by a Nuclear Magnetic Resonance (NMR) flux-meter and kept constant to within 0.03%.

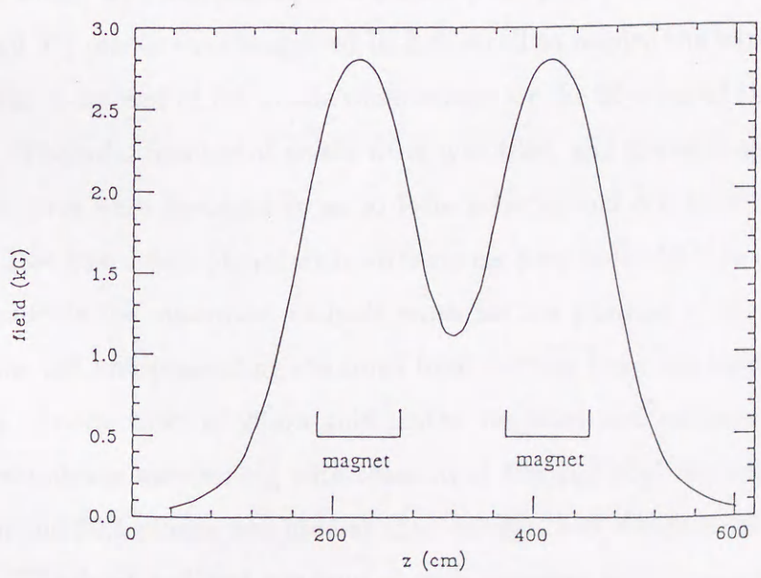

Figure 2.6: Y-component of the measured magnetic field at the center of the magnet aperture as function of the z-coordinate.

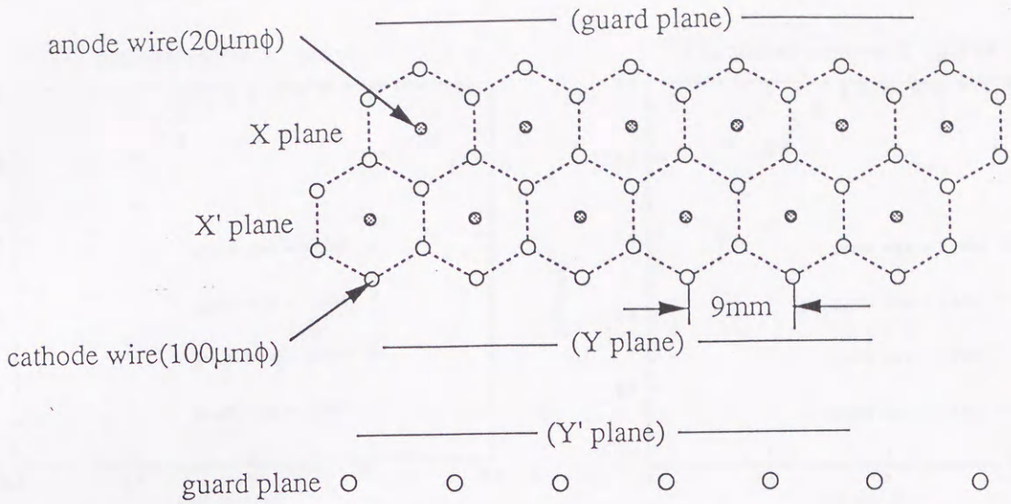

Figure 2.7: Schematic view of the cell structure of the drift chamber.

2.3.2 Drift Chamber

Five drift chambers (W1-W5) were installed in each arm. W1 and W2 were placed in front of the first magnet with an inclination of $50mrad$. W3 was set between two magnet, and W4 and W5 were placed after the second magnet without inclination. The first two drift chambers had dimensions of $1152mm \times 864mm$, and the others $1152mm \times 1152mm$. Each drift chamber had four anode wire planes (X,X',Y,Y') as shown in Figure 2.7. X and X' (Y and Y') planes were staggered by half a cell to resolve the left-right ambiguity. Each plane was composed of 128 anode wires except for the 96 wires of the Y(Y') plane in W1 and W2. The total number of anode wires was 4864, and the wire spacing was $9mm$. The cathode wires were arranged so as to form a hexagonal cell structure around each anode wire. Two guard wire planes with wires strung perpendicularly to anode wires were placed just outside the outermost cathode wires for the purpose of shaping the electric field inside the cell and preventing electrons from drifting from the outside of the cell to the inside it. Anode wires of $20\mu m$ gold-plated tungsten and cathode wires of $100\mu m$ gold-plated aluminum were strung with tensions of $40g$ and $80g$, respectively. A mixture of 50% argon and 50% ethane was used as chamber gas, and the drift velocity were about $50\mu m/nsec$. The front and end windows of each chamber were covered by $25\mu m$ mylar sheet except for the end of W5 covered by $50\mu m$ mylar sheet. The thickness of each drift chamber including wires was 1.08×10^{-3} radiation lengths for W1 to W4 and 1.17×10^{-3}

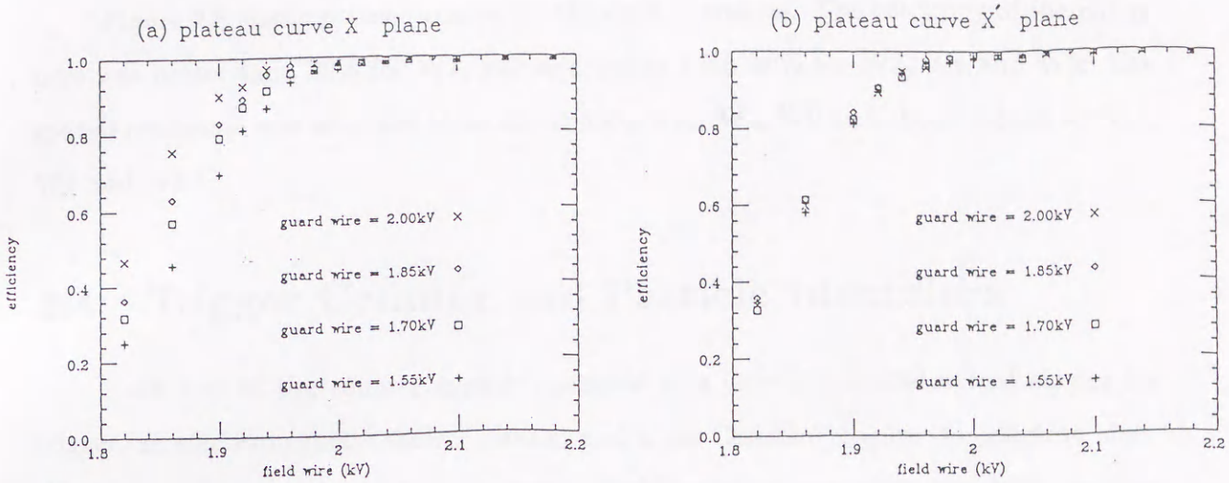

Figure 2.8: Plateau curves of the drift chambers as a function of the field wire voltage and the guard wire voltage for (a)X plane and (b)X' plane.

radiation lengths for W5.

For each of the three chambers W3, W4, and W5 a potential of $-2000V$ was supplied through the cathode wire, while a potential of $50V$ less was supplied for W1 and W2 because of heavier background. A potential of $-1850V$ was supplied to all guard-wires.

The chamber signal from the anode wires was amplified by a pre-amplifier, the gain of which was $12.5mV/\mu A$. Cards, each of which contained pre-amplifiers with 16 channels, were attached to each chamber frame. The amplified signal was transported by $4m$ twisted-pair cables to a 32-channel amplifier-discriminator circuit. The circuit amplified the signal by an additional factor of ten and discriminated it to generate an ECL signal. The threshold voltage for the discriminators was set at $90mV$. The ECL signal was transmitted to a 32-channel TDC module through a $30m$ twisted-pair flat cable. The TDC module was installed in a signal slot in the TKO crate, which was developed at KEK. The signal was delayed by a $300nsec$ delay line on the board and gated during $175nsec$ by a master trigger pulse. It was used to start a TAC (time to amplitude converter). A stop signal was given by the delayed master trigger. The timing edge of the master trigger was defined by the hodoscope signal. The charges held in 32 capacitors were digitized by one ADC chip. They are switched by a multiplexer one after another. The TAC resolution was $0.7nsec$, and the conversion time was $12\mu sec$ per hit.

The digitized data were stacked in memory for readout.

Figure 2.8 shows plateau curves for the drift chambers. The efficiency of the chambers was better than 98% for W1, W2 and better than 99% for W3, W4 and W5. The spatial resolution was obtained to be about $330\mu m$ for W1, W2 and about $280\mu m$ for W3, W4 and W5 [1].

2.4 Trigger Counter and Particle Identifiers

Each arm of the counter system consisted of a pair of scintillator hodoscopes for trigger, an electromagnetic shower counter and a gas Čerenkov counter for electron identification, and a muon identifier. Since the single counting rates were very high, booster voltages were supplied to the last two or three dynode stages of every photomultiplier except for the Čerenkov counter.

2.4.1 Hodoscope

The hodoscopes were used for generating the basic trigger signal as well as setting the time origin for data acquisition. Hodoscopes, H1 and H2 were constructed as shown in Figure 2.9. The first hodoscope, H1, was placed $0.2m$ downstream from the last drift chamber W5 and the second one, H2, was set $2m$ downstream from H1. Each of them was composed of sixteen plastic scintillators (Bicron BC-412) with dimensions $70mm \times 1160mm \times 10mm$ for H1, $120mm \times 1400mm \times 10mm$ for H2. The counters in H1 and H2 were arranged side by side with a pitch of $72mm$. Each counter of H2 was set at the same x position as the corresponding H1 counter to form pairs and overlapped with the neighboring counters by $48mm$. All scintillators were viewed from both top and bottom ends by photomultipliers, and a signal from the top/bottom photomultiplier was discriminated and divided into two. One output was fed to a mean-timer to get a timing pulse independent of y position of a hit. The mean-time signal was used for triggering and the start time of the drift chamber TDC. The relative time of the signals from all counters were adjusted by cables to be within $0.5nsec$. The other output was led to TDC modules with a time resolution of $25psec$ through a $50m$ coaxial delay cable 5D2V. The

[1] These resolutions are obtained from Figure 3.2.

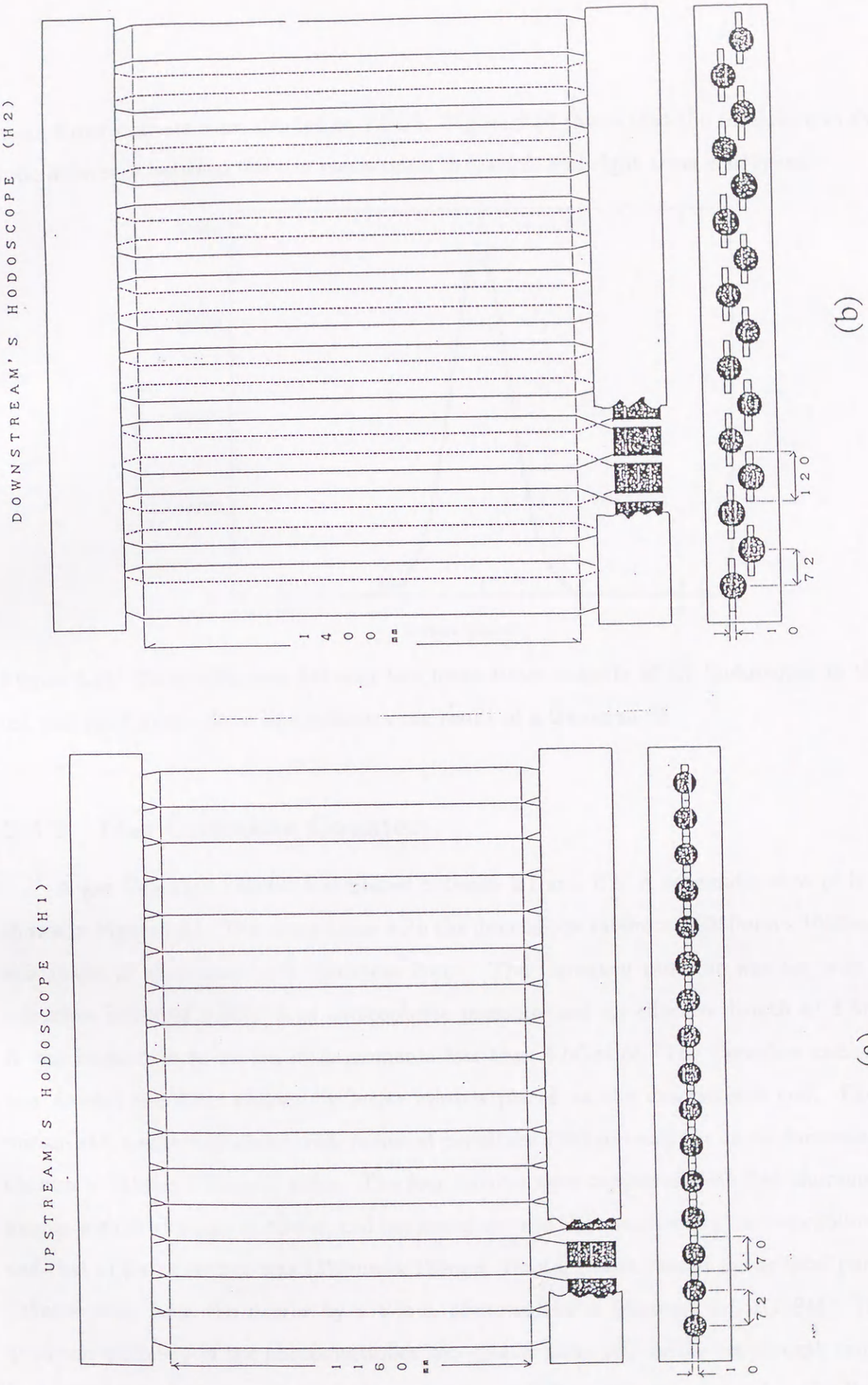

Figure 2.9: Schematic view of the (a)H1 and (b)H2 hodoscopes

mean-timer outputs were also led to TDC's. Figure 2.10 shows that the resolution in the time difference between the two mean-times in the left and right arms is $619psec$.

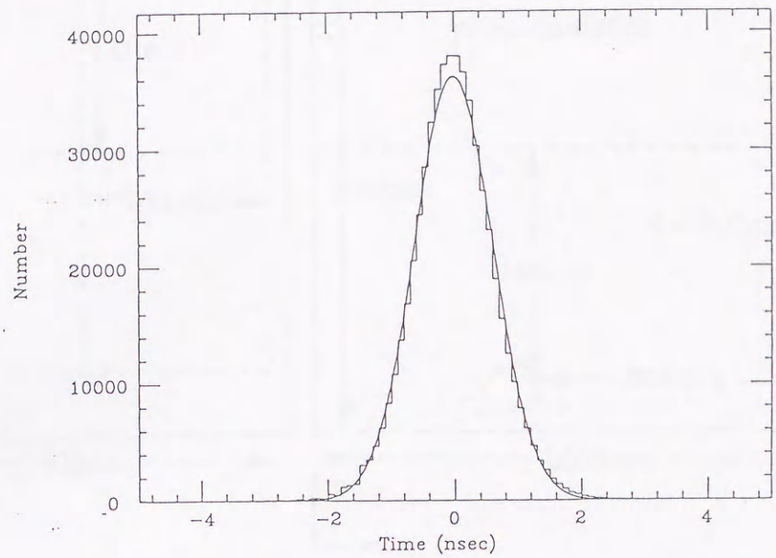

Figure 2.10: Time difference between two mean-timer outputs of H1 hodoscopes in the left and right arms. Solid line indicates the result of a Gaussian fit.

2.4.2 Gas Čerenkov Counter

A gas Čerenkov counter was placed between H1 and H2. A schematic view of it is shown in Figure 2.11. The outer frame with the dimensions $1400mm \times 2050mm \times 1660mm$ was made of aluminum with thickness $2mm$. The Čerenkov radiator was air with a refractive index of 1.000273 at atmospheric pressure and an effective length of $1.5m$. It was insensitive to muons with momenta less than $4.5GeV/c$. The Čerenkov counter was divided into four regions by lucite mirrors placed at the downstream end. Each mirror had a spherical shape with radius of curvature $1900mm$ and the same dimensions $651mm \times 751mm$ with each other. The four mirrors were supported with five aluminum boards with thicknesses of $15mm$, and the size of three of the boards was $1370mm \times 250mm$ and that of the other two was $1370mm \times 150mm$. Photons were viewed at the focal point $905mm$ away from the mirror by a 5-inch photomultiplier (Hamamatsu R1584). The quantum efficiency of the photomultiplier was greater than 10% in the wavelength range from $200nm$ to $550nm$ and reached maximum of 28% at $350nm$. Assuming the light collection efficiency to be 50%, about 9 photoelectrons were expected for each electron

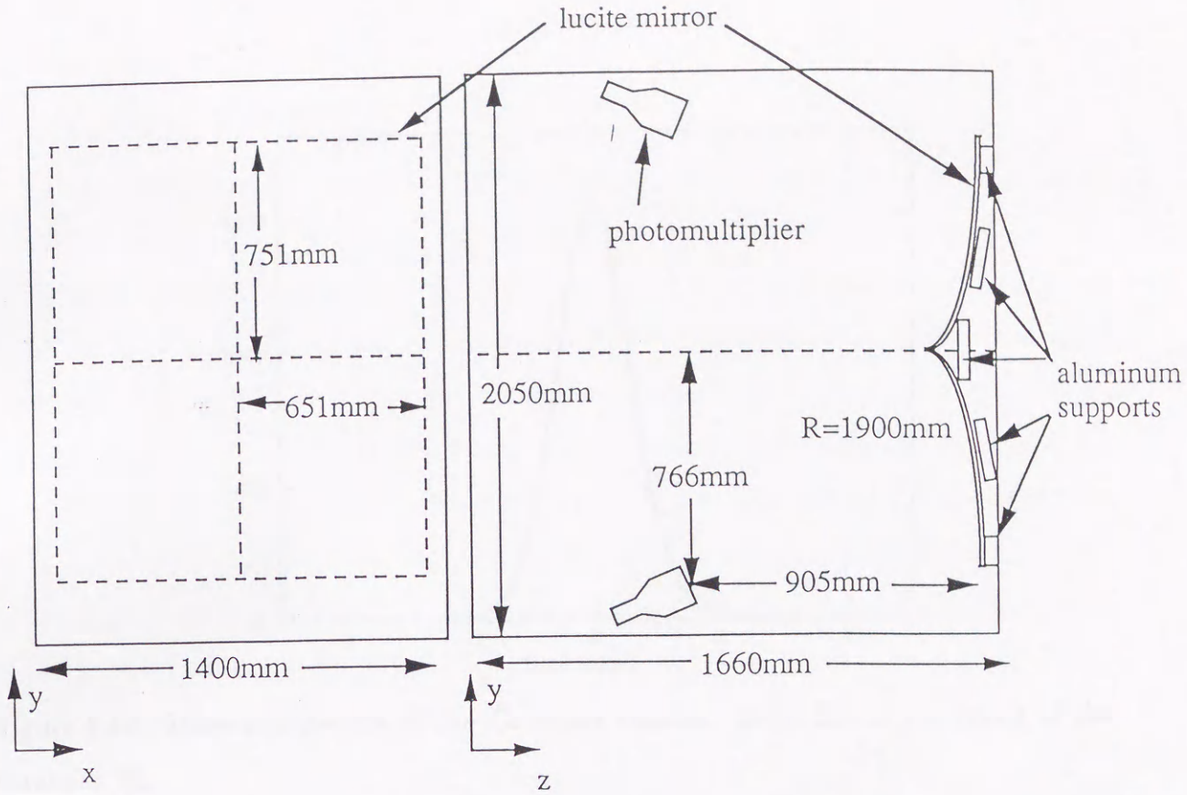

Figure 2.11: Schematic view of the gas Čerenkov counter

entering the counter using the following formula:

$$N = 2\pi\alpha L \int_{\lambda_1}^{\lambda_2} \left(1 - \frac{1}{\beta^2 n^2}\right) \frac{d\lambda}{\lambda^2}, \tag{2.1}$$

where α is the fine structure constant, L is the length of radiator, and λ_1, λ_2 represent the limits of wavelength for which the photomultiplier is sensitive. Since the fringing field of about $2Gauss$ from the spectrometer magnets was present at the photomultipliers, several-turn coils were mounted just at surface of each photomultiplier to compensate. A signal from each photomultiplier was divided into three signals by a passive divider. One of them was used for an electron trigger. Another was transmitted to an ADC through a delay of a $50m$ coaxial cable 5D2V. The gate width for ADC was $60nsec$. The remaining signal was fed to a TDC module. The level of one photoelectron was calibrated by a special run during beam off time. Figure 2.12 shows the time distribution of the gas Čerenkov counter, and the resolution was obtained to $604psec$ including the time resolution of the Hodoscopes.

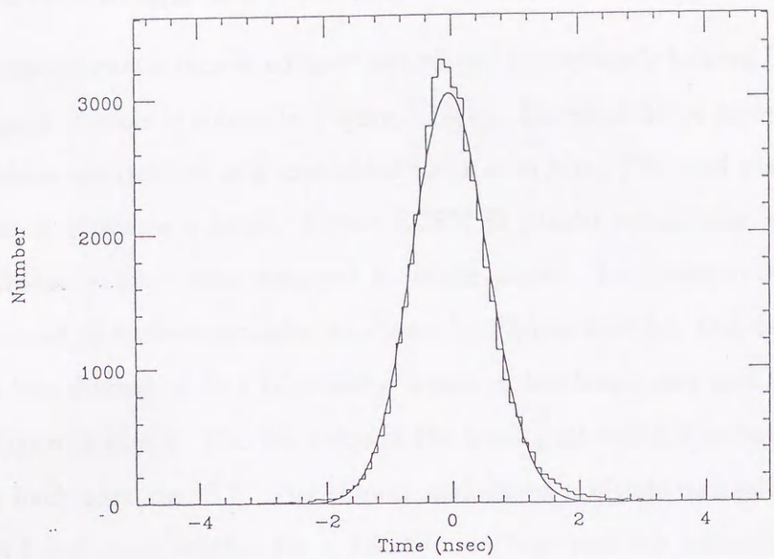

Figure 2.12: Time distribution of the Čerenkov counter. Solid line is the result of the Gaussian fit.

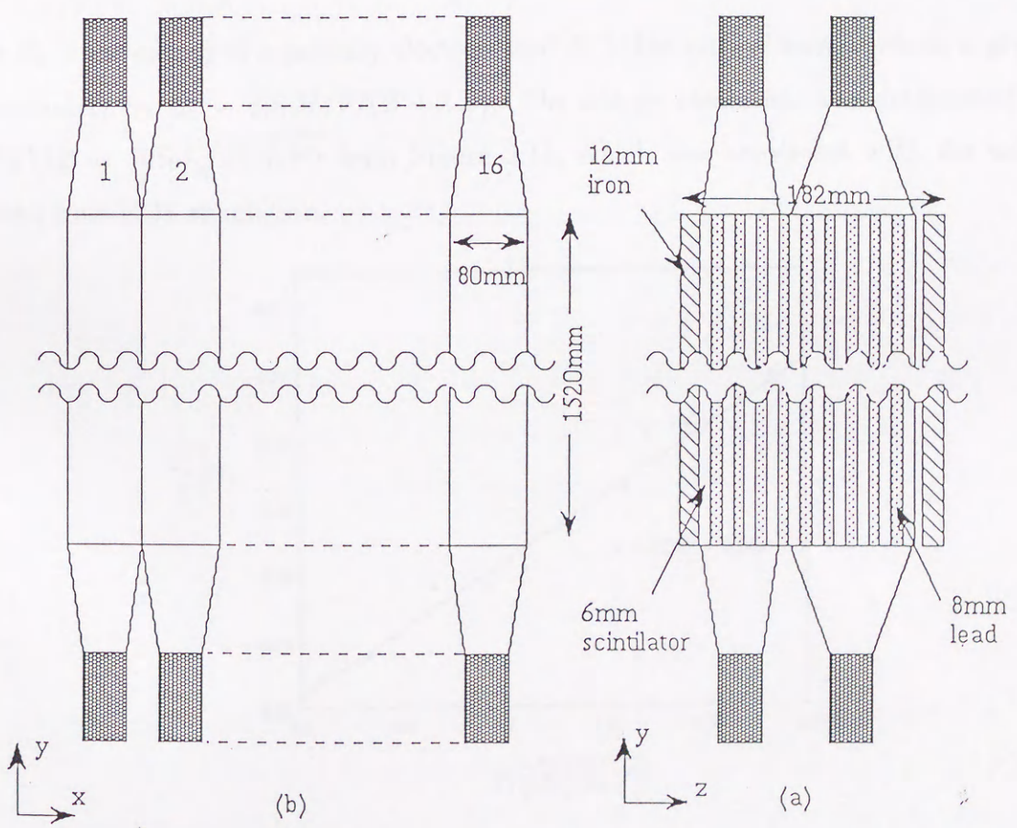

Figure 2.13: Schematic view of the electromagnetic shower counter.

2.4.3 Electromagnetic Shower Counter

The electromagnetic shower counter was placed immediately behind H2. A schematic view of a typical module is shown in Figure 2.13(a). Ten scintillator layers and nine lead plate layers were sandwiched and assembled in an iron box. The lead plates had dimensions $1345mm \times 1500mm \times 8mm$. Kyowa SCSN 81 plastic scintillator with dimensions $80mm \times 1520mm \times 6mm$ was wrapped in white paper. Each electromagnetic shower counter consisted of sixteen modules as shown in Figure 2.13(b), and each module was divided into two sharing of four scintillator layers in the front part and six layers in the back part (Figure 2.13(a)). The thickness of the front part was 5.0 radiation lengths and those of the back part was 8.7. The shower maximum position was estimated to be at a depth of 4.1 radiation lengths for a $1GeV/c$ electron and 5.5 radiation lengths for a $4GeV/c$ electron using the formula;

$$t_{max} = \ln(E_0/E_c) - 0.5, \tag{2.2}$$

where E_0 is the energy of a primary electron, and E_c is the critical energy which is given approximately by $E_c = 800MeV/(Z + 1.2)$. The energy resolution was determined to be $\sigma(E)/E = 20\%/\sqrt{E(GeV)}$ from Figure 2.14, which was consistent with the value expected from EGS simulation.

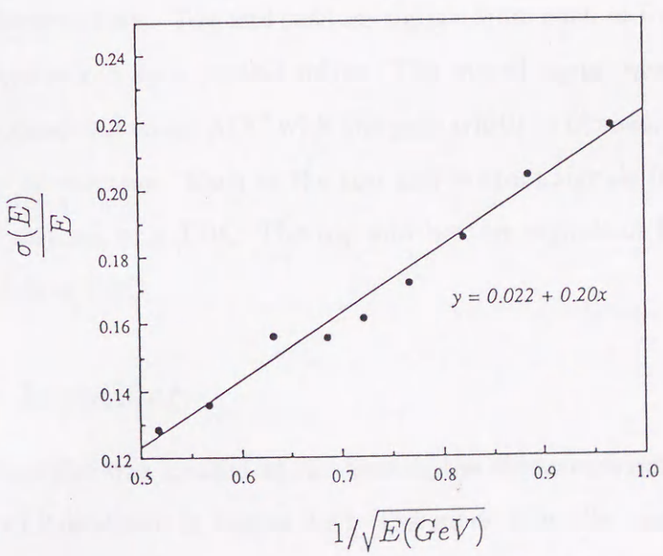

Figure 2.14: The energy resolution of the electromagnetic shower counter as a function of the energy of an electron.

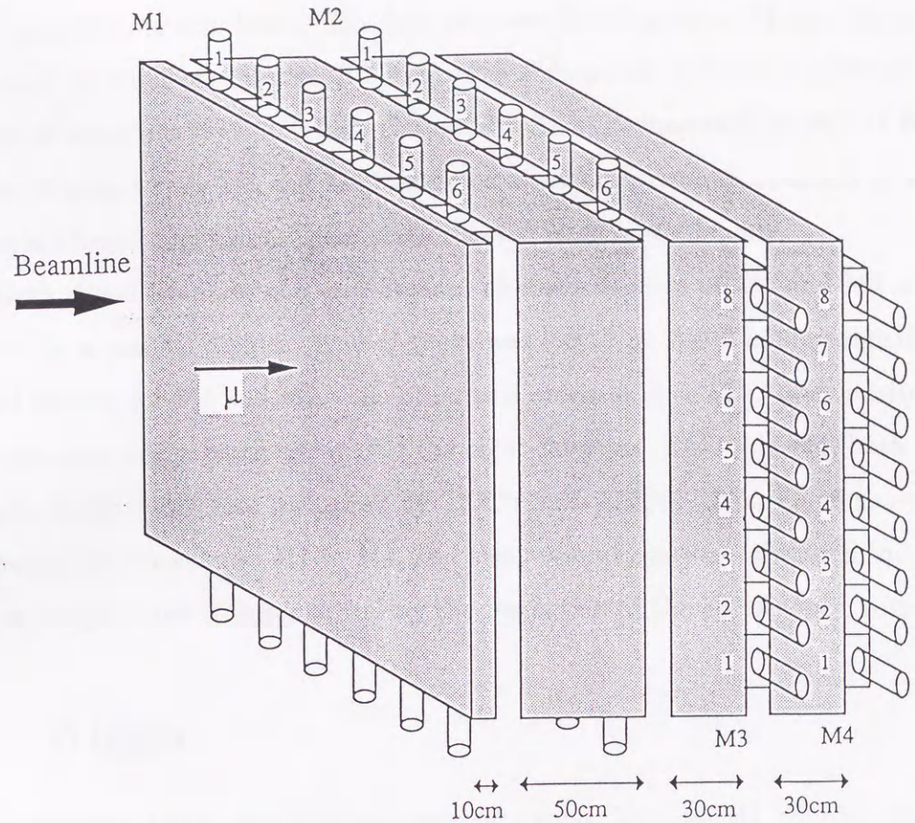

Figure 2.15: Schematic view of the muon identifier.

Each part in one module was viewed by 2-inch photomultipliers (Hamamatsu H1161) from the top and bottom ends. Top and bottom signals from each of front and back parts in each module were mixed by a passive mixer. The mixed signal was divided into two, and one part was connected to an ADC with the gate width of $60nsec$, and the other was used for triggering an electron. Each of the top and bottom signals from the front part was discriminated and led to a TDC. The top and bottom signals of the back part were mixed and also led to a TDC.

2.4.4 Muon Identifier

The muon identifier was located at the back of the electromagnetic shower counter. A schematic view of it is shown in Figure 2.15. The muon identifier consisted of four iron blocks followed by a scintillation counter array. The blocks covered an area of $1520mm \times 1900m$. The thicknesses of the blocks were 10, 50, 30 and $30cm$, respectively in the downstream direction. Muons with momenta 0.4, 1.0, 1.4 and $1.8GeV/c$ could penetrate

to the corrsponding iron blocks The first two scintillator arrays, M1 and M2 consisted of six vertical scintillators (Bicron BC-412) with dimensions $220mm \times 1620mm \times 10mm$. Light from them was fed into 2-inch photomultipliers (Hamamatsu H1161) at the top and bottom. The last two, M3 and M4, consisted of eight horizontal counters of $1400mm \times 210mm \times 10mm$. Light from them was collected from one side only.

Each signal from the top and bottom photomultipliers of M1 and M2 was divided into two by a passive divider. One of them was led to an ADC mixing signals from the top and bottom for M1 and M2. The other was received by a TDC after passing through a discriminator and a mean-timer. For the eight counters of M3 and M4, both the timing and pulse height were also measured by TDC's and ADC's. Figure 2.16 shows the time distribution of muons from M1 to M4, and their resolutions were obtained to be $784psec$, $657psec$, $802psec$ and $910psec$ including the resolution of the hodoscopes, respectively.

2.5 Trigger

The basic trigger was a coincidence of signals from an H1 counter and the corresponding H2 counter in both arms (parallel trigger). The mean-timer outputs of an H1 counter and the corresponding H2 counter were used to produce a parallel signal as shown in Figure 2.17. The parallel signals from the sixteen pairs of H1 and H2 counters were taken OR by a fan-in logic to produce a parallel signal for each arm. A coincidence of the two parallel signals from both arms was required and called the parallel trigger. The trigger covered a horizontal angular range of $\pm 12.5mrad$ with respect to the beam axis. It gave a severely limited acceptance for three-body decays such as $K_L^0 \rightarrow \pi e \nu$, $K_L^0 \rightarrow \pi \mu \nu$ and $K_L^0 \rightarrow \pi^+ \pi^- \pi^0$ which have large branching ratios than two-body decays, because they have smaller transverse momenta and were bent inward, while it gave much larger acceptance for two-body decays. Figure 2.18 shows the results of a Monte Carlo simulation demonstrating that the acceptances for the two-body decays are around 10^{-2}. The acceptances for the three-body decays are about 10^{-5} at the trigger level.

The $K_L^0 \rightarrow \mu e$, ee and $\mu\mu$ triggers required additional lepton-identifying signals for electrons and/or muons. The timing width of the hodoscope signal was $8nsec$, while those of muon and electron signals were $20nsec$ so that the hodoscope signal determined the timing of the system. The electron signal for each arm was made from signals of

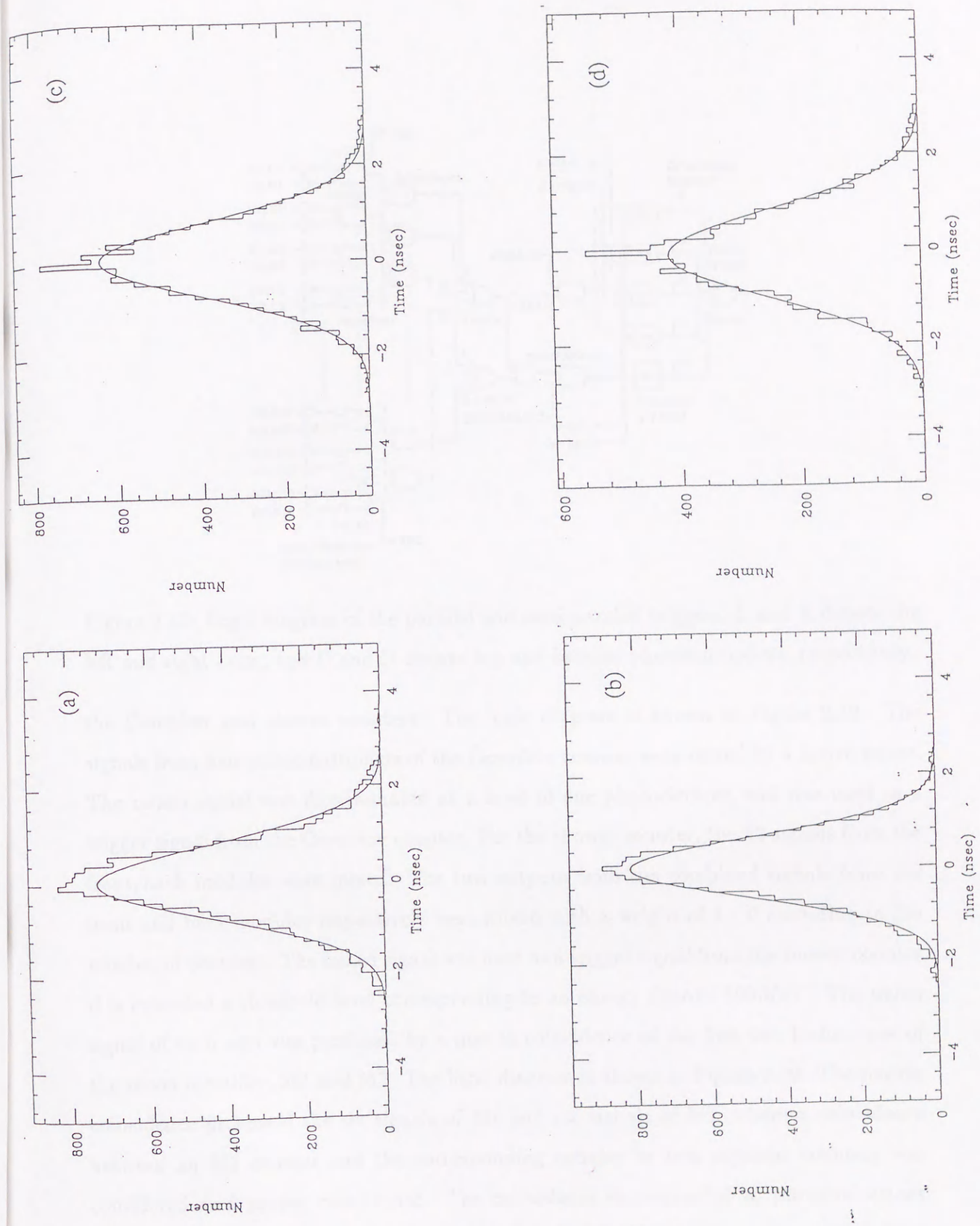

Figure 2.16: Time distribution of muon counters from (a)M1 to (d)M4. Solid line indicates the result of a Gaussian fit.

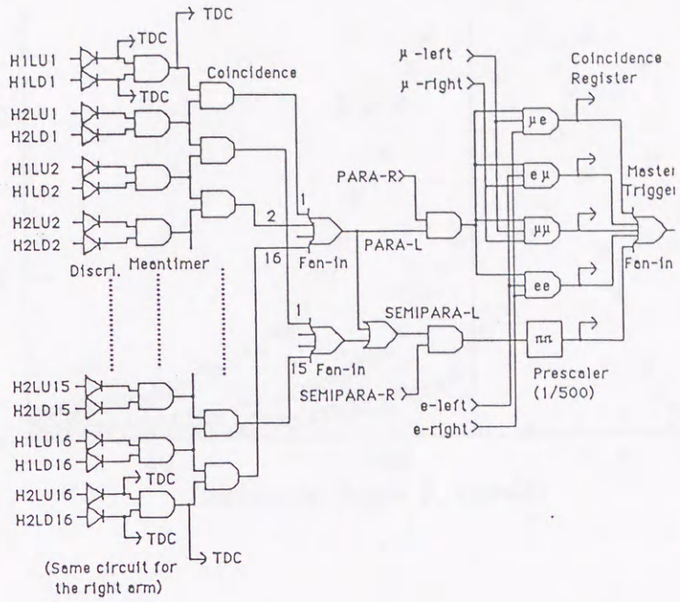

Figure 2.17: Logic diagram of the parallel and semi-parallel triggers. L and R denote the left and right arms, and U and D denote top and bottom photomultipliers, respectively.

the Čerenkov and shower counters. The logic diagram is shown in Figure 2.19. The signals from four photomultipliers of the Čerenkov counter were mixed by a active mixer. The mixed signal was discriminated at a level of one photoelectron and was used as a trigger signal from the Čerenkov counter. For the shower counter, the 32 signals from the front/back modules were mixed. The two outputs from the combined signals from the front and back modules respectively were mixed with a weight of 4 : 6 according to the number of counters. The mixed signal was used as a trigger signal from the shower counter if is exceeded a threshold level corresponding to an energy deposit $500MeV$. The muon signal of each arm was produced by a matrix coincidence of the first two hodoscopes of the muon identifier, M1 and M2. The logic diagram is shown in Figure 2.20. The matrix coincidence processed the six signals of M1 and six signals of M2, where a coincidence between an M1 counter and the corresponding counter or two adjacent counters was considered as a proper coincidence. The coincidence corresponded to the requirement that the momentum of the muon should be above $1.0GeV/c$.

The trigger for the decay $K_L^0 \to \pi^+\pi^-$ was made from only the hodoscopes without

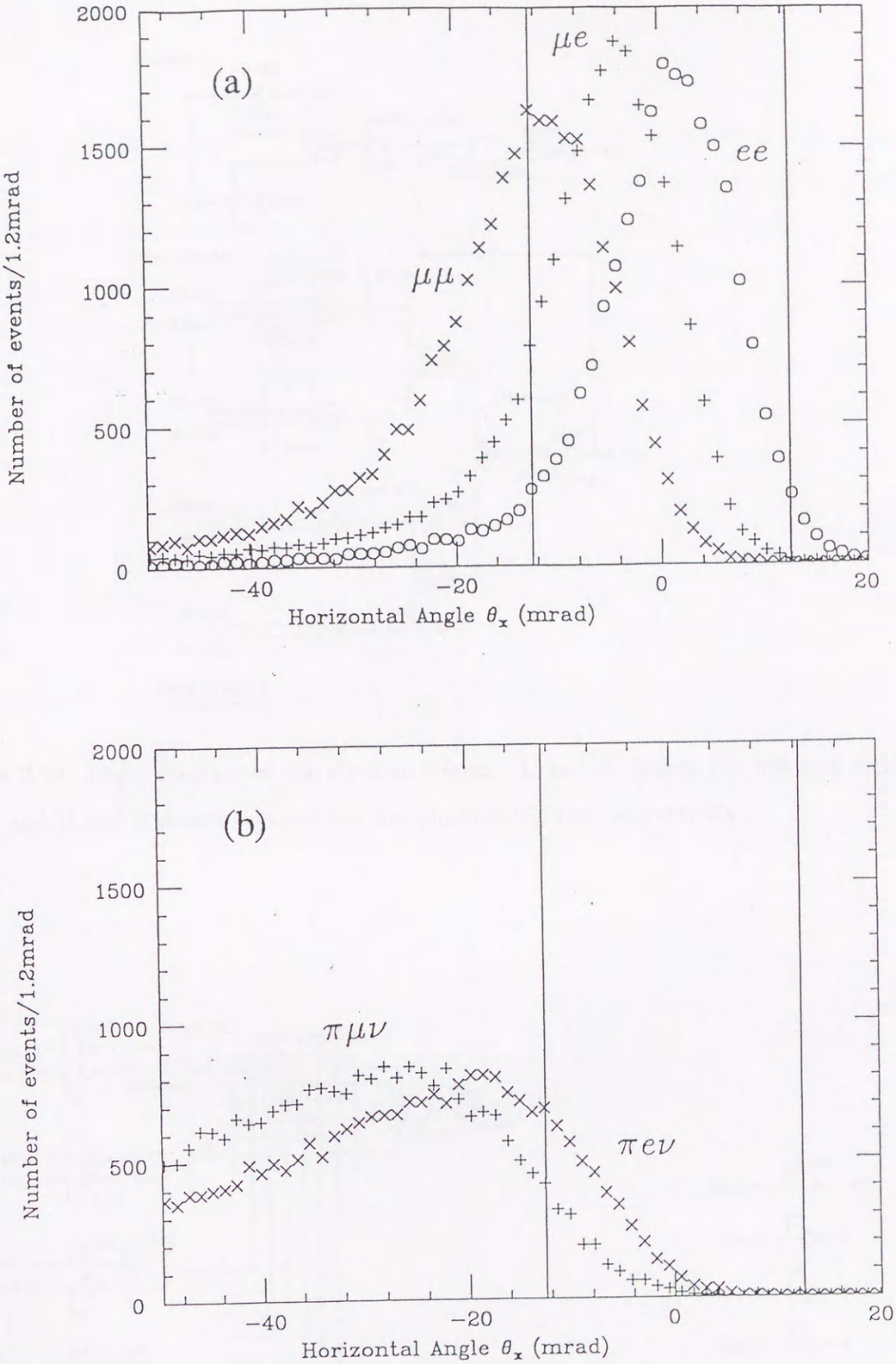

Figure 2.18: Horizontal angular distribution at H1 with respect to the beam axis (a) for two-body leptonic (10^6) decays and (b) for three-body semileptonic (10^8) decays by a Monte Carlo simulation.

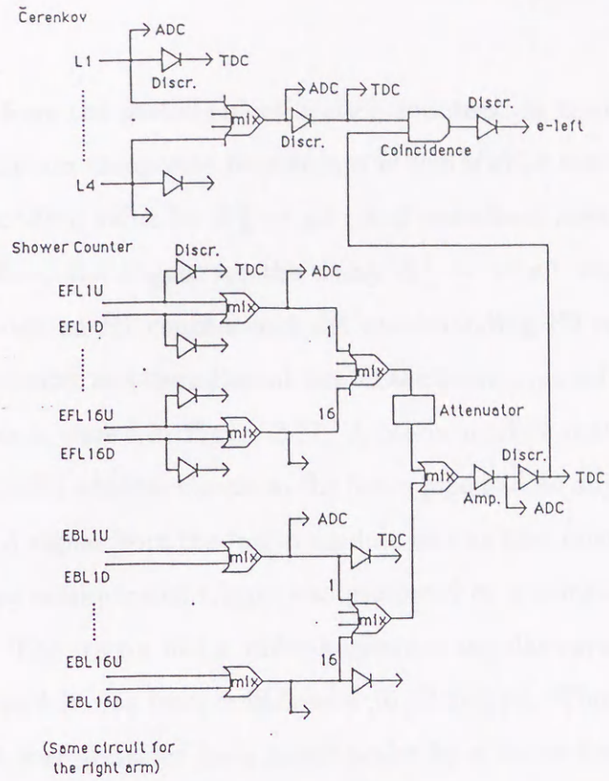

Figure 2.19: Logic diagram of the electron trigger. L and R denote the left and right arms, and U and D denote top and bottom photomultipliers, respectively.

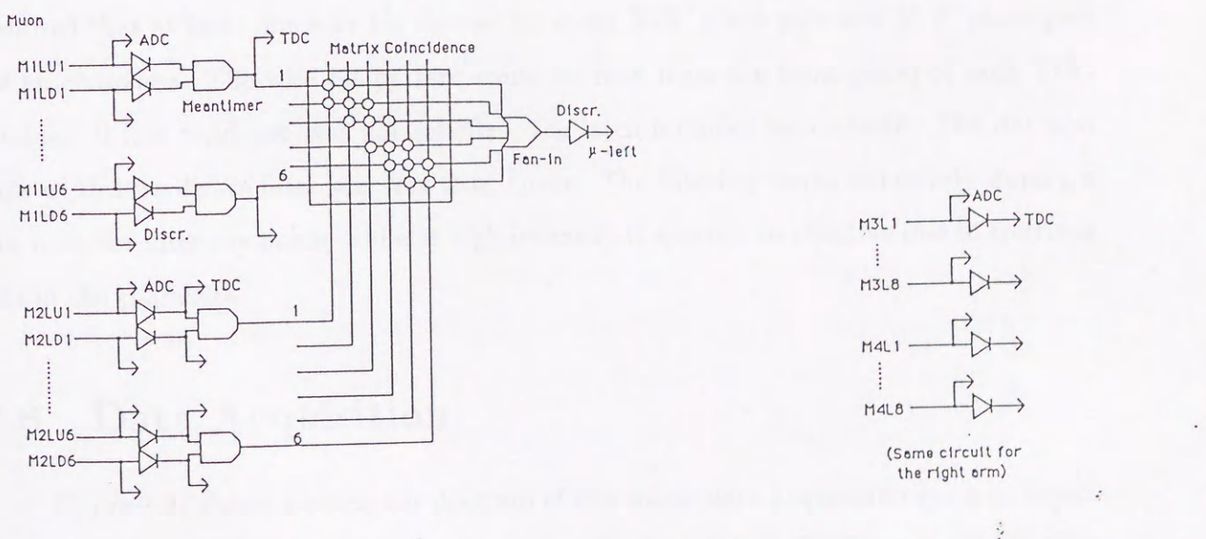

Figure 2.20: Logic diagram of the muon trigger. L and R denote the left and right arms, and U and D denote top and bottom photomultipliers, respectively.

requiring signals from the particle-identification counters. In the decay $K_L^0 \rightarrow \pi^+\pi^-$, the pions had a maximum transverse momentum of $206 MeV/c$ which was somewhat lower than the corresponding value for $K_L^0 \rightarrow \mu e$, and were bent inward by the spectrometer magnets. Therefore, the trigger for the decay $K_L^0 \rightarrow \pi^+\pi^-$ was produced by either a coincidence between an H1 counter and the corresponding H2 counter or a coincidence between the H1 counter and the adjacent one on the beam pipe side (semi-parallel trigger). The logic diagram is shown in Figure 2.17. A fun-in module makes an OR of the fifteen signals because the H1 counter closest to the beam pipe had no adjacent H2 counter on the beam pipe side. A signal from the fun-in module was further mixed with a parallel signal for each arm. The semi-parallel trigger was produced by a coincidence of two OR signals from both arms. The trigger had a wider horizontal angular coverage than that with the parallel trigger, and it was from $-48.5 mrad$ to $12.5 mrad$. Thus, since the trigger rate was very high, it was prescaled by a preset scaler by a factor from 250 to 500, typically 500.

The dilepton and $\pi\pi$ triggers were mixed by a fun-in module to produce the master trigger. Thus, the four decay modes were simultaneously triggered and tagged to take data.

In order to reduce accidental triggers, a signal was made from checking the hit patterns from the drift chambers and was called a hardware filter. The filter module required that at least one wire hit existed for every X-X' plane pair and Y-Y' plane pair for all chambers. The wire hit pattern could be read from the front panel of each TDC module. If this condition was not satisfied, the latch modules were closed. The decision time of this hardware filter was less than $1 \mu sec$. The filtering works effectively during a run with low intensity beam, while at high intensity it was not so effective due to spurious hits in the chambers.

2.6 Data Acquisition

Figure 2.21 shows a schematic diagram of the online data acquisition system. Seven CAMAC crates were used for blind scalers, coincidence registers, TDC's and ADC's. The TDC's for each drift chamber were contained in a TKO crate. The data of the modules in each crate were scanned by a crate controller called a CH (Control Head) and stored

in a memory module called MP (Memory Partner) event by event during a beam pulse of $0.5sec$. An MP has a storage capacity of 32bit $\times$ 8k. Fast crate controller which has a Towel (TKO Online Wire Link) bus interface for ADC's and TDC's were used. Seventeen MP modules were arranged in two CAMAC crates which were connected by a crate controller, Kinetic K3922. A Kinetic K2922 interface board was connected between the CAMAC crate and the host computer μVAX II.

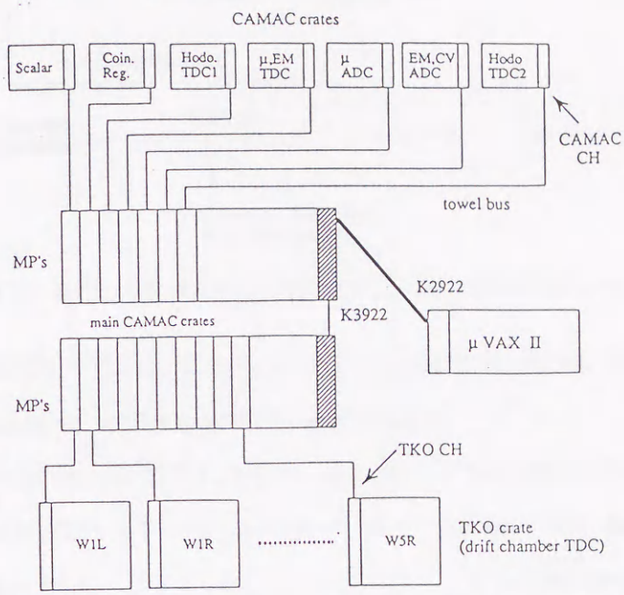

Figure 2.21: Schematic diagram of the online data acquisition system.

A flow diagram of the data acquisition system is shown in Figure 2.22. When a master trigger came to the data acquisition system, other triggers were inhibited while the master trigger was being processed. At the same time, all CAMAC TDC's and ADC's began to digitize the detector signals. The conversion times of the CAMAC modules were adjusted within $50\mu sec$. If the hardware filter described in the previous section vetoed the master trigger, then all the modules were cleared, and the system was ready to accept data. If the trigger passed the hardware filter, the system waited for $60\mu sec$ during the conversion and commanded all the MP's to start storing data. If there was no value in a TDC, namely the coverted value was zero, it was not transferred to the MP. Similarly, if the value in an ADC was less than the pedestal, it was not transferred to the MP. In this way, we could transfer the TDC and ADC data during a short time. When the MP finished storing the data, it sent out the end signal. When all the MP's were ready, the system cleared all the modules and waited for the next trigger. It took $12\mu sec$ to clear

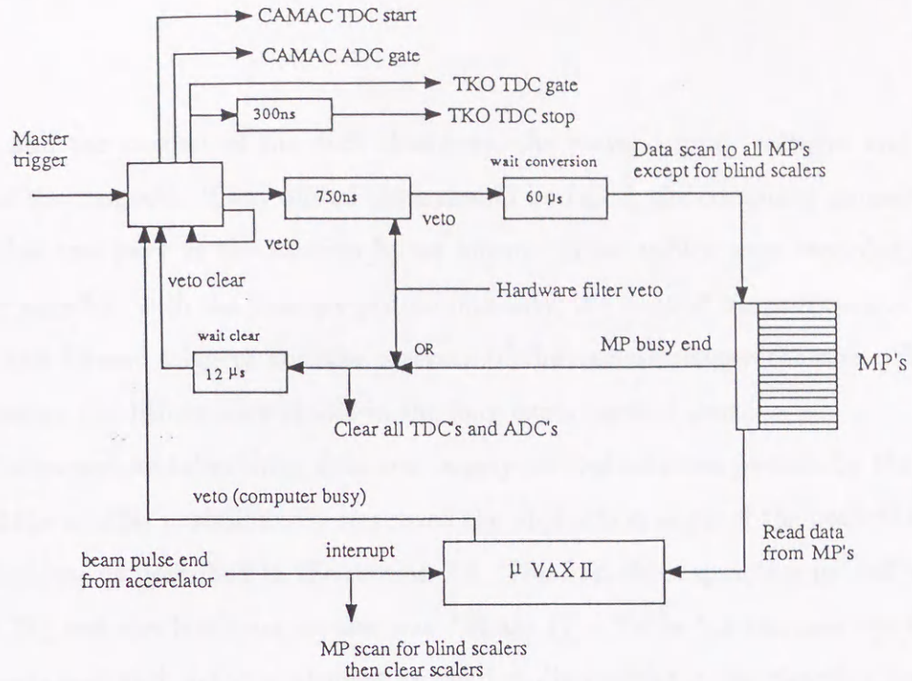

Figure 2.22: Schematic diagram of the control signal flow.

the ADC's and TDC's. The data acquisition system took about $200 \sim 400 \mu sec$ from a master trigger coming in until the system was ready.

The data stored in the MP's were transferred to the host computer and processed event by event during the $2.65 sec$ interval of beam pulses. The data transfer rate was $0.8 \mu s/byte$. At this stage, the timing between the two hodoscopes H1 in the left and right arms was examined and required to be within $\pm 5.0 nsec$. By this filtering, events were reduced by about 10% to 20%. The filtered data were recorded on magnetic tape. The average data size of one event was about 2k bytes, and the data were written in one 2400-foot magnetic tape with 6250bpi per about one hour under normal conditions. For the last quarter period, the data were recorded in one 2Gbyte 8mm video tape per more than eight hours.

2.7 Running Condition

We had accumulated data in the physics running time from 1988 to 1990. During that time, the detector condition was monitored by the online computer. At least one event per pulse was sampled and all the data of the event were unpacked and were accumulated into histograms of this purpose. The sampling rate was adjusted so that the computer could be ready by the next pulse. The computer monitored on the high

voltage and the current of the drift chambers, the power supply voltages and the field values of the magnets. If any one of them should be failed, the computer paused the data acquisition and gave us the caution by an alarm. These values were recorded on a pen recorder together with the primary proton intensity, the neutral beam intensity, numbers of raw and filtered triggers and the pressure of the vacuum decay chamber. The beam and detector conditions were stable in the long experimental time.

The experimental running time was largely divided into two periods by the improvement of the neutral beamline. We improved the production angle of the neutral beam and the collimator as described in the section 2.2. The first three quarters period was called "Phase I", and the last quarter one was "Phase II". Table 2.3 summarizes the single counting rate of each detector element at the first discriminator, the chamber current and the averaged number of hits per plane in the two phases. Table 2.4 also summarized the trigger rate at each trigger stage. In the Phase I, the intensity of the primary proton beam was $1.0 \times 10^{12} \sim 1.5 \times 10^{12}$ *ppp*. At the same intensity, the counting and trigger rates in the Phase II were less than the Phase I, and the intensity was increased in the Phase II and was $2.0 \times 10^{12} \sim 2.5 \times 10^{12}$ *ppp*.

Each phase was further divided into several periods called "cycle". The KEK PS had two running modes called a two-week cycle and a three-week cycle. In former mode the PS ran for nine days in two weeks, while in the latter it ran for fourteen days in three weeks. The Phase I consisted of seventeen cycles, and Phase II consisted of six cycles. Each cycle produced from about 70 to 320 runs, where a run corresponded to the amount of data of about 160M bytes, and total number of runs reached 4637 except for calibration runs. These data were processed by the offline analysis described in the following chapter.

Detector	Phase I	Phase II	
	1.5×10^{12} ppp	1.5×10^{12} ppp	2.5×10^{12} ppp
counting rate	MHz	MHz	MHz
W1L (plane)	60.	-	48.
(hottest wire)	0.87	-	0.69
H1	0.765	0.496	0.708
EMF	2.474	1.534	2.066
CH	0.715	0.433	0.601
MU1	2.374	1.155	1.601
MU2	0.934	0.413	0.572
MU3	0.620	0.288	0.407
MU4	0.675	0.302	0.432
chamber current	μA	μA	μA
W1, W2	165	88	145
W3	160	60	110
W4, W5	71	35	63
# of hit per plane			
W1, W2	10	7	9
W3	9	5	7
W4, W5	6	4	5
H1	2.0	1.6	1.8

Table 2.3: Single counting rate of each detector at the first discriminator, the drift chamber current, and the averaged number of hits per plane. For each detector, the counting rate of the hottest counter is shown. The left and right arm rates were averaged except for W1L, and the sum was taken for all the counters. " W1, W2 (W4, W5) " means the average of W1 and W2 (W4 and W5).

Signal	Phase I	Phase II	
	1.5×10^{12} ppp	1.5×10^{12} ppp	2.5×10^{12} ppp
(Prescaling factor)	500	250	500
counting rate	Hz	Hz	Hz
parallel	$496K$	$253K$	$376K$
Para	$12.8K$	$5.6K$	$9.2K$
Spara	$30.1K$	$13.8K$	$22.7K$
muon	$329K$	$150K$	$212K$
electron	$78K$	$332K$	$440K$
master trigger	204	178	228
$\mu_L\mu_R$	34	21	31
$\mu_L e_R$	45	33	50
$e_L\mu_R$	37	33	50
$e_L e_R$	20	34	54
$\pi\pi$	59	39	32
hardware-filter OK	(×90.2%)	(×68.5%)	(×83.2%)
	184	122	190
software-filter OK	(×76.7%)	(×84.0%)	(×93.7%)
	140	102	154
(dead-time)	6.7%	3.9%	6.3%

Table 2.4: Counting rates at various trigger stages, and the dead-time ratio. The rates of "parallel", "muon", and "electron" were the averages of the left and right arms. Note that during the Phase II the rate of "electron" was only the Cherenkov counter signal.

Chapter 3

Data Analysis

We have accumulated a total of 4.01×10^8 triggers consisting of μe , ee and $\mu\mu$ triggers and prescaled $\pi\pi$ triggers. The fraction of μe , ee , $\mu\mu$ and $\pi\pi$ triggers are 48.0%, 18.5%, 13.5% and 20.0%, respectively. The data are processed by an offline computer(HITAC M280/680). The data analysis procedure consists of four steps: track finding and fitting, second track fitting, event selection and particle identification.

In the first step, the pattern recognition algorithm finds one or more tracks in x- and y-views of each arm by making all possible combinations of hits in the five drift chambers and orders them by fitting to straight lines with kinks at the centers of two magnets. After reconstructing three-dimensionally the tracks in each arm and combining tracks of the left and right arms, we apply loose kinematical cuts on these track candidates to save computing time by eliminating fake tracks. Then, the track candidates in each arm are fitted by a spline method[18] using hits in all chambers which consist of pairs of adjacent hits on two staggered planes and single hits, but giving a lower weighting to single hits. One or more V^0 candidates are formed by combining two three-dimensional tracks in the left and right arms, and a vertex location for each V^0 candidate is determined by finding the point of closest approach of the two tracks to each other. The V^0 candidate with the minimum distance of closest approach and the lowest χ^2 in each arm is recorded as an event without applying a χ^2 cut.

In the second step, further hit selection around the candidate track is carried out. For the second track fitting algorithm, pairs of hits and single hits are assigned the same weight. The χ^2 of the track fit is calculated using an error matrix for the spectrometer

including the chamber resolution and multiple scattering effects. Cuts on the track fit χ^2 and other track quantities are applied in this step.

In the third step, cuts are applied to reconstructed events to reject backgrounds unassociated with K_L^0 decays. Finally, in the fourth step a search is made for candidate hits in the particle identification counters along the extrapolated track.

These four steps are described in the following sections, respectively.

3.1 Track Finding and Fitting

3.1.1 Track Finding

The pattern recognition algorithm starts with selecting hits in the trigger counter and the drift chambers. The search starts by selecting in each arm pairs of hits in the hodoscopes H1 and H2 corresponding to either parallel or semi-parallel trigger. Then, the time difference between hits in the H1 hodoscopes on the left and right is required to be within $3nsec$. The resolution in time difference for the proper track is measured to be $600psec$. The requirement for the drift chamber hits is to have a drift time between $-20nsec$ and $130nsec$.

The pattern recognition algorithm searches for tracks in x- and y-views of each arm using the selected hits from the trigger counters and the drift chambers. The pattern recognition starts from the downstream side, because the downstream chambers of W4 and W5 have fewer extraneous hits than the upstream ones. Here, a pair of two adjacent hits in the staggered planes (called staggered hits) is treated as one hit, and a track in each view should have five hits. In the y-view, a guideline is constructed by connecting hits of W4 and W5. It is extrapolated upstream, and hit candidates are selected in each drift chamber from W1 to W3. A straight track for each combination of the candidate hits is obtained by fitting five hits using the least square fitting method. The most probable track for each pair of W4 and W5 is selected according to the χ^2 of the fit. The procedure for combining hits into candidates in the x-view is more complicated because a straight line cannot be used here due to the kick by the main component of the magnetic field. The first step is to form pairs of all hits by taking all combinations of hits in W4 and W5. Then triplets are formed by combining each pair with each hit in W3, introducing

a bend angle due to the second magnet which is located between W3 and W4. Then for each triplet the track is extrapolated to W1 and W2, introducing the same bend angle for the first magnet (located between W2 and W3) and quintuplets are formed by taking the hits in W1 and W2 which are the closest to the extrapolated track for each triplet. The χ^2 is calculated for each quintuplet, and the one is chosen which has the minimum χ^2, and for each triplet, the other combinations of hits in W1 and W2 are discarded. All tracks formed from each triplet are saved provided that χ^2 is less than a cutoff value. The cutoff value is determined to make a routine as fast as possible without loosing the $K_L^0 \to \pi^+\pi^-$ events by the cut. The tracks in each view are required to have three or more pairs of staggered hits.

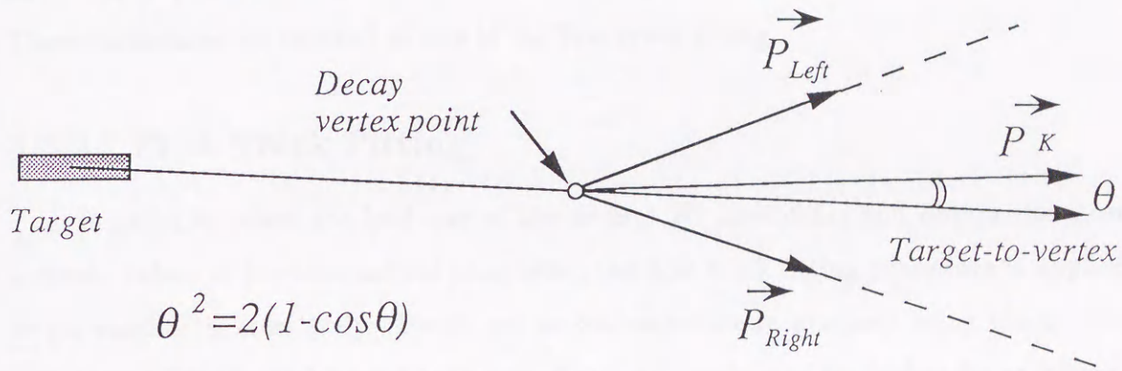

Figure 3.1: Definition of the collinearity angle θ.

When more than one track candidate is found by the above procedure in at least one view, all possible combinations of tracks of x- and y-view are combined to form three-dimensional tracks. The momentum of a track in each arm is calculated from the kink angle using knowledge of the magnetic field. Combining two three-dimensional tracks in the left and right arms to form V^0 candidates, the provisional decay vertex is defined as the midpoint between the points of the closest approach of the two tracks. Then, the distance at the closest approach, Δ_v, is calculated. The collinearity angle θ between the target-to-vertex direction and the K_L^0 momentum, P_K, which is a vector-sum of momenta of the two tracks, is calculated (see Figure 3.1). In order to reduce three-body decays, the event candidate requires to have the product, $P_K\theta^2$, less than $0.55 MeV/c \cdot rad^2$, where $P_K\theta^2$ is chosen since $\Delta(P_K\theta^2)$ is independent of P_K and θ^2. This property is confirmed by a Monte Carlo simulation. Further, the effective mass is calculated according to the trigger mode. μe and $\mu\mu$ event candidates whose effective mass is less than $430 MeV/c^2$

are eliminated. The mass selection is not applied to events of the other trigger modes, because they are useful for the calibration of particle identification counters.

After these cuts, the remaining V^0 candidates were stored in order of increasing χ^2_{v0} with a limit of ten best χ^2_{v0}, where the χ^2_{v0} is defined by,

$$\chi^2_{v0} = \sum_{L,R} \frac{(\chi^2_x + \chi^2_y)}{4} + \frac{\Delta^2_v}{\sigma^2_v}, \tag{3.1}$$

where χ^2_x, χ^2_y are the track fit χ^2 calculated in the pattern recognition for x- and y-views, respectively, and σ^2_v is the resolution of the vertex distance (Δ_v) which is taken as $10mm$. At this stage, the V^0 candidates formed from several different track candidates in one event may remain, and the average number of the candidates is about 2.4 per event. These candidates are reduced to one in the first track fitting.

3.1.2 First Track Fitting

In order to select the best one of the several V^0 candidates and obtain the most accurate values of the kinematical parameter, the first track fitting procedure is applied to the candidates iteratively. Tracks are reconstructed more precisely using the quintic spline model[18] in which a track is described by a spline curve of the fifth order as follows:

$$x_i \approx a_1 + a_2 z_i + \frac{1}{p} X(z_i), \tag{3.2}$$

$$y_i \approx b_1 + b_2 z_i + \frac{1}{p} Y(z_i). \tag{3.3}$$

$X(z_i)$ and $Y(z_i)$ are derived by double integration of cubic spline expressions, and describes the trajectories in the x- and y- views of charged particles in the magnetic field. The magnetic field map is made from a field measurement performed using a grid with 5, 5 and $2.5cm$ step in the x, y and z coordinates, respectively. For 46 particular z_i positions including the 20 chamber planes, at each iteration x_i and y_i are calculated for that z_i position using (3.2), (3.3), and the magnetic field is then calculated at that x, y and z from the magnetic field map by using Bessel's interpolation formula of third degree.

The chamber hit positions for staggered hits are calculated using the drift length which is calculated from the TDC information by converting it to drift time[19]. The drift time is related to the charge accumulated in the each TDC by a linear function whose coefficients are different for each TDC. Its two coefficients for every wire are determined by

applying a test pulse to the amplifier-discriminator boards and TDC's with various time delays. The propagation delay in the chamber wire is also considered, and the propagative velocity is determined to be $250mm/nsec$ by a test pulse measurement. The drift velocity is expressed by a quadratic function of the drift time, and its three coefficients for every wire are calculated from an analysis of tracks in the real data. Using this function, the drift time is converted to the drift length. The hit position for a single hit is given as the sense wire position in this step.

The left-right ambiguity for a pair of staggered hits is resolved using information from the expected with position calculated from the track fit. Since there are four solutions with different slopes between two hits, the algorithm chooses the solution consistent with the slope of the provisional track at the chamber position. Since there is no easy way to resolve the left-right ambiguity from single hits, the hit position for a single hit is given as the sense wire position in this step.

The fitting is performed for all track candidates. Using the tracks in both the left and right arms as well as the vertex position, χ^2 is calculated as follows:

$$\chi^2_{total} = \frac{1}{f}\left\{\sum_{L,R}\sum_{i=1}^{N}\frac{(X_i - x_i)^2}{\sigma_i^2} + \frac{\Delta_v^2}{\sigma_v^2}\right\}, \tag{3.4}$$

where the X_i are the hit positions, the x_i are the fitted track coordinates, and σ_i are the spatial resolutions which are given as $400\mu m$ for the staggered hits and $3.5mm$ for the single hit. Δ_v is the distance between two tracks at the vertex, and σ_v is the vertex resolution which is given as $10mm$. N is the total number of x and y planes with hits (maximum of 20 planes in each arm), and $f = N_L + N_R - 10$ is the degree of freedom where 10 is the number of fitting parameters in both arms. The combination of left and right tracks with minimum χ^2_{total} is chosen.

Then, the effective mass is calculated assigning the masses according to the trigger mode. In order to reduce three-body decays in the μe and $\mu\mu$ events, the effective mass of μe and $\mu\mu$ is required to be greater than $475MeV/c^2$. Any other cut is not applied.

The total number of events for each trigger mode which have passed this procedure is summarized in Table 3.1. The number of events is reduced by about a factor of 25 by this procedure. Most of the eliminated events come from the three-body decays of K_L^0's and accidental triggers. For the reduced data, the track and kinematical parameters are recorded on magnetic tapes together with all of raw data information.

Trigger mode	Number of events
μe	1.7×10^6
$\mu\mu$	0.73×10^6
ee	6.4×10^6
$\pi\pi$	6.9×10^6

Table 3.1: Total number of events for each trigger mode which have passed the track finding and fitting procedure.

3.2 Second Track Fitting

The second track fitting procedure is applied to the events selected by the track finding and fitting procedure described in the previous section. In the first track fitting procedure, tracks are fitted based on the staggered hits. However, when there are successive pairs of staggered hits around the pair of hits which are used, the track will have an ambiguity as to which pairs should be used in the fitting. Furthermore, it is possible that a drift time information of one wire in the staggered hit is destroyed by an accidental hit. When wrong hits are used in the tracking, the momentum and χ^2 of such a track cannot be estimated properly. Therefore, we have done further selection of hits. A search is made for new candidate hits in the area between $\pm$1cell away from the hit selected in the track finding procedure for the staggered hits and $\pm$2cells away for the single hit.

Before searching for new candidate hits among staggered hits, we calculate the sum of the two drift lengths to estimate the property of the hits. For the staggered hits in principle, the sum of the drift lengths should be equal to the half cell size of $4.5mm$ after correcting for the incident angle of the track. Figure 3.2 shows the distribution of this sum. We define a "good" pair of hits as one having sum of the drift lengths sum lying between $3.3mm$ and $5.7mm$, and a "bad" pair of hits as one having the sum of drift lengths lying outside this interval or with the deviation of hit positions from the track to be larger than $1.2mm$ even for a pair of hits with the drift length sum not to lie between $3.6mm$ and $5.4mm$, For "bad" pairs a search is made among the other combinations to find a pair with the sum of the drift lengths nearer to $4.5mm$. If the best pair of staggered hits has a sum of the drift lengths greater than $5.7mm$ or less than $3.3mm$, only the hit

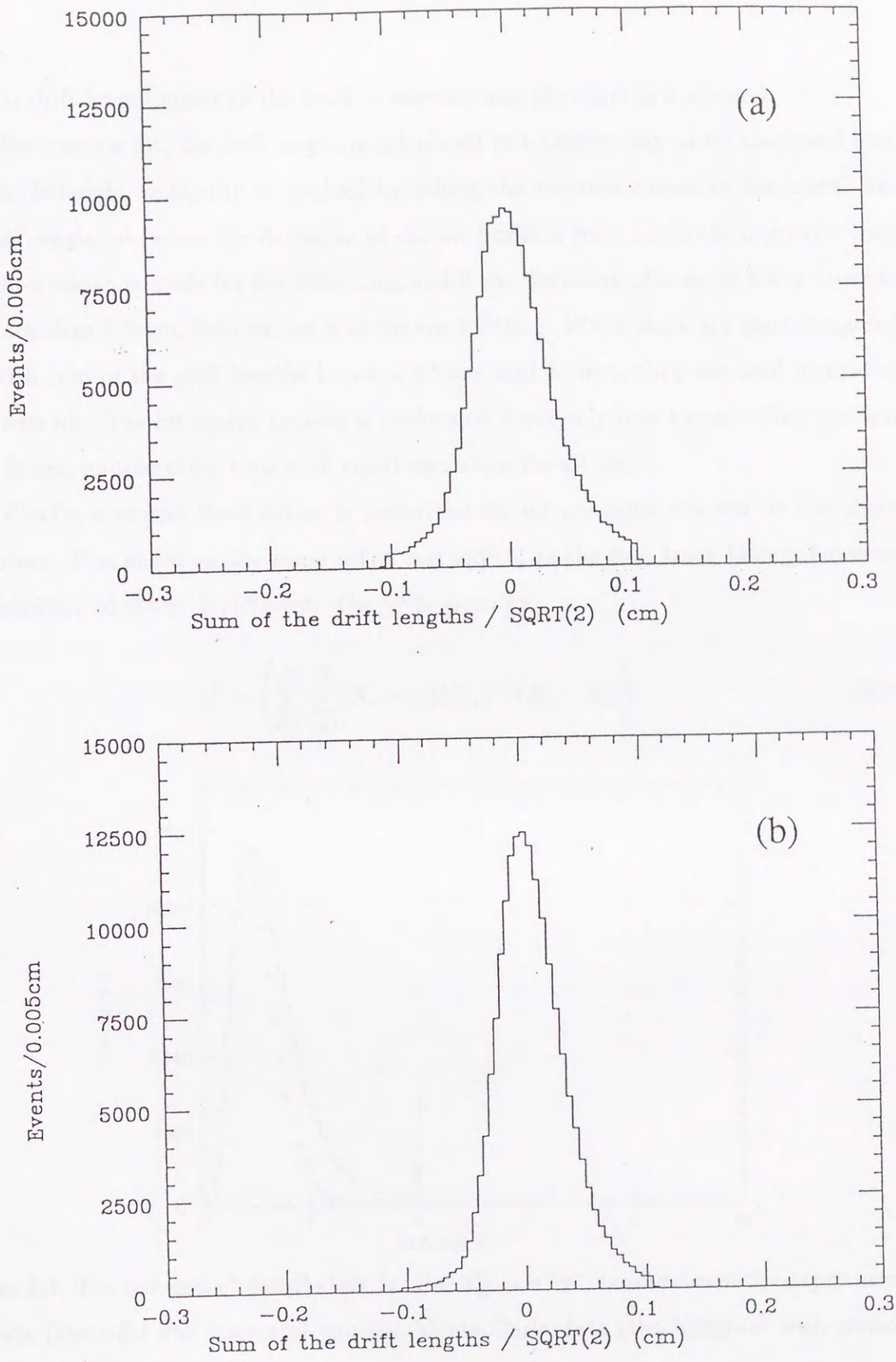

Figure 3.2: Distribution of sum of the dirft lengths of the two adjacent hits on the staggered planes (a) for W1 and W2 (b) for W3, W4 and W5.

with its drift length closer to the track is selected and the other is discarded.

For a single hit, the drift length is calculated in a similar way as for staggered hits, and the left-right ambiguity is resolved by taking the solution closest to the track. For a "bad" single hit, when the deviation of the hit position from the track is greater than $1.7mm$, a search is made for the other hits, and if the deviation of a single hit is closer to the track than $1.7mm$, then we use it in the track fitting. When there are good staggered hits with sum of the drift lengths between $3.3mm$ and $5.7mm$, they are used instead of the single hit. The hit search process is performed iteratively four times calling the first track fitting routine every time with equal resolution for all hits.

Finally, a second track fitting is performed for hit positions selected by the above procedure. It is based on the same spline method[18] as the first track fitting, however, the definition of the χ^2 is different. The χ^2 is given by,

$$\chi^2 = \left(\sum_{i=1}^{N} \sum_{j=1}^{N} (X_i - x_i)(E_{ij})^{-1}(X_j - x_j) \right), \tag{3.5}$$

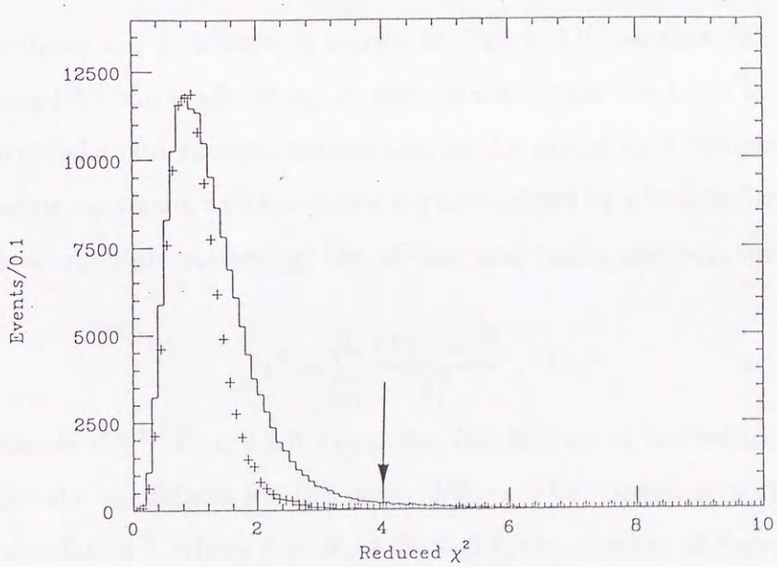

Figure 3.3: The reduced χ^2 distribution for the $K_L^0 \to \pi^+\pi^-$ candidates of the experimental data (the solid line histgram) and the Monte Carlo data (the histgram with simbol "+").

where E_{ij} is the error matrix and the inverse $(E_{ij})^{-1}$ is the weight matrix. The diagonal elements of the matrix are the usual variance, σ_i^2. The σ_i's are the individual resolutions for each plane which has been obtained from the measurement as $330\mu m$ for W1 and

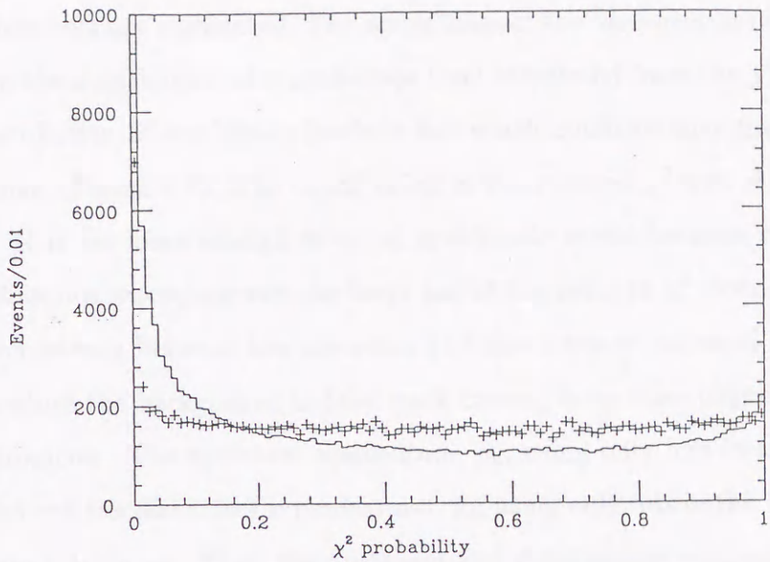

Figure 3.4: Distribution of confidence levels for the $K_L^0 \to \pi^+\pi^-$ candidates of the experimental data (the solid line histgram) and the Monte Carlo data (the histgram with simbol "+"). The distributions are normalized to the peak value.

W2 and $280\mu m$ for W3 to W5. [1] We get the values of the position resolutions of the drift chambers from the distributions shown in Figure 3.2, because the measurement is little influenced by the track fitting quality and multiple Coulomb scattering. The off-diagonal ones take into account correlations in the actual drift chamber hits due to multiple scattering upstream, and the values are determined by a Monte Carlo simulation. In the absence of multiple scattering, the off-diagonal terms are zero, and the formula reduces to,

$$\chi^2 = \sum_{i=1}^{N} \frac{(X_i - x_i)^2}{\sigma_i^2} , \tag{3.6}$$

which is the standard χ^2. Figure 3.3 shows the distribution of the reduced $\chi^2 (= \chi^2/f)$ in each arm for the candidates for the decay $K_L^0 \to \pi^+\pi^-$ together with that from a Monte Carlo simulation [2], where $f = N_x + N_y - 5$ is the number of degrees of freedom which is fourteen on the average. N_x and N_y denote the numbers of hits used in the track fitting in the x- and y-views, respectively. We require N_x to be more than 8 and N_y more than 7 (maximum of 10 possible) in each view, because the fitting in the x-view is less constrained than in the y-view. Furthermore, tracks having only single hits in two

[1] For a single hit, the resolution $\times 1/\sqrt{2}$ is set on σ_i

[2] Details of the Monte Carlo simulation are described in Appendix B.

successive chambers are eliminated, The correctness of the variances used in the fitting is checked from the distribution of a confidence level calculated from the χ^2 of the fit. The resulting distribution of confidence levels is flat which confirms that the variances used are proper ones (Figure 3.4). The cutoff value in the reduced χ^2 was chosen to be 4 for either arm. It is set loose enough to avoid systematic errors because the Monte Carlo simulation does not reproduce well the large tail of the reduced χ^2 distribution.

The consistency between the upstream and downstream halves of the track is also checked to reduce the background of fake track coming from misinterpretation of decays in the spectrometer. The upstream momentum, p_u, using only hits in the W1, W2 and W3 chambers and the downstream momentum, p_d, using only hits in the W3, W4 and W5 chambers, are calculated. Then the upstream and downstream momentum asymmetry Δ_{ud} is defined as

$$\Delta_{ud} = \frac{|p_u - p| + |p_d - p|}{p} , \tag{3.7}$$

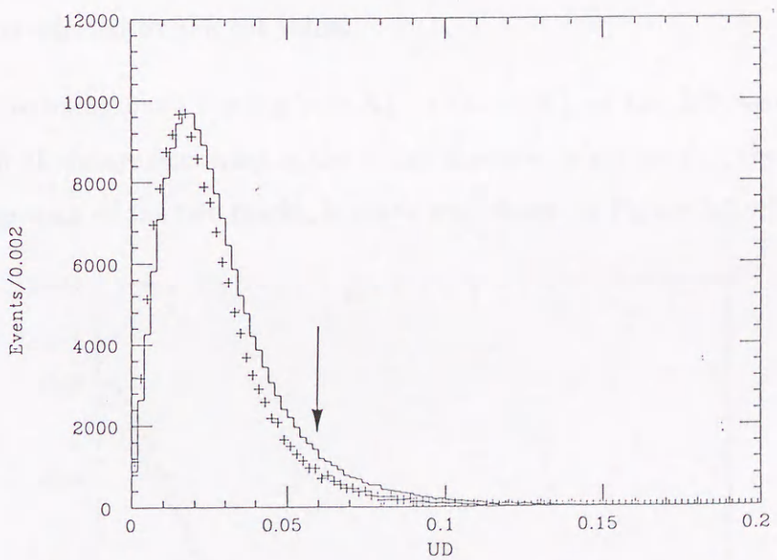

Figure 3.5: Δ_{ud} distribution of for the $K_L^0 \to \pi^+\pi^-$ candidates of the experimental data (the solid line histgram) and the Monte Carlo data (the histgram with simbol "+"). The distributions are normalized to the peak value.

where p is the momentum obtained from hits in all the chambers. Figure 3.5 shows the distribution of Δ_{ud} for $K_L^0 \to \pi^+\pi^-$ events. When a particle decays in the spectrometer leading to a fake track, Δ_{ud} is, in general, different from zero. Therefore, requiring it to

be close to zero reduces the background for $K_L^0 \to \mu e$ events from the $K_L^0 \to \pi e \nu$ decay whose pion decays into a muon in the spectrometer. It is required that $\Delta_{ud} < 0.06$. The cut is effective in removing fake tracks from pion decay in the spectrometer. The loss of genuine pion tracks by this cut is estimated to be 7% by a Monte Carlo simulation for the decay $K_L^0 \to \pi^+\pi^-$ as shown in Figure 3.5. Only the tracks which survive the cuts mentioned above are used in the subsequent analysis.

3.3 Event Selection

In order to eliminate background and select good events associated with K_L^0 decays, the following cuts are applied to the reconstructed events. The event selection criteria used for this analysis are summarized in Table 3.2.

The $K_L^0 \to \pi^+\pi^-$ candidates were used to make the solid line histograms shown in the section. Also Monte Carlo results are shown on the same histograms by the symbol "+", and arrows indicate the cut position. The distributions are normalized with the number of events selected by the cut value.

- To eliminate background coming from $K_L^0 \to \pi e \nu$ or $K_L^0 \to \pi \mu \nu$ followed by π decay to $\mu\nu$ with all decays occurring in the decay chamber, a cut on Δ_v, the distance at closest approach of the two tracks, is made and shown in Figure 3.6 with arrow.

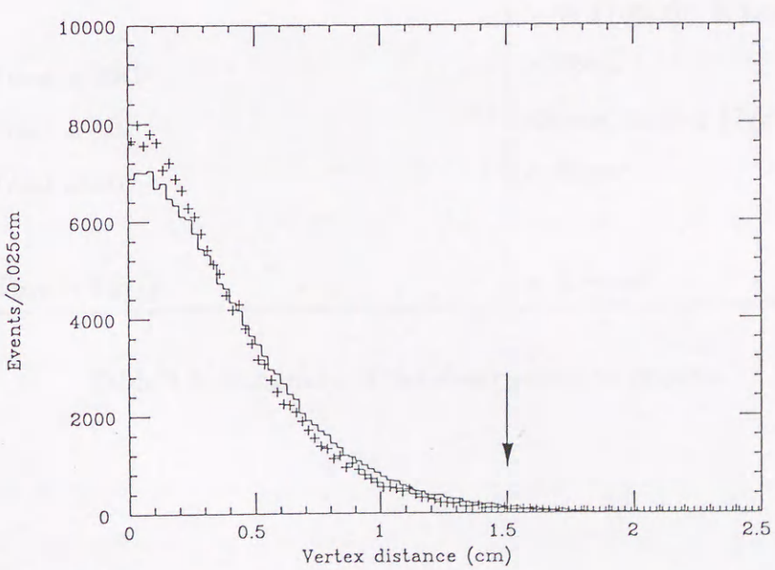

Figure 3.6: Distribution of the distance at closet approach of the two tracks.

Description of Cut	Cut Value
Vertex distance	$< 1.5cm$
Vertex z	$-1000cm <$ and $< 0cm$
Collimation angle limit	$< 9mrad$
Momentum balance $(p_L - p_R)/(p_L + p_R)$	< 0.5
Maximum momentum	$< 4.5GeV/c$
X aperture of vacuum window	$28cm <$ and $< 126cm$
X aperture of magnet	$> 42cm$
Y aperture of magnet	$< 49.5cm$
$\lvert X_{track\ at\ H1} - X_{C\ of\ H1}\rvert$	$< 4.0cm$
$\lvert X_{track\ at\ EM} - X_{CG\ of\ EM}\rvert$	$< 5.5cm$
$X_{track\ at\ EM}$	$> 48.43cm$ for L arm
	$> 49.27cm$ for R arm
$\lvert Y_{track\ at\ EM}\rvert$	$< 72cm$
$X_{track\ at\ M1}$	$45cm <$ and $< 177cm$
$\lvert Y_{track\ at\ M1}\rvert$	$< 80cm$
$\lvert T_{H1L} - T_{H1R}\rvert$	$< 2.5nsec$

Table 3.2: Summary of the event selection criteria

- Figure 3.7 shows the vertex position distribution along the z-axis. It is required that the decay vertex must lie in the decay chamber as indicated with arrows.

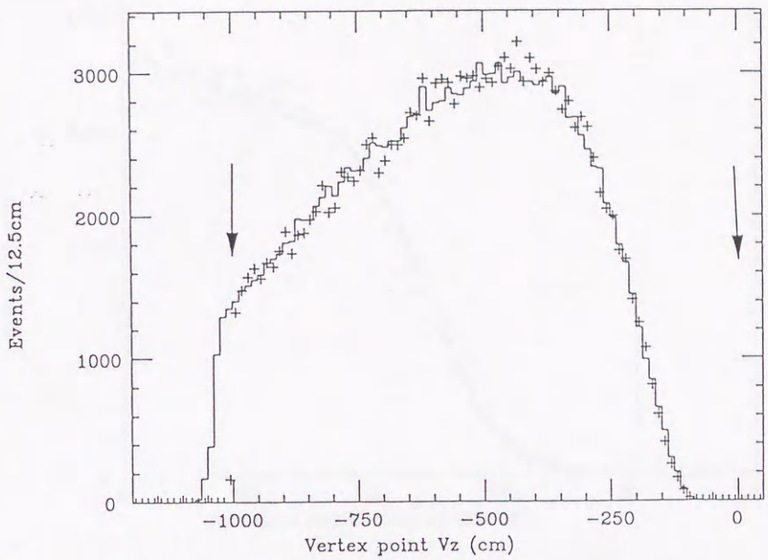

Figure 3.7: Distribution of the vertex position along the z-axis.

- Since the K_L^0 beam is collimated so as to lie within $(7mrad)^2$, a cut is made at $(9mrad)^2$ taking into account smearing by the finite target size and the resolution of the reconstructed angle. Figure 3.8 shows the distribution of the direction angle squared between the vertex-to-target and the beamline, and the cut is applied as indicated by the arrow.

- Figure 3.9 shows the distribution of the reconstructed K_L^0 momentum, and Figure 3.10 shows the momentum distribution of pions. The momentum of the daughter particle is required to be less than $4.5GeV/c$– the momentum region where electrons can be identified ($4.5GeV/c$ corresponds to the momentum threshold of the Čerenkov counter for muons).

- the momentum balance $(p_L - p_R)/(p_L + p_R)$ between the left and right particles is shown in Figure 3.11, and should be within ± 0.5.

- Cuts are made the aperture of the vacuum window and the magnet. Figure 3.12 illustrates the x position of the track at the vacuum window, which has to be greater than $28cm$ and less than $126cm$. Tracks very close to the spectrometer magnet pole

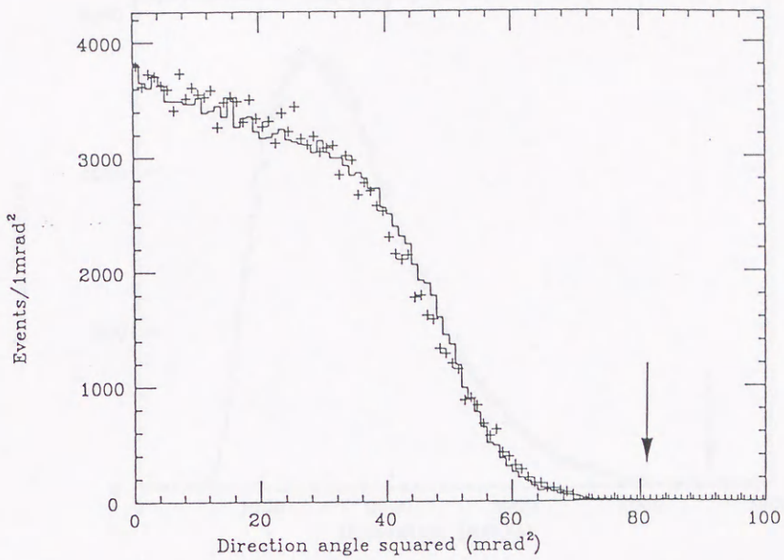

Figure 3.8: Distribution of the direction angle squared between the vertex-to-target and the beamline.

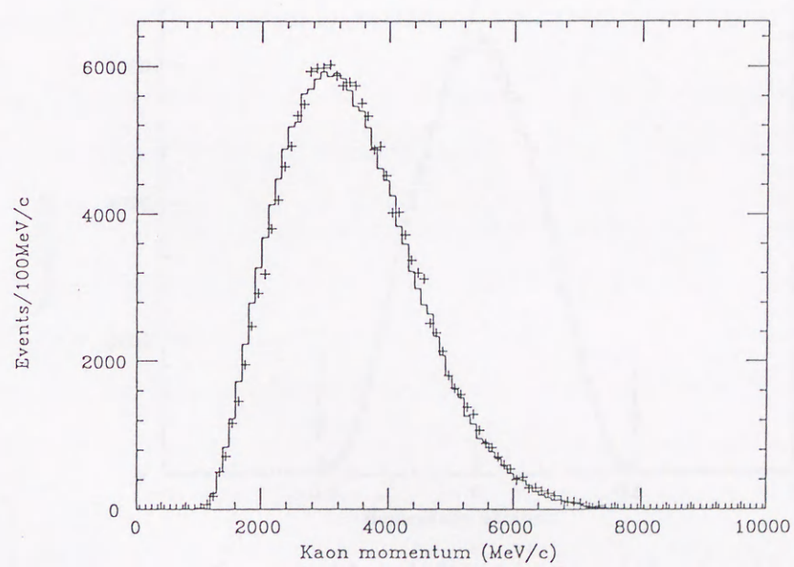

Figure 3.9: Distribution of the reconstructed K_L^0 momentum.

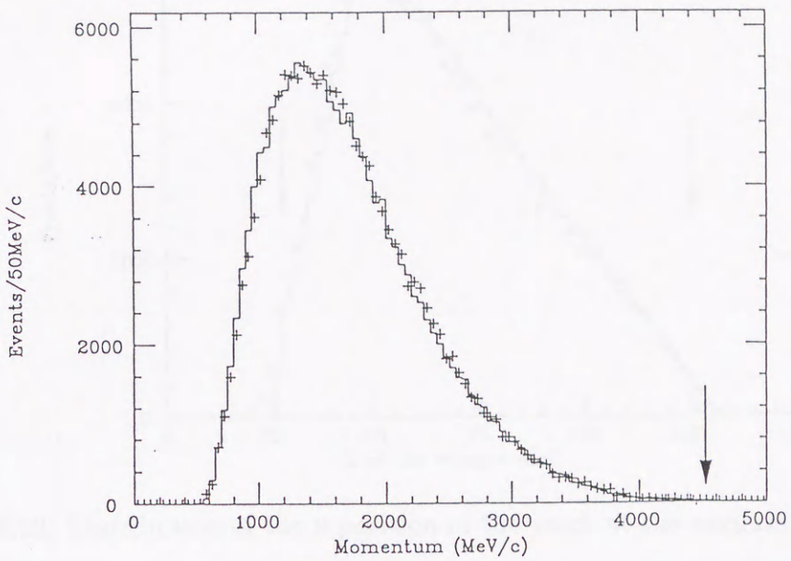

Figure 3.10: Momentum distribution of pions.

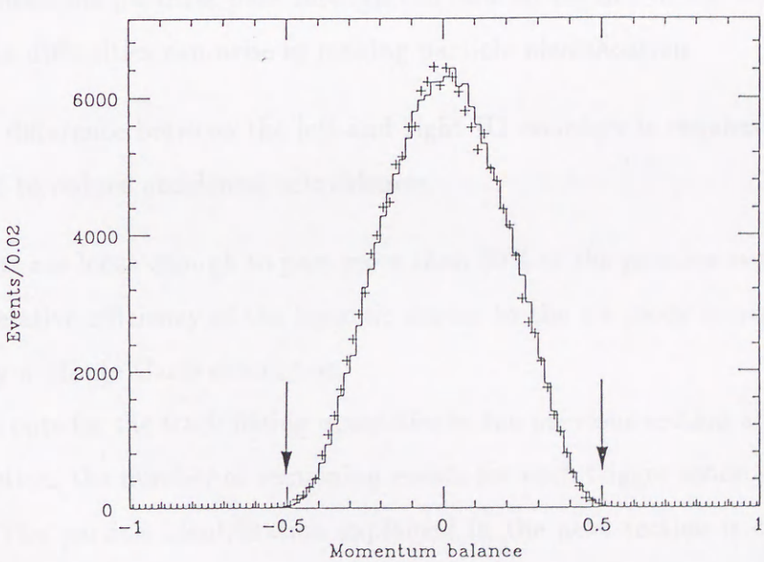

Figure 3.11: Distribution of the momentum balance $(p_L - p_R)/(p_L + p_R)$ between the left and right particles.

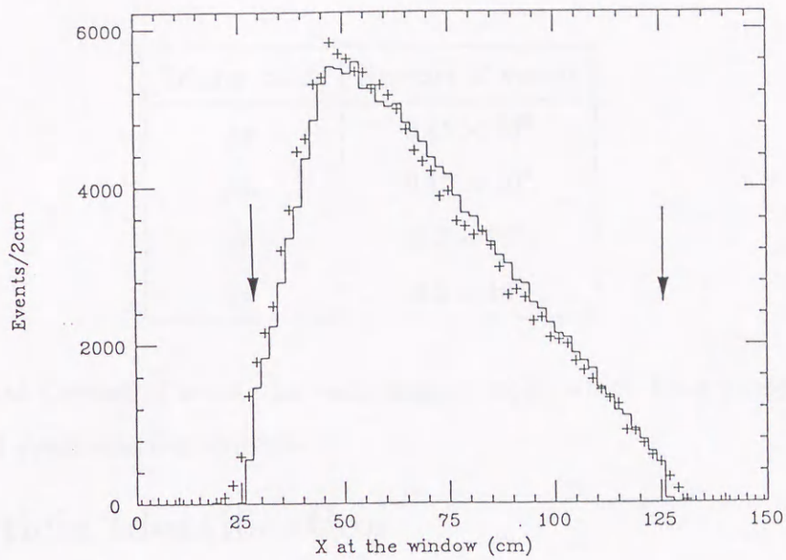

Figure 3.12: Distribution of the x position of the track at the vacuum window.

faces or coils should be rejected, since the field becomes very strong. The track position in x at the entrance of the first magnet must be more than $5.5cm$ away from the inner pole face, and the y position has to be more than $0.5cm$ away from the top and bottom pole faces.

- It is required the particles pass through the fiducial regions of the lepton counters. Otherwise difficulties can arise in making particle identification.

- the time difference between the left and right H1 counters is required to be within $\pm 2.5nsec$ to reduce accidental coincidences.

These cuts are loose enough to pass more than 99% of the genuine events, and their effect on the relative efficiency of the leptonic modes to the $\pi\pi$ mode is negligibly small, as indicated by a Monte Carlo simulation.

After the cuts for the track fitting quantities in the previous section and event selection in this section, the number of remaining events for each trigger mode is summarized in Table 3.3. The particle identification explained in the next section is carried out for the remaining events, and we obtain the final results for μe , ee , $\mu\mu$ and $\pi\pi$, respectively, which are described in the next chapter.

Trigger mode	Number of events
μe	0.45×10^6
$\mu\mu$	0.15×10^6
ee	3.0×10^6
$\pi\pi$	3.5×10^6

Table 3.3: Total number of events for each trigger mode which have passed the track quality cut and event selection criteria

3.4 Particle Identification

The reconstructed tracks in the spectrometer are extrapolated to the particle identification counters, and a search is made for proper signals in them along the extrapolated track. Each counter has criteria for identifying particles, and they are calibrated by using well-defined samples from semileptonic K decays, K_{l3}, included in the $\pi\pi$ trigger data. Discussion about the calibration will be given in section 4.3. However, it is worth mentioning that the calibration using these samples simultaneously collected is very important to reduce the systematic errors due to the running condition.

3.4.1 Proper Signal in the Muon Identifier

A search is made for proper signals in the muon hodoscopes from M1 to M4. Signals in M1 and M2 are considered if the center of the counter having a signal lies within $33cm$ of the x position expected from the extrapolated track and the meantime from the top and bottom photomultipliers lies within $2.5nsec$ of the time expected on the basis of H1. Signals in M3 and M4 are considered if the center of the counter with a signal lie within $42cm$ of the y position expected from the extrapolated track and the time including an x-dependence correction depending lie within $3nsec$ of the time expected from H1. Then the hit pattern from M1 to M4 is checked, and the last hodoscope containing such a signal is determined. On the other hand, the last hodoscope which a muon can penetrate depend on the momentum of the track. In order to be identified as a muon a track is required to have a signal in the last hodoscope where one is expected. Figures 3.13 (a) to (c) show

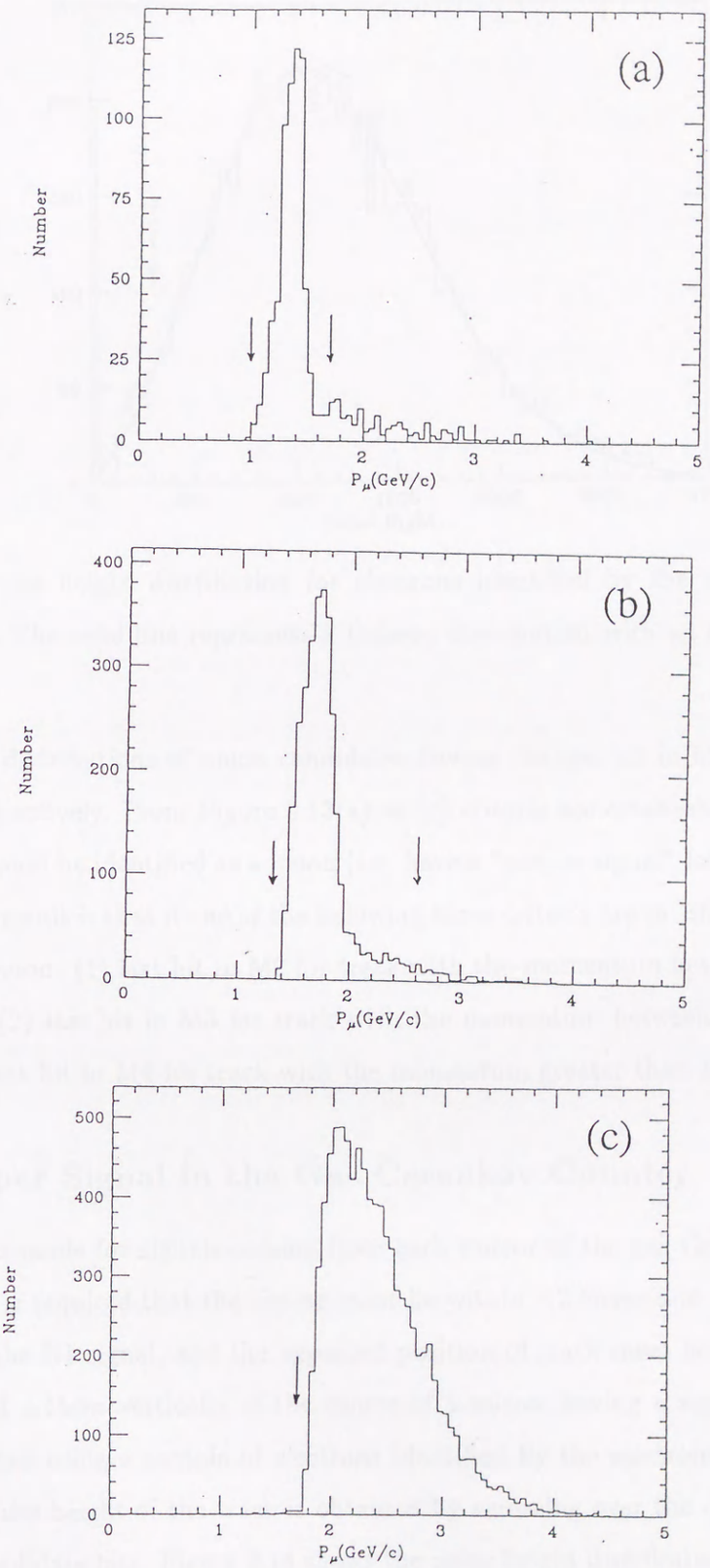

Figure 3.13: Momentum distributions of muon candidates having the last hit in (a)M2, (b)M3 and (c)M4.

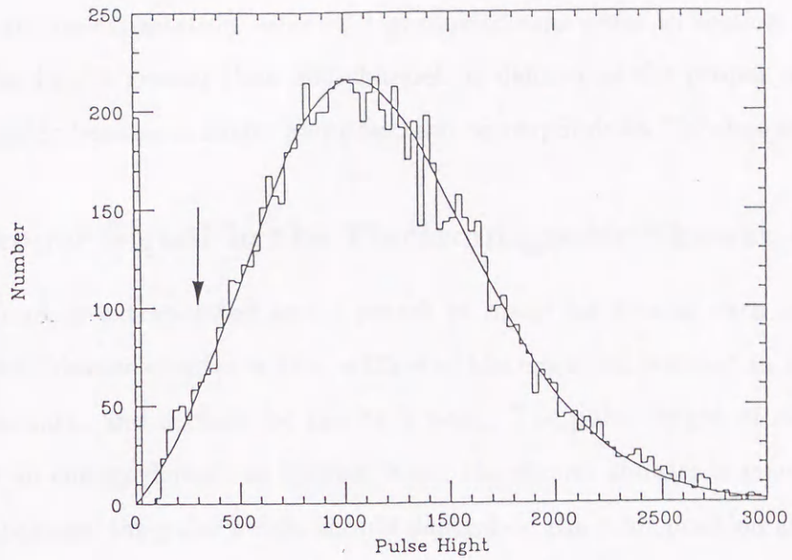

Figure 3.14: Pulse height distribution for electrons identified by the electromagnetic shower counter. The solid line represents a Poisson distribution with an assuming mean value of 5.

the momentum distributions of muon candidates having the last hit in M2, M3 and M4 hodoscopes, respectively. From Figure 3.13(a) to (c) criteria are established for deciding when a track should be identified as a muon (i.e. have a "proper signal" for a muon in the identifier). The result is that if one of the following three criteria are satisfied, the track is identified as a muon: (1) last hit in M2 for track with the momentum between $1.0GeV/c$ and $1.7GeV/c$, (2) last hit in M3 for track with the momentum between $1.3GeV/c$ and $2.6GeV/c$, (3) last hit in M4 for track with the momentum greater than $1.7GeV/c$.

3.4.2 Proper Signal in the Gas Čerenkov Counter

A search is made for signals coming from each mirror of the gas Čerenkov counter during which it is required that the timing must lie within $-2.5nsec$ and $3.0nsec$ of that expected from the H1 signal, and the expected position of track must lie within $\pm 40cm$ horizontally and $\pm 45cm$ vertically of the center of a mirror having a signal. The ADC value is calibrated using a sample of electrons identified by the electromagnetic shower counter. The pulse height of the track is obtained by summing over the calibrated ADC values of the candidate hits. Figure 3.14 shows the pulse height distribution for electrons. This figure agrees with a Poisson distribution with an assumed mean value of 5, and this

is smaller than the expectation value of 9 photoelectrons given in section 2.4. A signal with the pulse height greater than 300 channels is defined as the proper one in the gas Čerenkov counter because a single photoelectron corresponds to 200 channels.

3.4.3 Proper Signal in the Electromagnetic Shower Counter

Each track is extrapolated and a search is made for hits in each module of the electromagnetic shower counter within $\pm 12cm$ of the expected position in x for the front part of the counter and $\pm 16cm$ for the back part. The pulse height of each module is converted to an energy deposit as follows. Since the shower counter is viewed from both the top and bottom, the pulse height should depend on the y hit position as a hyperbolic function. Considering this dependence, the ADC value of the hit module is converted to an energy deposit by

$$E = \frac{ADC}{A_u e^{(y-y_0)/\lambda} + A_d e^{-(y+y_0)/\lambda}}, \tag{3.8}$$

where A_u and A_d are energy scale factors of the top and bottom photomultipliers, which are calibrated with a sample of electrons identified by the gas Čerenkov counter. λ denotes a light attenuation length [3] which was measured by viewing from one end in calibration runs. y is the vertical hit position at the shower counter expected for the track, and y_0 is the y coordinate of the end of the counter end. The energy deposit for the front and back parts is calculated by summing over all the hit modules. The total energy deposit is obtained by summing the front and back ones, which share the energy in the ratio of 10 to 8, which is determined empirically so as to minimize the energy resolution. Then, a signal with the ratio of the total energy deposit(E) to the momentum(P), E/P, greater than 0.7 is regard as a proper one. Figure 3.15 shows the E/P distribution for two samples of electrons and pions which are distinguished by the Čerenkov and muon counters. Furthermore, lower limits of $139MeV$, $44MeV$ and $500MeV$ are imposed on the front, back and total energy deposit for the proper signal to discriminate electrons from other minimum ionizing particles such as muons or pions.

[3] The attenuation length was obtained to be about $1.5m$ for the front part and about $2.0m$ for the back part.

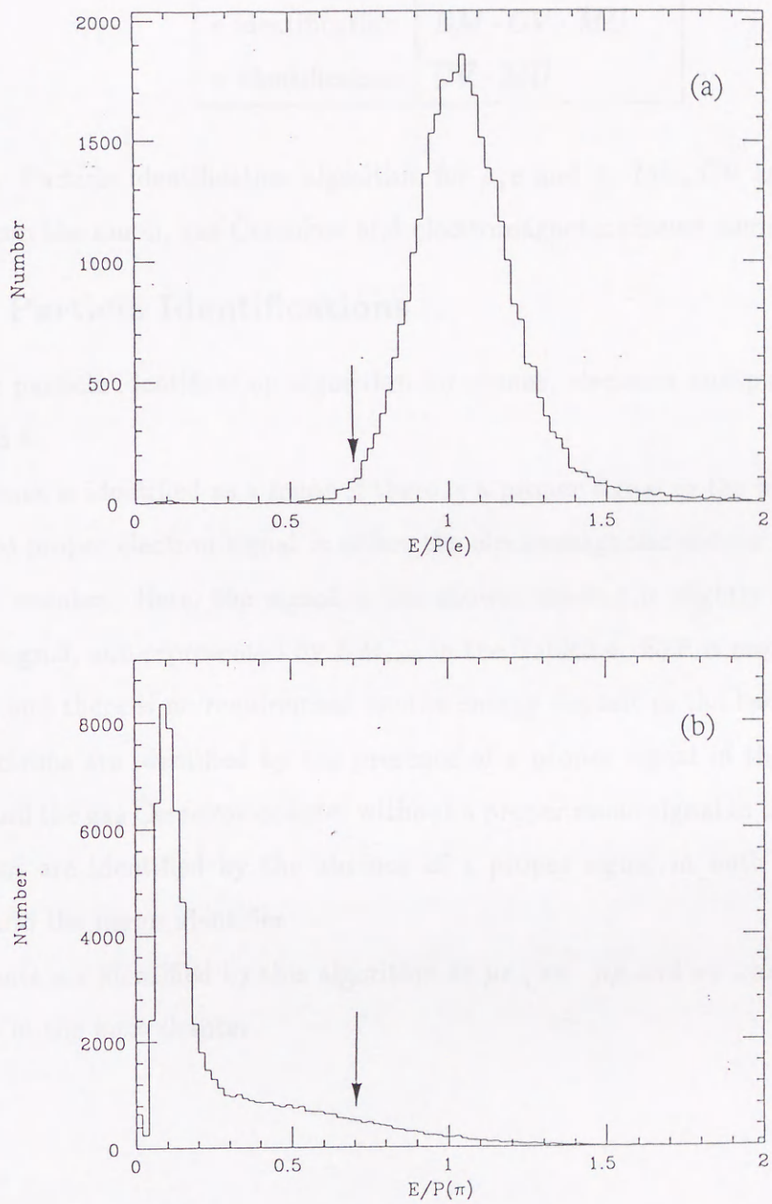

Figure 3.15: E/P distributions (a)for electrons and (b)for pions.

particles	Definition
μ identification	$MU \cdot \overline{CV} \cdot \overline{EM}_{veto}$
e identification	$EM \cdot CV \cdot \overline{MU}$
π identification	$\overline{CV} \cdot \overline{MU}$

Table 3.4: Particle identification algorithm for μ, e and π. MU, CV and EM denote the signals from the muon, gas Čerenkov and electromagnetic shower counters, respectively.

3.4.4 Particle Identifications

The particle identification algorithm for muons, electrons and pions is summarized in Table 3.4.

A track is identified as a muon if there is a proper signal in the muon identifier and there is no proper electron signal in either the electromagnetic shower counter or the gas Čerenkov counter. Here, the signal in the shower counter is slightly different from the ordinary signal, and represented by EM_{veto} in the Table3.4. E/P is required to be greater than 0.6, and there is no requirement for the energy deposit in the back part.

Electrons are identified by the presence of a proper signal in the both the shower counter and the gas Čerenkov counter without a proper muon signal in the muon identifier.

Pions are identified by the absence of a proper signal in both the gas Čerenkov counter and the muon identifier.

Events are identified by this algorithm as μe , ee , $\mu\mu$ and $\pi\pi$, and the final results are given in the next chapter.

Chapter 4

Final Results

The final results for dilepton events are shown in this chapter. In order to obtain the branching ratios of $K_L^0 \to \mu e$, $K_L^0 \to ee$ and $K_L^0 \to \mu\mu$, the single event sensitivity for each mode should be calculated. The single event sensitivity for $K_L^0 \to \mu e$ is given by,

$$S_{\mu e} = B_{\pi^+\pi^-} \cdot \frac{1}{N_{\pi^+\pi^-}} \cdot \frac{A_{\pi^+\pi^-}}{A_{\mu e}} \cdot \frac{\epsilon_{\pi^+\pi^-}}{\epsilon_{\mu e}} \cdot C, \tag{4.1}$$

where $B_{\pi^+\pi^-} = 0.203\%$ is the branching ratio of the decay $K_L^0 \to \pi^+\pi^-$, and $N_{\pi^+\pi^-}$ is the number of $K_L^0 \to \pi^+\pi^-$ events. $A_{\mu e}$ and $A_{\pi^+\pi^-}$ denote the acceptances for the $K_L^0 \to \pi^+\pi^-$ and $K_L^0 \to \mu e$ decays, respectively, and they are given by the ratio of the acceptances. $\epsilon_{\mu e}$ and $\epsilon_{\pi^+\pi^-}$ are the particle identification efficiencies. A correction factor C consisting of the trigger loss of pions due to pion-nucleon interactions in the detector (pion absorption rate) and the dead time difference between dilepton trigger and $\pi\pi$ trigger is applied. The sensitivities for the decay $K_L^0 \to ee$ and $K_L^0 \to \mu\mu$ are also obtained in a similar way.

4.1 Counting $K_L^0 \to \pi^+\pi^-$ Events

4.1.1 Number of $K_L^0 \to \pi^+\pi^-$ Events

Since the branching ratio of the decay $K_L^0 \to \pi^+\pi^-$ is relatively high, the number of events obtained was sufficient to determine with a statistical error of about 1%. The $K_L^0 \to \pi^+\pi^-$ events are obtained with particle identification of the pion in both arms according to the criteria described in section 3.4. Figure 4.1 shows a scatter plot of

the effective mass, $M_{\pi^+\pi^-}$, vs. the collinearity angle-squared, θ^2, for a 1000 $\pi\pi$ event sample, where the collinearity angle θ is defined as the angle between the target-to-vertex direction and the K_L^0 momentum reconstructed by the tracking. The $K_L^0 \to \pi^+\pi^-$ events are clustered near the K_L^0 mass and θ^2 near zero. Figure 4.2 shows the projection onto the mass axis of all $\pi\pi$ event candidates with collinearity-squared $\theta^2 < 3mrad^2$, and Figure 4.3 is the projection onto θ^2 axis of the $K_L^0 \to \pi^+\pi^-$ events with $493MeV/c^2 < M_{\pi^+\pi^-} < 502MeV/c^2$. The mass resolution is determined to be $1.28MeV/c^2$ and the θ^2 resolution to be $0.9mrad^2$. Then, the fiducial region is defined as $493MeV/c^2 < M < 502MeV/c^2$ and $\theta^2 < 3mrad^2$, which is about three times the resolution in each case.

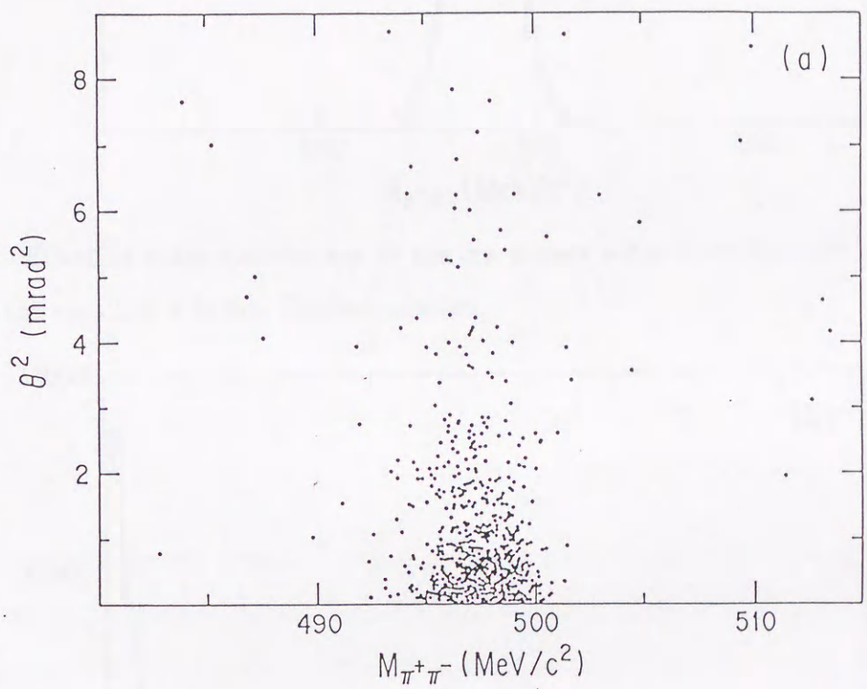

Figure 4.1: Scatter plot of the $\pi\pi$ effective mass, $M_{\pi^+\pi^-}$, vs. the collinearity angle-squared, θ^2, for a 1000 $\pi\pi$ event sample.

The number of $\pi\pi$ events is determined to be 1.59×10^5 by subtracting the background events from the number of events in the fiducial region. A few background events around the $K_L^0 \to \pi^+\pi^-$ cluster can be seen in the scatter plot of Figure 4.1. These events are due to the semileptonic K_L^0 decay, $K_L^0 \to \pi\mu\nu$ and also $K_L^0 \to \pi e\nu$, whose muon and electron are misidentified as pions. In the mass distribution of Figure 4.4, shown on a logarithmic scale, the background has a flat distribution outside the fiducial region. Then,

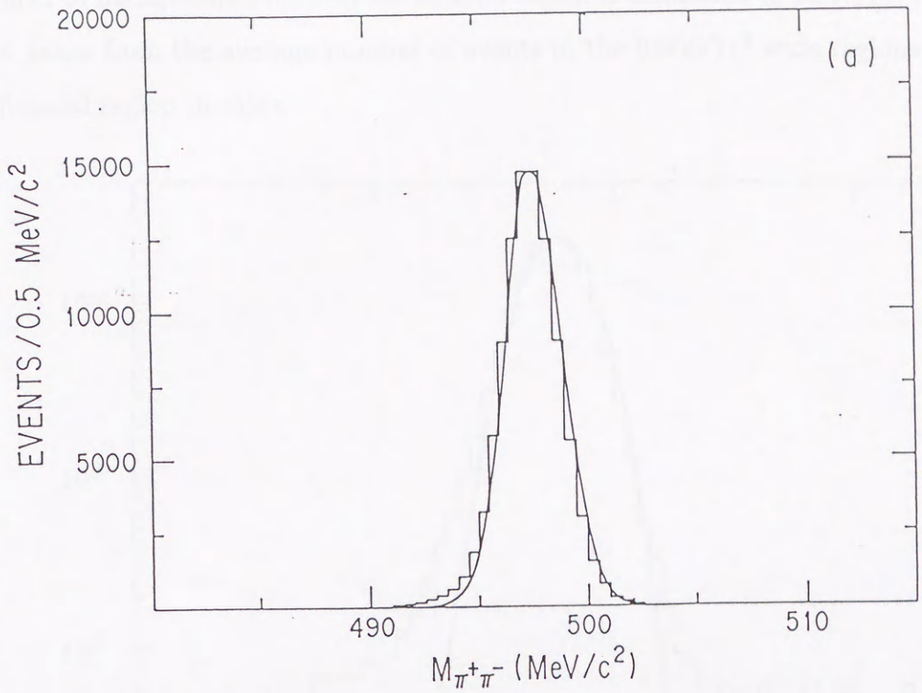

Figure 4.2: Effective mass distribution of the $\pi\pi$ events with $\theta^2 < 3mrad^2$. Solid line represents the result of a Monte Carlosimulation.

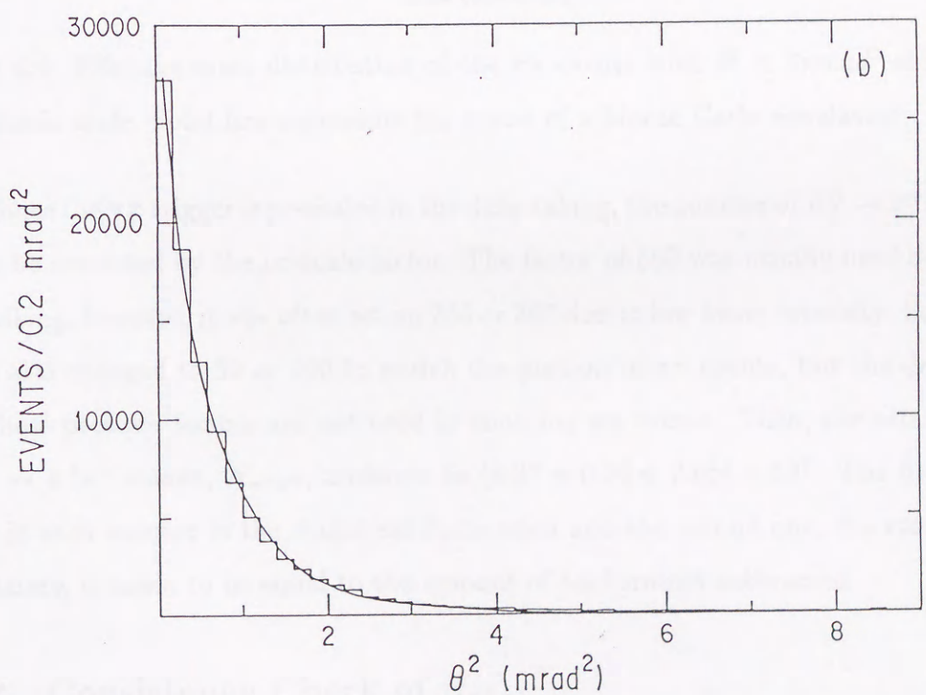

Figure 4.3: θ^2 distribution of the $\pi\pi$ events with $493MeV/c^2 < M_{\pi^+\pi^-} < 502MeV/c^2$. Solid line represents the result of a Monte Carlo simulation.

the number of background events in the fiducial region is estimated to be 1.51×10^3 events which it taken from the average number of events in the $9MeV/c^2$ wide regions adjacent to the fiducial region in mass.

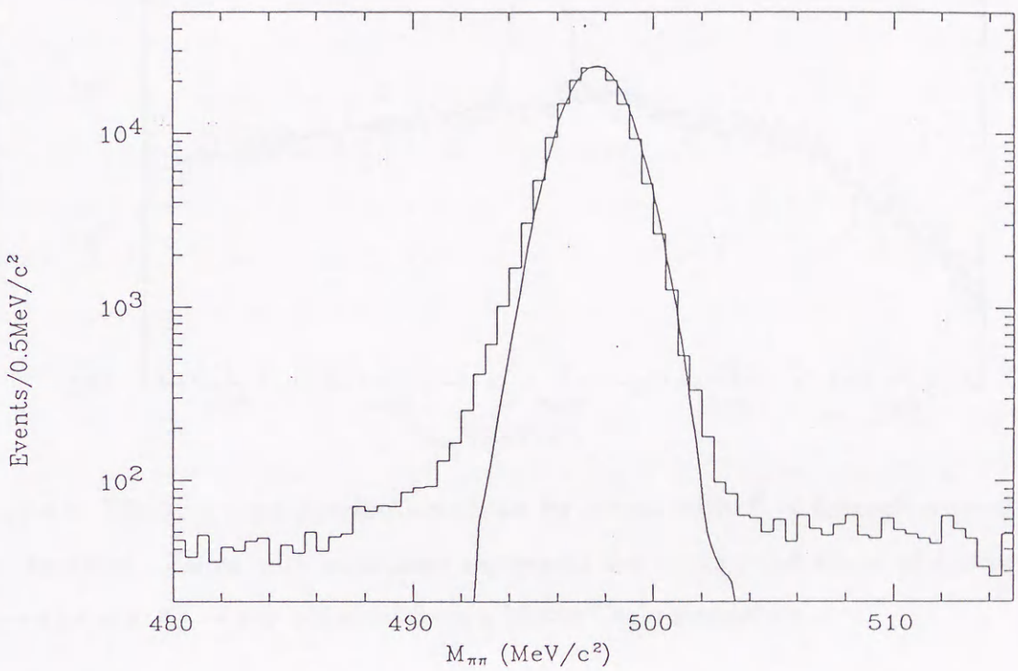

Figure 4.4: Effective mass distribution of the $\pi\pi$ events with $\theta^2 < 3mrad^2$ shown on a logarithmic scale. Solid line represents the result of a Monte Carlo simulation.

Since the $\pi\pi$ trigger is prescaled in the data-taking, the number of $K_L^0 \to \pi^+\pi^-$ events should be corrected by the prescale factor. The factor of 500 was usually used during the data-taking, however, it was often set on 250 or 300 due to low beam intensity. Sometimes it was also changed to 50 or 100 to enrich the portion of $\pi\pi$ events, but the data taken with these prescale factors are not used in counting $\pi\pi$ events. Then, the total number of $K_L^0 \to \pi^+\pi^-$ events, $N_{\pi^+\pi^-}$, amounts to $(6.37 \pm 0.02 \pm 0.06) \times 10^7$. The first uncertainty in each number is the statistical fluctuation and the second one, the systematical uncertainty, is taken to be equal to the amount of background subtracted.

4.1.2 Consistency Check of $N_{\pi^+\pi^-}$

In order to check the internal consistency of $N_{\pi^+\pi^-}$, it is calculated from the $\pi\pi$ mass distribution without requiring particle identification. Figure 4.5 shows the distribution of

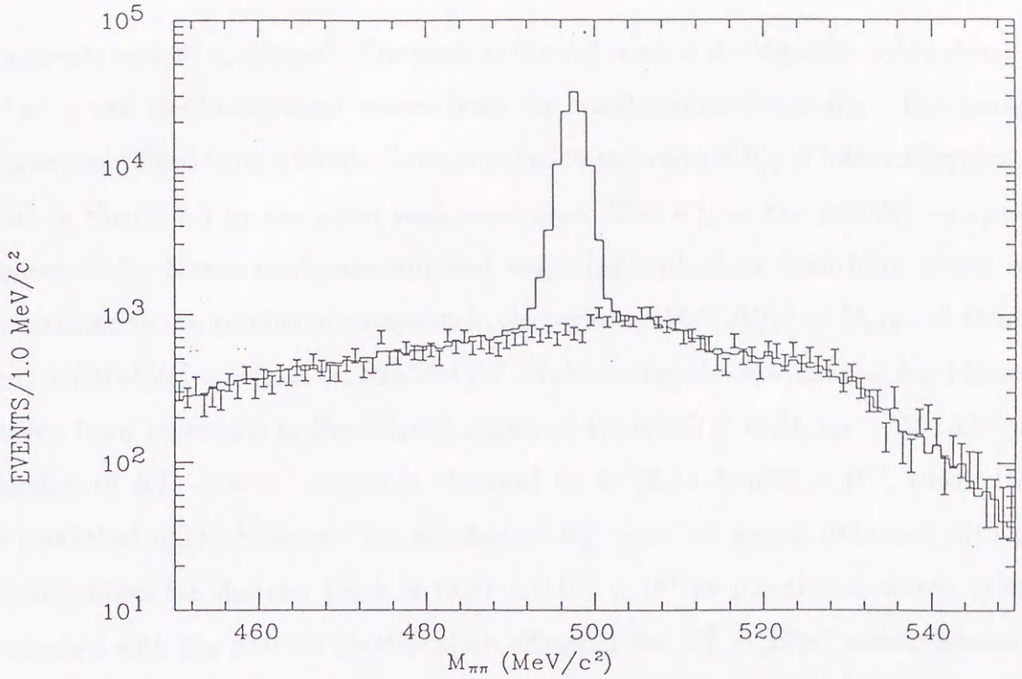

Figure 4.5: Effective mass distribution of the $\pi\pi$ events with $\theta^2 < 3mrad^2$ without the pion identified. Points with error bars represents the background shape of the decays $K_L^0 \to \pi\mu\nu$ and $K_L^0 \to \pi e\nu$ obtained from a Monte Carlo simulation.

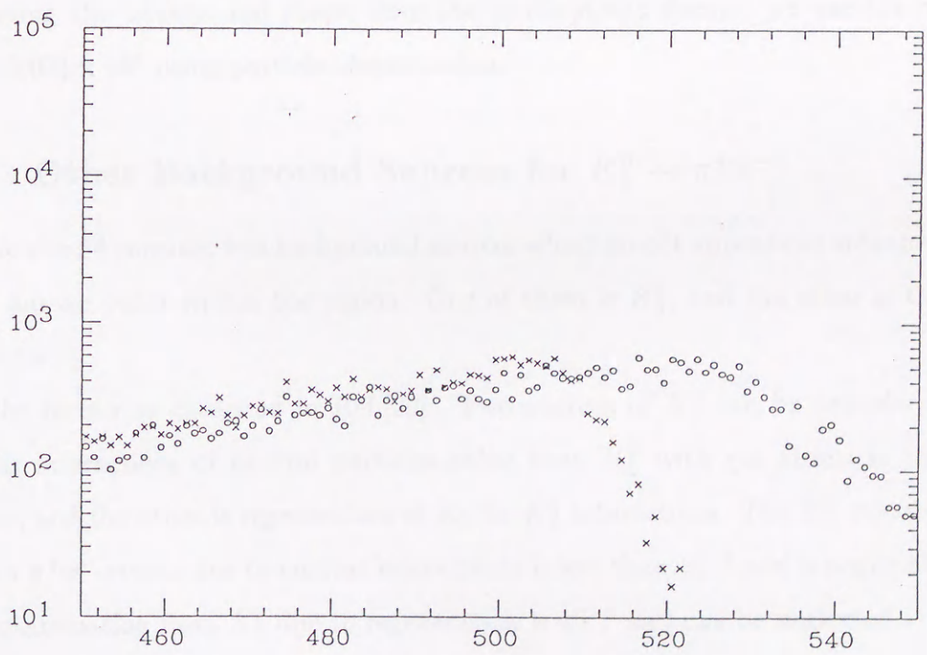

Figure 4.6: Effective mass distribution of $K_L^0 \to \pi\mu\nu$ (×) and $K_L^0 \to \pi e\nu$ (o) events with $\theta^2 < 3mrad^2$ generated by a Monte Carlo simulation.

$\pi\pi$ events with $\theta^2 < 3mrad^2$. The peak at the K_L^0 mass is the signal from the decay $K_L^0 \rightarrow \pi^+\pi^-$, and the background comes from the semileptonic decay K_{l3}. The background shape is obtained from a Monte Carlo simulation assuming a $V-A$ interaction shown with bars in Figure 4.5 by the point with error bars. The $K_L^0 \rightarrow \pi e\nu$ and $K_L^0 \rightarrow \pi\mu\nu$ events generated by Monte Carlo are summed weighting with their branching ratios, and are normalized to the number of $\pi\pi$ events in the regions, $470MeV/c^2 < M_{\pi^+\pi^-} < 485MeV/c^2$ and $510MeV/c^2 < M_{\pi^+\pi^-} < 525MeV/c^2$. Subtracting the normalized K_{l3} Monte Carlo events from $\pi\pi$ events in the fiducial region of $493MeV/c^2 < M_{\pi^+\pi^-} < 502MeV/c^2$, the number of $K_L^0 \rightarrow \pi^+\pi^-$ events is obtained to be $(6.84 \pm 0.02) \times 10^7$, where the error is statistical only. Although the number of $K_L^0 \rightarrow \pi^+\pi^-$ events obtained with particle identification for the two pions is $(6.37 \pm 0.07) \times 10^7$ as mentioned above, it must be corrected with the particle identification efficiency for $K_L^0 \rightarrow \pi^+\pi^-$ events because pions are lost due to misidentification. The correction factor of 0.937 ± 0.003 is calculated in section 4.3, and the number of $K_L^0 \rightarrow \pi^+\pi^-$ events corrected by the efficiency is $(6.80 \pm 0.07) \times 10^7$. The two results obtained by the particle identification and the background subtraction procedures agree well-to within 1%. Since there is a slight discrepancy in reproducing the background shape from the semileptonic decays, we use the result of $(6.80 \pm 0.07) \times 10^7$ using particle identification.

4.1.3 Other Background Sources for $K_L^0 \rightarrow \pi^+\pi^-$

We should consider two background sources which do not appear out side the fiducial region, but do occur within the region. One of them is K_S^0, and the other is the decay $K_L^0 \rightarrow \pi^+\pi^-\gamma$.

The former is discussed in Ref.[20]. Two sources of K_S^0 can be considered. One source is interactions of neutral particles other than K_L^0 with gas atoms in the decay chamber, and the other is regeneration of K_S by K_L^0 interactions. The K_S^0 contamination in $K_L^0 \rightarrow \pi^+\pi^-$ events due to nuclear interactions is less than 10^{-5} and is negligibly small. The contamination from K_S^0 due to regeneration is 10^{-9} and can be neglected.

The latter background, $K_L^0 \rightarrow \pi^+\pi^-\gamma$, can occur through two processes: inner bremsstrahlung (IB), where a decay occurs into two charged pions followed by the emission of a photon from one of the pions; and direct emission (DE), where a photon is emitted

from the $\pi\pi$ decay vertex (or one of the quark lines). For the $K_L^0 \to \pi^+\pi^-$ events, IB is substantial. The $K_L^0 \to \pi^+\pi^-\gamma$ events via an IB process will appear in the somewhat below the K_L^0 mass while those via a DE will appear in a much lower mass region and thus be eliminated. Actually the shape of the mass distribution of $K_L^0 \to \pi^+\pi^-$ events is very slightly inconsistent with the Monte Carlo simulation as seen in Figure 4.2 because the Monte Carlo does not include this process. However, since the decay $K_L^0 \to \pi^+\pi^-\gamma$ is the radiative process of the decay $K_L^0 \to \pi^+\pi^-$, the branching ratio of the decay $K_L^0 \to \pi^+\pi^-\gamma$ is smaller by a factor of the fine structure constant, 1/137. Furthermore the branching ratio of the decay $K_L^0 \to \pi^+\pi^-$ is determined including the decay $K_L^0 \to \pi^+\pi^-\gamma$ via the IB process. Therefore $K_L^0 \to \pi^+\pi^-\gamma$ events via the IB process are included in the $K_L^0 \to \pi^+\pi^-$ events.

4.2 Correcting Acceptance

The acceptance for a certain K_L^0 decay mode is determined by the configuration of the detector system, detection efficiencies and event selection criteria, and slightly varies from that for a different decay mode due to the decay kinematics. Then, this difference must be taken into account in the sensitivity calculation. The acceptances for the $K_L^0 \to \mu e$, ee and $\mu\mu$ decays are calculated with respect to that for the $K_L^0 \to \pi^+\pi^-$ decay using a Monte Carlo simulation.

The Monte Carlo simulation program consist of event generation and its reconstruction. More details are described in the Appendix B. The generated events are converted into the format for real data including the drift chamber resolution which is obtained from experimental data. In order to investigate effects coming from accidental hits on the analysis is determined by using data taken with random triggers during experimental runs under various beam conditions, superimposing them on the Monte Carlo events, analyzing the events using the same track reconstruction program. A decrease in the tracking efficiency for the $K_L^0 \to \pi^+\pi^-$ events with increasing beam intensity as shown in Figure 4.7, which is observed to be 10% to 20%, is well reproduced from these superimposed Monte Carlo data. Although it is found that high beam intensity, due to the number of accidental hits, lead to a considerably decrease in the efficiency of track reconstruction, the effect on the relative acceptances is found to be smaller than 0.2% due to cancelation

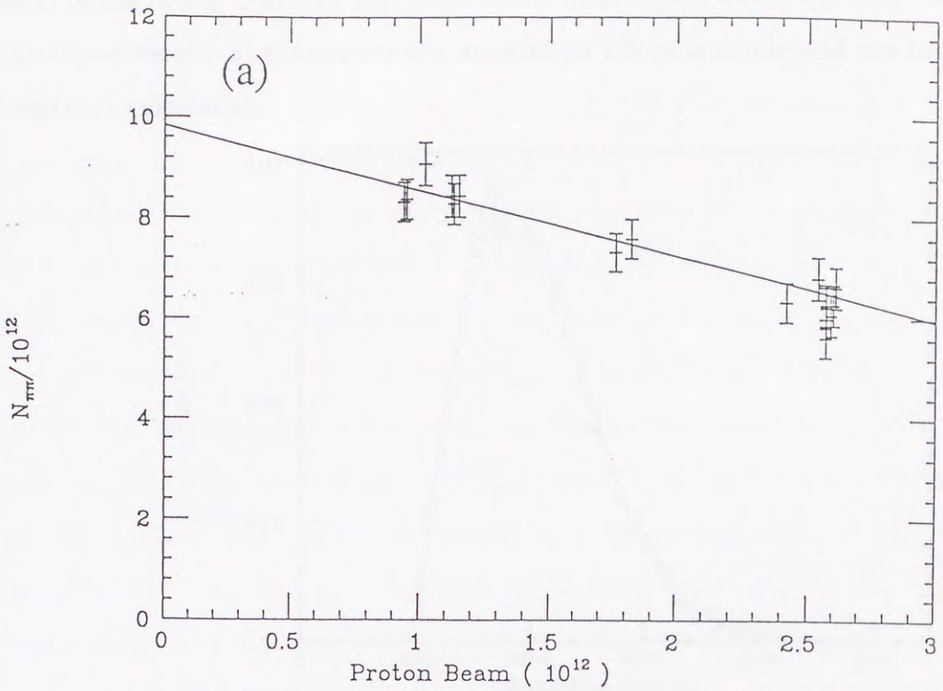

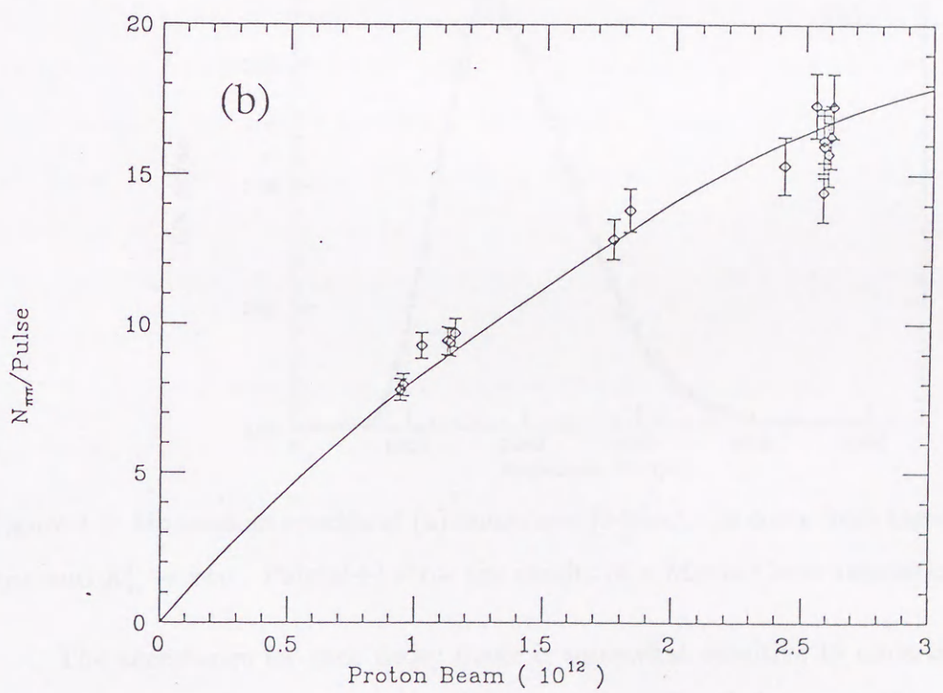

Figure 4.7: Tracking efficiencies for the $K_L^0 \to \pi^+\pi^-$ events as a function of the beam intensity. They are represented by (a)the number of $K_L^0 \to \pi^+\pi^-$ events per 10^{12} protons and (b) that per pulse. Solid line represents the results of a Monte Carlo simulation which is normalized at $1 \times 10^{12} ppp$.

effects in the ratios. Another effect due to the dead anode wires, typically 10 out of 4864, is also considered. These corrections amount to 1% as a whole and are included in the acceptance calculation.

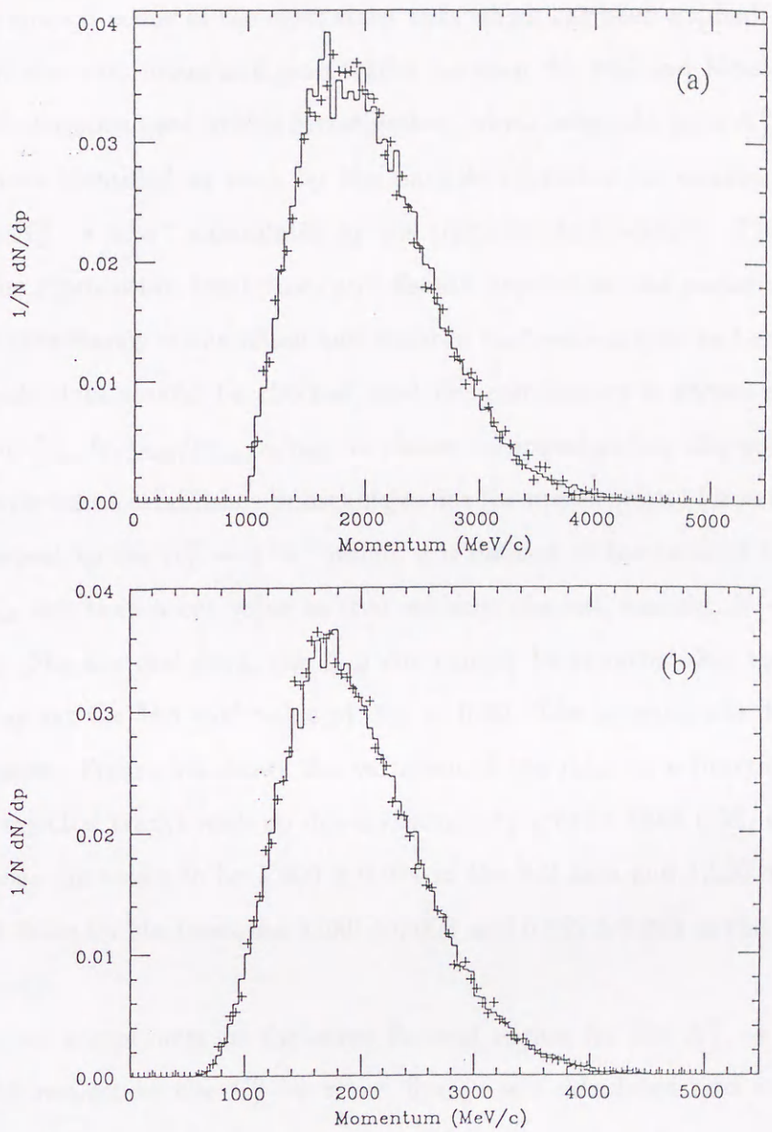

Figure 4.8: Monemtum spectra of (a)muons and (b)electrons come from the decays $K_L^0 \to \pi\mu\nu$ and $K_L^0 \to \pi e\nu$. Points(+) show the results of a Monte Carlo simulation.

The acceptance for each decay mode is somewhat sensitive to uncertainties in the absolute values of the integral magnetic field strength. Small changes in the magnetic field $\Delta B/B$ would lead to small shifts in the K_L^0 mass reproduced by the $K_L^0 \to \pi^+\pi^-$ events. The shift of the K_L^0 mass expected with the accuracy of magnetic field measurements of this experiment is less than 0.04%. Therefore, the correction due to miscalibration in the

magnetic field measurement procedure is negligible.

The acceptance is also a function of the cut variables. The effect of the cut on the upstream and down momentum asymmetry, Δ_{ud}, defined in section 3.2 is investigated on the acceptance since it is one of the most strict cuts which has been applied. This effect is investigated for electron, muon and pion tracks between the real and Monte Carlo data. The muons and electrons used in this investigation, which originate from K_L^0 semileptonic decay, were those identified as such by the particle identification counters. Pions are obtained from $K_L^0 \to \pi^+\pi^-$ candidates by the particle identification. The size of Δ_{ud} is related to the momentum resolution, and should depend on the particle momentum. Therefore, the consistency of the muon and electron momentum spectra between the real and Monte Carlo data should be checked, and the consistency is shown in Figure 4.8. Then, the ratio $(\epsilon_{\mu,e}/\epsilon_\pi)_{data}/(\epsilon_{\mu,e}/\epsilon_\pi)_{MC}$ is chosen in investigating the cut dependence because this experiment establishes branching ratios (or upper limits) for various dilepton modes with respect to the $K_L^0 \to \pi^+\pi^-$ mode. ϵ is defined as the ratio of the number of tracks with Δ_{ud} less than a cut value to that without the cut, namely, $N(<$ a cut value $)/N($ no cut $)$. For the real data, the Δ_{ud} cut cannot be removed due to background, and so there, we set the "no cut" value of Δ_{ud} to 0.20. The error on ϵ is determined by binomial statistics. Figure 4.9 shows the variation of the ratio as a function of the Δ_{ud} cut. Since we rejected tracks with up-down asymmetry greater than 0.06, the correction factors for muons are taken to be 1.000 ± 0.004 in the left arm and 1.003 ± 0.004 in the right arm, and those for electrons are 0.980 ± 0.003 and 0.982 ± 0.003 in the left and right arms, respectively.

The relative acceptances in the same fiducial region for the $K_L^0 \to \mu e$, ee and $\mu\mu$ decays with respect to the $K_L^0 \to \pi^+\pi^-$ decays are calculated and summarized in Table 4.1, where they are calculated requiring the momentum of muons to be greater than $1GeV/c$ because the muon identifier is insensitive to muons with $p < 1GeV/c$.

4.3 Particle Identification Efficiencies

The responses of each counter to electrons, muons and pions are calibrated by using well-defined samples from the semileptonic K decays, K_{l3}, included in the $\pi\pi$ triggered data. In the selection of the K_{l3} events used for the calibration, the cut on the upstream

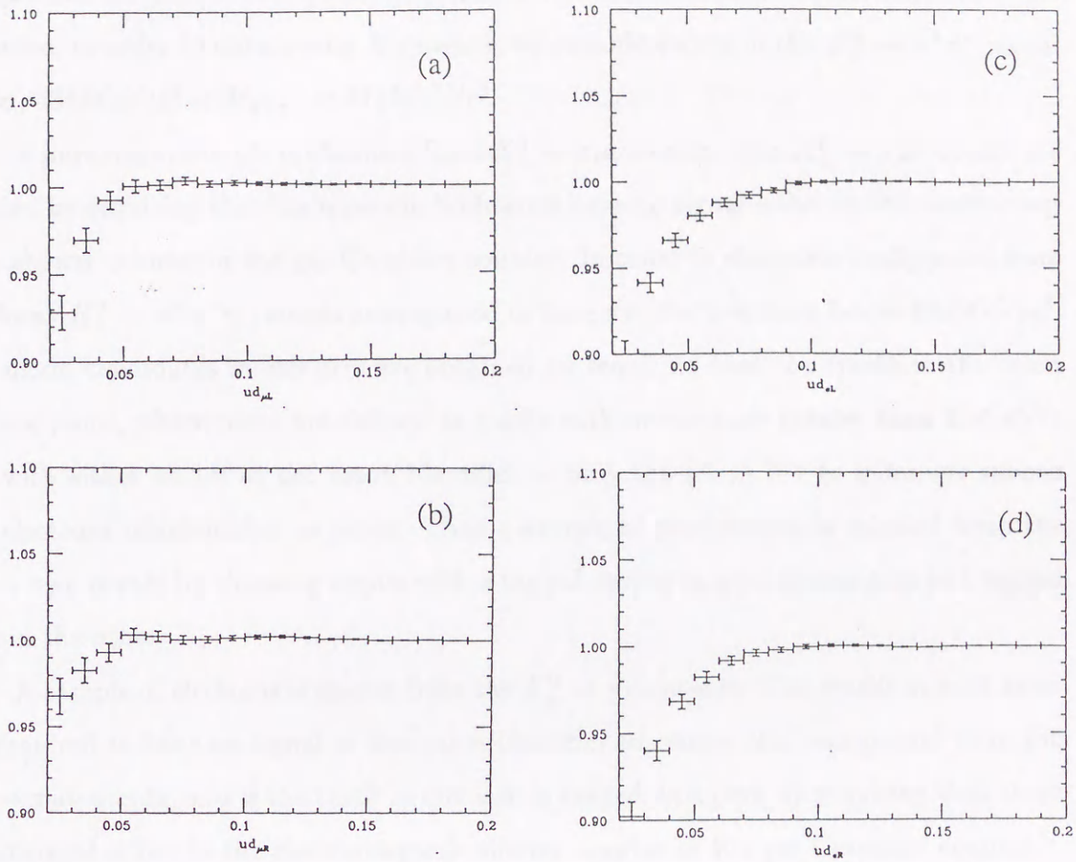

Figure 4.9: Variation of $(\epsilon_{\mu,e}/\epsilon_\pi)_{data}/(\epsilon_{\mu,e}/\epsilon_\pi)_{MC}$ as a function of the Δ_{ud} cut for (a),(b) muons and (c),(d) electrons in the left and right arms, respectively.

decay mode	Acceptance	corrections	$A/A_{\pi\pi}$
$K_L^0 \to \pi^+\pi^-$	$(5.48 \pm 0.02) \times 10^{-3}$	–	–
$K_L^0 \to \mu e$	$(5.04 \pm 0.02) \times 10^{-3}$	1.018 ± 0.004	0.939 ± 0.009
$K_L^0 \to ee$	$(4.94 \pm 0.02) \times 10^{-3}$	1.040 ± 0.004	0.940 ± 0.009
$K_L^0 \to \mu\mu$	$(4.64 \pm 0.02) \times 10^{-3}$	0.997 ± 0.006	0.839 ± 0.013

Table 4.1: Acceptances for the four decay modes, and the corrections for the Δ_{ud} cut.

and downstream momentum asymmetry is removed to increase the number of events. Furthermore, in order to obtain only K_{l3} events, we exclude events in the $K_L^0 \to \pi^+\pi^-$ signal region, $484MeV/c^2 < M_{\pi^+\pi^-} < 511MeV/c^2$.

A pure muon sample is obtained from $K_L^0 \to \pi\mu\nu$ events. The $K_L^0 \to \pi\mu\nu$ events are selected by requiring that the tracks in both arms have no signal either in the electromagnetic shower counter or the gas Čerenkov counter. In order to eliminate background from the decay $K_L^0 \to \pi^+\pi^-\gamma$, events are required to have $\pi\pi$ effective mass below $480MeV/c^2$. The muon candidates in one arm are obtained by requiring that the tracks in the other arm are pions, where pions are defined as tracks with momentum greater than $1.5GeV/c$ and with either no hit in the muon identifier or only the hit in M1 to eliminate muons and electrons misidentified as pions. Thus a sample of pure muons is selected from the $K_L^0 \to \pi\mu\nu$ events by choosing events with a tagged muons in a particular arm and tagged pion in the other.

A sample of electrons is chosen from the $K_L^0 \to \pi e\nu$ events. The tracks in both arms are required to have no signal in the muon identifier to reduce the background from the $K_L^0 \to \pi\mu\nu$ events, and if the track in one arm is tagged as a pion by requiring that there be no signal either in the electromagnetic shower counter or the gas Čerenkov counter.

A sample of pions are also chosen from the $K_L^0 \to \pi e\nu$ events. The pion candidates can be obtained by requiring that the tracks in the other arm are identified as electrons by both the Čerenkov and shower counters.

4.3.1 Gas Čerenkov Counter Efficiency

In order to remove residual contamination in the electron sample used in calibrating the efficiency of the gas Čerenkov counter, the effective mass calculated assigning the pion mass to both tracks is required for the $K_L^0 \to \pi e\nu$ evnets to be greater than $511MeV/c^2$ because the decay $K_L^0 \to \pi\mu\nu$ is not allowed to have the $\pi\pi$ effective mass in the region, $M_{\pi^+\pi^-} > 511MeV/c^2$ kinematically as shown in Figure 4.6. In addition a signal is required in the electromagnetic shower counter for the electron sample. Then, the background contamination of muons and pions for the electron sample is estimated to be around 1.2×10^{-4} and is neglected. Since the efficiency depends on the position of the hit due to variations in the reflective efficiencies of mirrors, the surface of the mirrors is subdivided

into 6×7 meshes, and the efficiency for electrons is determined for each region. Figure 4.10 shows the results. It also varied from one cycle of the experimental run to the next, so all efficiencies are calibrated for each cycle. The responses for pions and muons are also calibarted using the pion and muon samples. Table 4.2 summarizes the efficiencies for electrons, muons and pions which are obtained averaging those calculated for each cycle weighted by the number of $K_L^0 \to \pi^+\pi^-$ events.

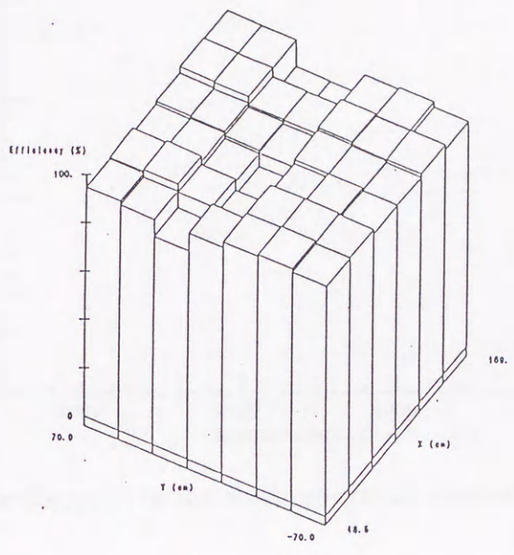

Figure 4.10: Efficieny for electrons in the Čerenkov counter as a function of the hit position.

	symbol	Left arm	Right arm
Efficiency for electrons	ϵ_e^{CV}	$(94.46 \pm 0.27)\%$	$(91.71 \pm 0.27)\%$
Efficiency for muons	ϵ_μ^{CV}	$(0.180 \pm 0.018)\%$	$(0.225 \pm 0.019)\%$
Efficiency for pions	ϵ_π^{CV}	$(0.128 \pm 0.012)\%$	$(0.190 \pm 0.015)\%$

Table 4.2: Efficiencies of the gas Čerenkov counters for electrons, muons and pions

4.3.2 Electromagnetic Shower Counter Efficiency

The efficiency of the electromagnetic shower counter for electrons is determined as a function of the momentum as shown in Figure 4.11 using an electron sample with a proper

signal in the gas Čerenkov counter. The impurity of the electron sample is estimated to be about 2.8×10^{-4} and is negligible small. The efficiencies for muons and pions are obtained using samples of muons and pions. These efficiencies are summarized in Table 4.3.

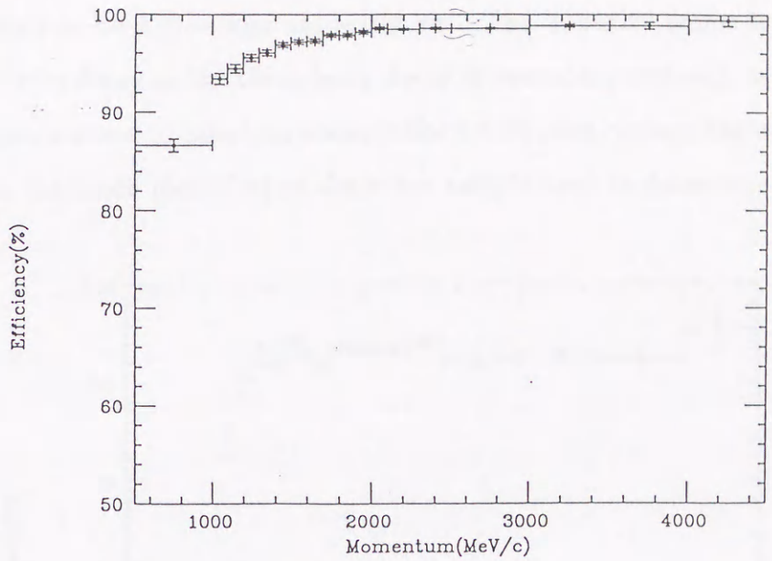

Figure 4.11: Efficieny for electrons in the electromagnetic shower counter as a function of the momentum.

	symbol	Left arm	Right arm
Efficiency for electrons	ϵ_e^{EM}	$(94.09 \pm 0.26)\%$	$(94.40 \pm 0.26)\%$
Efficiency for muons	ϵ_μ^{EM}	$(1.673 \pm 0.054)\%$	$(1.642 \pm 0.052)\%$
Efficiency for pions	ϵ_π^{EM}	$(9.363 \pm 0.073)\%$	$(10.913 \pm 0.079)\%$

Table 4.3: Efficiencies of the electromagnetic shower counter for electrons, muons and pions

4.3.3 Muon Identifier Efficiency

The efficiency of the muon counter is determined as a function of momentum, shown in Figure 4.12, using a muon sample without proper signals in both the gas Čerenkov counter and the electromagnetic shower counter. The purity of the muon sample is estimated to be 99.5% as follows. The contamination of electrons in the muon sample is

negligible since electrons can be rejected redundantly by two independent electron identifiers. The contamination of pions in the muon sample is investigated by imposing on this sample the criteria described in the introduction to this section It is found that a pion contamination of 0.52% is included in the muons. This implies that 0.52% of the events considered to be $K_L^0 \to \pi\mu\nu$ are really $\pi\pi$. The impurity seems to be $\pi\pi$ events from $K_L^0 \to \pi^+\pi^-\gamma$ decay or the three-body decay of vector mesons such as ω. The muon efficiency is renormalized to take into account the 0.52% pion contamination (which realy gives counts in the muon identifier) in the muon sample used to determine the efficiency.

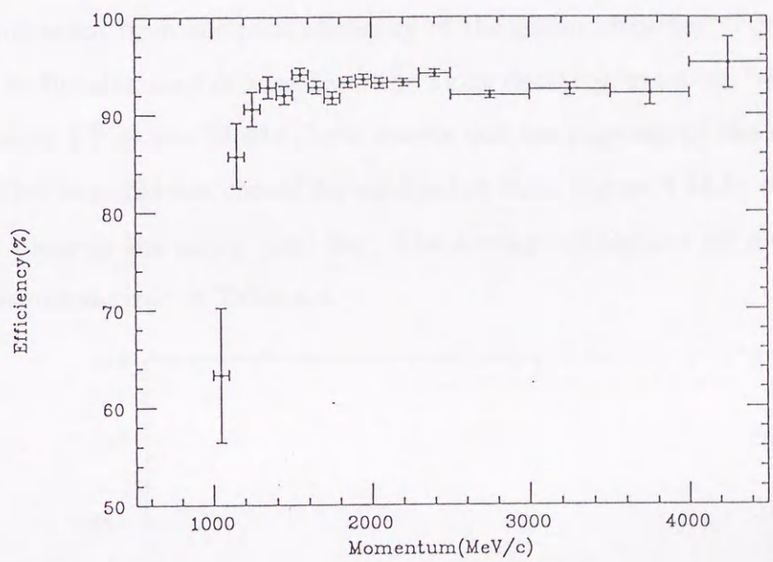

Figure 4.12: Efficieny for muons in the muon identifier as a function of the momentum.

	symbol	Left arm	Right arm
Efficiency for electrons	ϵ_e^{MU}	$(0.242 \pm 0.013)\%$	$(0.257 \pm 0.013)\%$
Efficiency for muons	ϵ_μ^{MU}	$(90.74 \pm 0.27)\%$	$(90.08 \pm 0.27)\%$
Efficiency for pions	ϵ_π^{MU}	$(1.94 \pm 0.29)\%$	$(1.88 \pm 0.29)\%$

Table 4.4: Efficiencies of the muon identifier for electrons, muons and pions

The efficiency for electrons in the muon identifier is obtained using the electron sample with proper signals in both the gas Čerenkov counter and the electromagnetic

shower counter. The efficiency for pions is obtained as a function of momentum as shown in figure 4.13 using a pion sample without proper signals in either the gas Čerenkov counter or the electromagnetic shower counter. The two discontinuities in the figure correspond to the limits at which additional muon hodoscopes should be reached—M3 and M4. Pions which decay to muons after W5 are regarded as pions misidentified as muons, because it is the momentum of the pion which is measured in the spectrometer. On the other hand, Pions which decay to muons before W5 are not treated as pions misidentified as muons because in this case it is the momentum of the muon after pion decay which is measured in the spectrometer.[1] The contribution of muons coming from the pion decay before W5 should be subtracted from the pion efficiency of the muon identifier. Figure 4.14 shows contribution to the efficiency coming from the pions decaying to muons before W5 which is obtained using $K_L^0 \to \pi e \nu$ Monte Carlo events and the response of the muon identifier for muons. This contribution should be subtracted from Figure 4.13 to obtain a proper efficiency for pions in the muon identifier. The average efficiencies for electrons, muons and pions are summarized in Table 4.4.

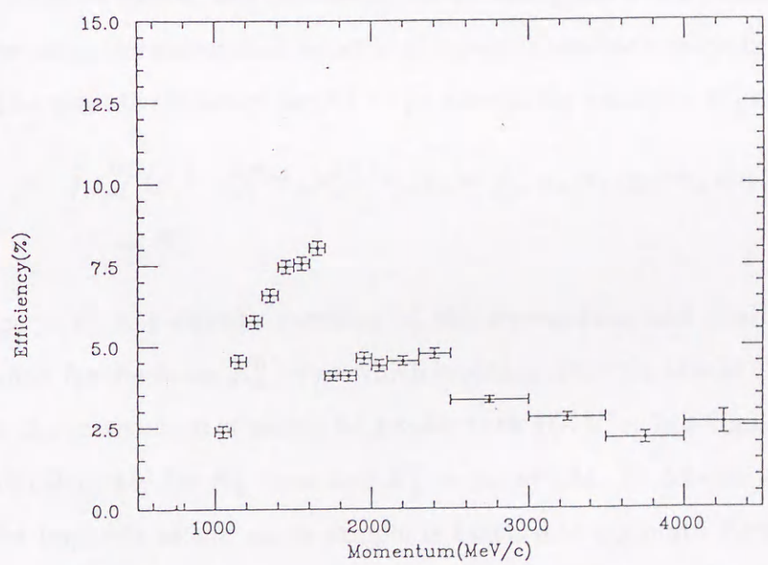

Figure 4.13: Efficieny for pions in the muon identifier as a function of the momentum.

[1]Tracks with pions decaying into muons within the spectrometer are almost rejected in track reconstruction, for those few which survive, there are several possibilities for what the reconstructed momentum value corresponds to but this is not an important effect.

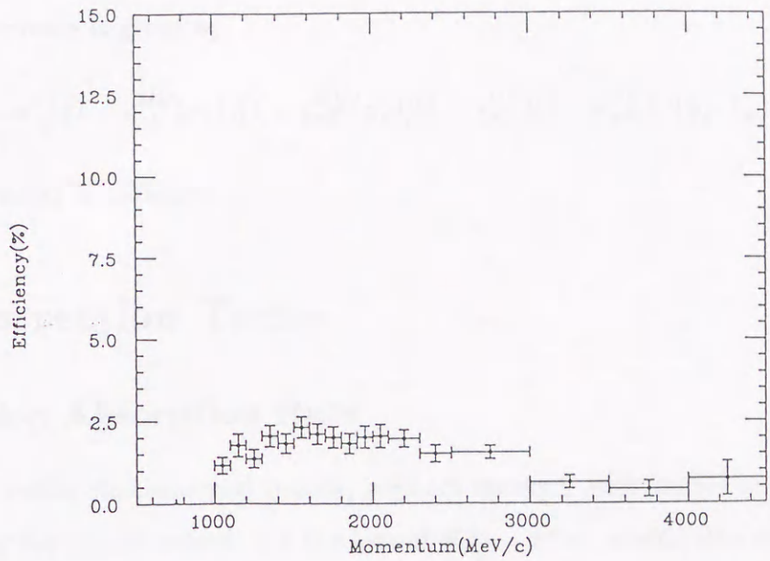

Figure 4.14: Contamination of muons in the pion efficiency in the muon identifier coming from the pions decaying to muons before W5.

4.3.4 Correcting Particle Identification Efficiencies

For the dilepton events, the efficiencies for detecting the two leptons are calculated on the average using the momentum spectra of leptons from each mode in a Monte Carlo simulation. The average efficiency for $K_L^0 \to \mu e$ events, for example, is given by,

$$2\epsilon_{\mu e} = \int \epsilon_{\mu L}^{MU}(p_L) \cdot \epsilon_{eR}^{EM}(p_R)\epsilon_{eR}^{CV}(x_R, y_R)\omega(p_L, p_R, x_R, y_R)dp_L dp_R dx_R dy_R + L \leftrightarrow R,$$

where $\omega(p_L, p_R, x, y)$ is a density function of the momentum and position at the gas Čerenkov counter for the decay $K_L^0 \to \mu e$ which is obtained from a Monte Carlo simulation requiring that the momentum of muons be greater than $1 GeV/c$. In a similar way, average efficiencies are calculated for $K_L^0 \to ee$ and $K_L^0 \to \mu\mu$ events. To determine the efficiency for muons, the impurity of the muon sample is taken into account. Furthermore, since electrons are vetoed by the muon identifier and muons are vetoed by the gas Čerenkov and electromagnetic shower counters, we correct the efficiencies by the veto efficiencies. [2] The corrections are 0.997 for electrons and 0.977 for muons. Then we determine the average values of particle identification efficiencies to be $0.744 \pm 0.005, 0.730 \pm 0.004$ and 0.763 ± 0.006 for $K_L^0 \to \mu e$, ee and $\mu\mu$. The average value of particle identification for

[2] Veto efficiency = 1− efficiency.

$K_L^0 \to \pi^+\pi^-$ events is given by,

$$\epsilon_{\pi^+\pi^-} = \int (1-\epsilon_{\pi L}^{MU}(p_L))(1-\epsilon_{\pi R}^{MU}(p_R))(1-\epsilon_{\pi L}^{CV})(1-\epsilon_{\pi R}^{CV})\omega(p_L,p_R)dp_L dp_R,$$

and 0.937 ± 0.003 is obtained.

4.4 Correction Terms

4.4.1 Pion Absorption Rate

Pions, unlike electrons and muons, interact strongly with nuclei in the material of the detector. We should correct for the loss of $K_L^0 \to \pi^+\pi^-$ events due to trigger failure caused by an interaction of a pion from $K_L^0 \to \pi^+\pi^-$. This is mostly due to material in the hodoscope H1 and the gas Čerenkov counter which is located between H1 and H2. The amount of material upstream from W5 is 4.56×10^{-3} interaction lengths whereas it is the 6.42×10^{-2} between hodoscopes H1 and H2. Thus, pions are absorbed mainly in the material between H1 and H2. Since the nuclei in material can be considered to be isoscalar, the cross section of $\pi^{\pm}N$ may be represented by that of $\pi^{\pm}d$ multiplied by the atomic mass number. Using the $\pi^{\pm}d$ cross section, the pion interaction rate is estimated to be about 10%. But, secondary charged particles may hit the downstream trigger hodoscope H2, and so the actual trigger loss will be smaller than the estimation.

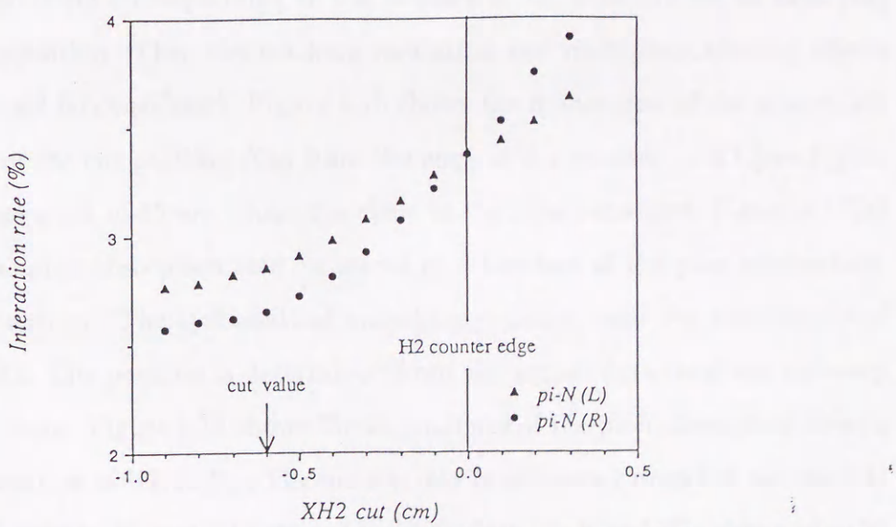

Figure 4.15: Fluctuation of the absorption rate as a function of the cut position X_{H2}.

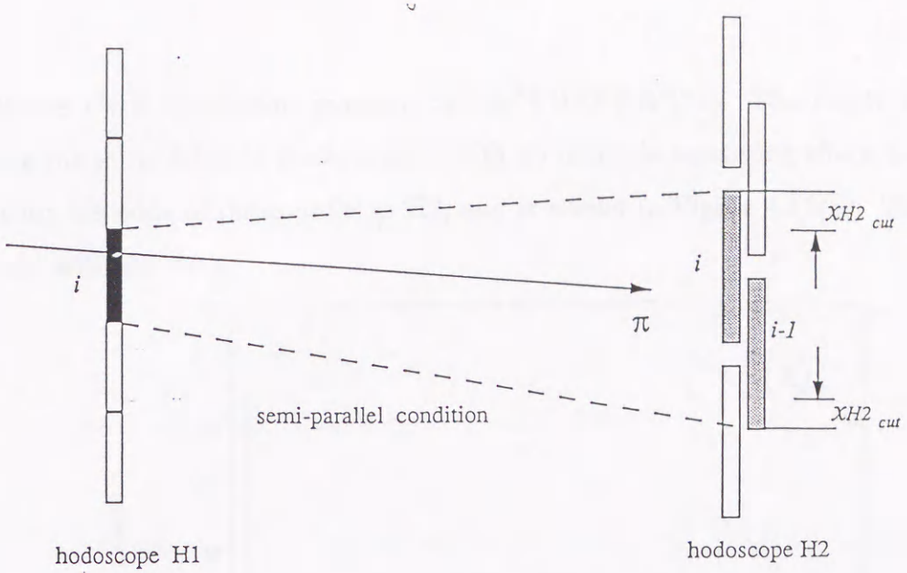

Figure 4.16: Schematic view of the definition of the cut position X_{H2}

We measured the $\pi\pi$ trigger loss between hodoscopes H1 and H2 with the decay $K_L^0 \to \pi e\nu$ in a special run. We made a $\pi e\nu$ trigger, in which at least one hit in the H1 hodoscope was required in one arm and a semi-parallel coincidence and an electron signal were required in one arm. In off-line analysis, tracks in one arm are tagged as pions by requiring electrons in one arm which are identified by requiring a signal in the Čerenkov counter, and pion tracks require no signal in the muon identifier to eliminate muons from $\pi \to \mu\nu$ decays. The pion tracks are extrapolated to the H1 and H2 hodoscopes. The pion absorption rate in the region between H1 and H2 is estimated from the fraction of signal loss in that counter of H2 corresponding to the counter of H1 with the hit as satisfying the semi-parallel condition. Then the tracking resolution and multiple scattering effects of the material should be considered. Figure 4.15 shows the fluctuation of the absorption rate as a function of the cut position X_{H2} from the edge of the counter in H2 (see Figure 4.16, and we impose a cut of $40mm$ where the slope in the figure changes. Figure 4.17(a) shows results of the pion absorption rate measured as a function of the pion momentum. The errors are statistical. The systematical uncertainty comes from the uncertainty of the x position of H2. The position is determined from the actual data, and the accuracy ΔX_{H2} is less than $1mm$. Figure 4.18 shows the dependence of the pion absorption rate on the shift of the x position of H2, ΔX_{H2} The uncertainty is estimated from the variation at the position determined by the actual data as $(\partial\sigma/\partial X_{H2})(\Delta X_{H2})$, and it is obtained to be 0.05%, where we take $\Delta X_{H2} = 1mm$ maximally. The pion absorption rate is confirmed

by a Monte Carlo simulation program called "FURUKA"[21]. The result is obtained assuming the same detector configuration with no multiple scattering effect, but without the cut for the edge of the counter in H2, and is shown in Figure 4.17(b). The result is consistent with the data.

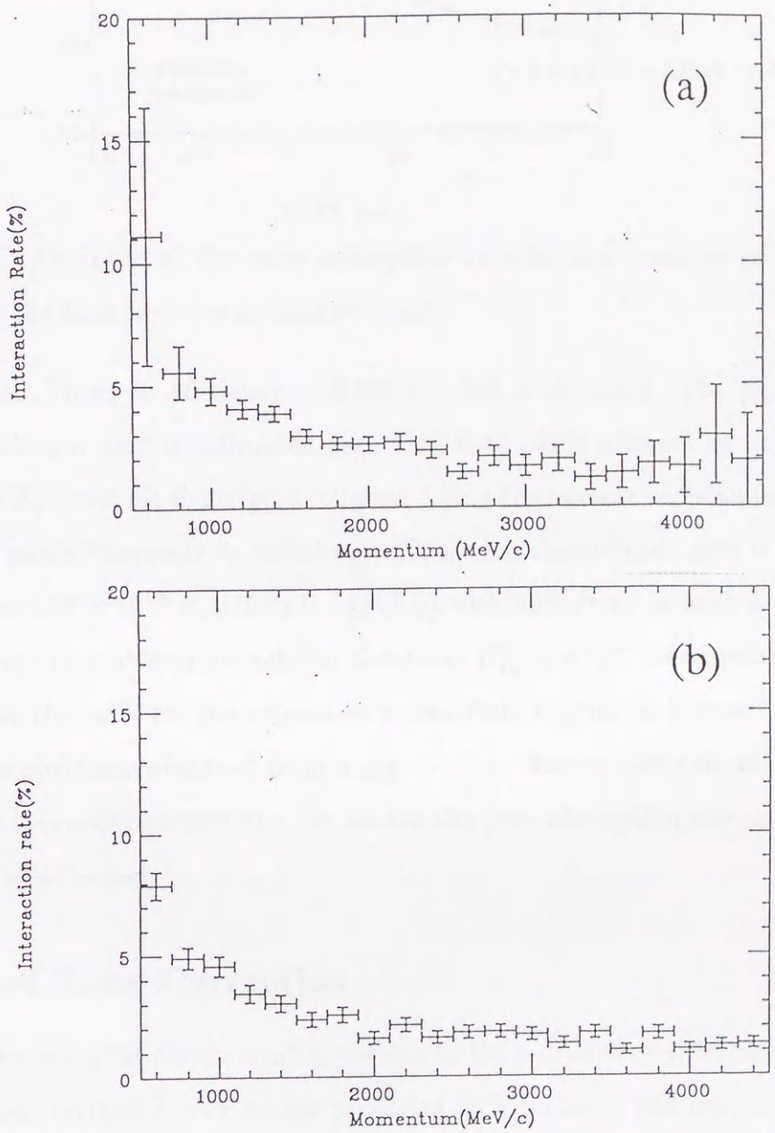

Figure 4.17: Pion absorption rate as a function of the momentum (a)for the real data and (b) for a Monte Carlo data on the basis of FURUKA.

There are two corrections in the pion absorption rate, one is the inefficiency of H2, and the other is the rate of interaction in the material upstream from H1. The inefficiency of H2 was measured during a special run which used the shower counter as the trigger counter. We use the same analysis procedure as for the determination of the

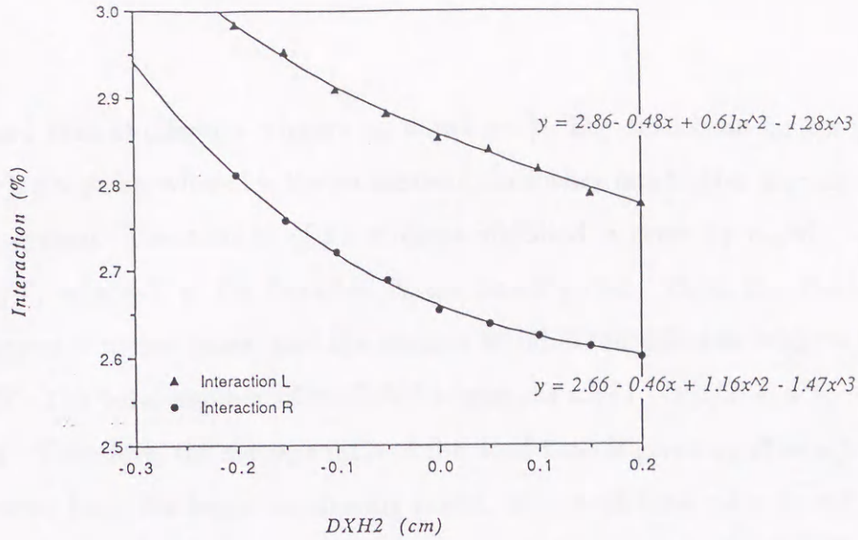

Figure 4.18: Dependence of the pion absorption rate on the position of H2 which is represented by the shift from its normal position.

pion absorption. Then, an efficiency of 0.995 ± 0.003 is obtained. The pion absorption rate in the upstream part is estimated assuming that pions interacting in the material upstream from H1 never hit the trigger counter. Using the nuclear collision length, namely assuming that pions disappear by colliding with nuclei, the collision rate is estimated to be $6.6 \times 10^{-3} = 4.56 \times 10^{-3} \times 1.45$(N.C.L/N.I.L) with 20% error in both arms.

The average pion absorption rate for the decay $K_L^0 \to \pi^+\pi^-$ is estimated to be $(6.3 \pm 0.6)\%$ averaging the rates for the respective momentum regions in Figure 4.17(a). Using the momentum spectrum obtained from a $K_L^0 \to \pi^+\pi^-$ Monte Carlo simulation. Finally, combining the two above corrections, we obtain the pion absorption rate of $(6.0 \pm 0.8)\%$ for the $K_L^0 \to \pi^+\pi^-$ decay.

4.4.2 Dead Time Correction

A trigger coming randomly is inhibited due to the online dead time for the preceding trigger. However, triggers for $\pi\pi$ events prescaled by a factor of 500 are not inhibited by the dead time because the prescaled trigger comes almost periodically, that is, the interval between two triggers is almost constant. But dilepton triggers may be inhibited due to the dead time. Therefore the difference of the effective dead times between the dilepton and $\pi\pi$ triggers should be corrected.

The correction factor is obtained as follows. Let n be the number of total triggers in a beam pulse and r be the fraction of $\pi\pi$ triggers. The number of $\pi\pi$ triggers, $n_{\pi\pi}$, is

$n_{\pi\pi} = nr$, and that of dilepton triggers $n_{ll} = n(1-r)$. The dead time for $\pi\pi$ triggers is $n_{ll} = n(1-r)t$ per pulse, where t is the online dead time when one trigger is accepted by the data-taking system. The number of $\pi\pi$ triggers inhibited is given by $n_{\pi\pi}n(1-r)t/T = n^2r(1-r)t/T$, where T is the duration of the beam pulse. Thus, the dead time for dilepton triggers is nt per pulse, and the number of inhibited dilepton triggers is $n_{ll}nt = n^2(1-r)t/T$. The total number of inhibited triggers is $n^2r(1-r)t/T + n^2(1-r)t/T = n^2(1-r)t/T$. Therefore, the average ratio of the dead time is given by $R = n(1-r^2)t/T$, and R is known from the beam monitoring scaler. The dead time ratio for $\pi\pi$ trigger is $n(1-r)t/T = R(1-r)/(1-r^2) = R/(1+r)$, and the ratio for dilepton triggers becomes $nt/T = R/(1-r^2)$. Then, a correction of the dead time difference between $\pi\pi$ and dilepton triggers is given by

$$C_{DT} = \frac{1 - R/(1+r)}{1 - R/(1-r^2)}.$$

A correction of C_{DT} has to be made in the calculation of the sensitivity. R and r are calculated for every run and are about 7% and about 20% as a whole. Then, the dead time difference between dilepton and $\pi\pi$ triggers is obtained to be $(1.3 \pm 0.3)\%$. [3]

4.5 Final Results

4.5.1 Sensitivities

Using the equation (4.1) and the values obtained in the previous four sections and $B(K_L^0 \to \pi^+\pi^-) = (2.03 \pm 0.04) \times 10^{-3}$, the single event sensitivities for the decays $K_L^0 \to \mu e$, $K_L^0 \to ee$ and $K_L^0 \to \mu\mu$ are calculated, and summarized in Table 4.5. All error terms and an uncertainty of 2% due to the error on the branching ratio of the decay $K_L^0 \to \pi^+\pi^-$ are added in quadrature, and the error in the sensitivity is determined to be 3% for each mode. The systematic error is very small because the sensitivity is determined by the ratio of two decay modes measured simultaneously using the same detector.

[3] There was no dead time difference during the last two cycles because the preset scalar was inhibited by the master trigger. Therefore, the correction factor is 1.0 for the two cycles.

	$K_L^0 \to \mu e$	$K_L^0 \to ee$	$K_L^0 \to \mu\mu$
$N_{\pi^+\pi^-}/\epsilon_{\pi^+\pi^-}(\times 10^7)$	6.80 (1.0%)	6.80 (1.0%)	6.80 (1.0%)
$A/A_{\pi\pi}$	0.939 (1.0%)	0.940 (1.0%)	0.839 (1.5%)
ϵ	0.744 (0.5%)	0.730 (0.5%)	0.763 (0.5%)
correction	0.952 (0.9%)	0.952 (0.9%)	0.952 (0.9%)
sensitivity ($\times 10^{-11}$)	4.07 (1.7%)	4.14 (1.7%)	4.44 (2.1%)

Table 4.5: Summary of the sensitivities, where systematic errors are given in parentheses

4.5.2 Results on the Decays $K_L^0 \to \mu e$ and $K_L^0 \to ee$

Figure 4.19 shows a scatter plot of the effective mass $M_{\mu e}$ vs. collinearity-squared θ^2 for μe events. No event is observed in the fiducial region represented by a rectangle. Since an observation of zero events corresponds to the presence of 2.3 events at the 90% confidence level assuming a Poisson distribution, the upper-limit of the $K_L^0 \to \mu e$ branching ratio at the 90% confidence level is determined to be,

$$B(K_L^0 \to \mu e) < 9.4 \times 10^{-11},$$

with a systematic error of 3%. There are a few events near to, but outside the fiducial region. According to a background study discussed in the next chapter, they are expected from the decay $K_L^0 \to \pi e \nu$ whose pion has decayed into a muon in the spectrometer, and we can safely say that the influence of the background in the fiducial region is small at this sensitivity level. Another possible background source is the double misidentification of $\pi \to e$ and $e \to \mu$ for the decay $K_L^0 \to \pi e \nu$, which turns out to be negligibly small.

On the other hand, there is one ee event in the fiducial region which is seen in a scatter plot for the ee events as shown in Figure 4.20. There are five background events below the K_L^0 mass. A background study for $K_L^0 \to ee$ in chapter 5 indicates that they mainly come from the decay $K_L^0 \to e^+e^-e^+e^-$. The one event in the fiducial region is at the tail end of the background distribution and cannot be distinguished from it at the sensitivity level of one event. Therefore, the upper-limit of the decay $K_L^0 \to ee$ branching ratio at the 90% confidence level which corresponds to the presence

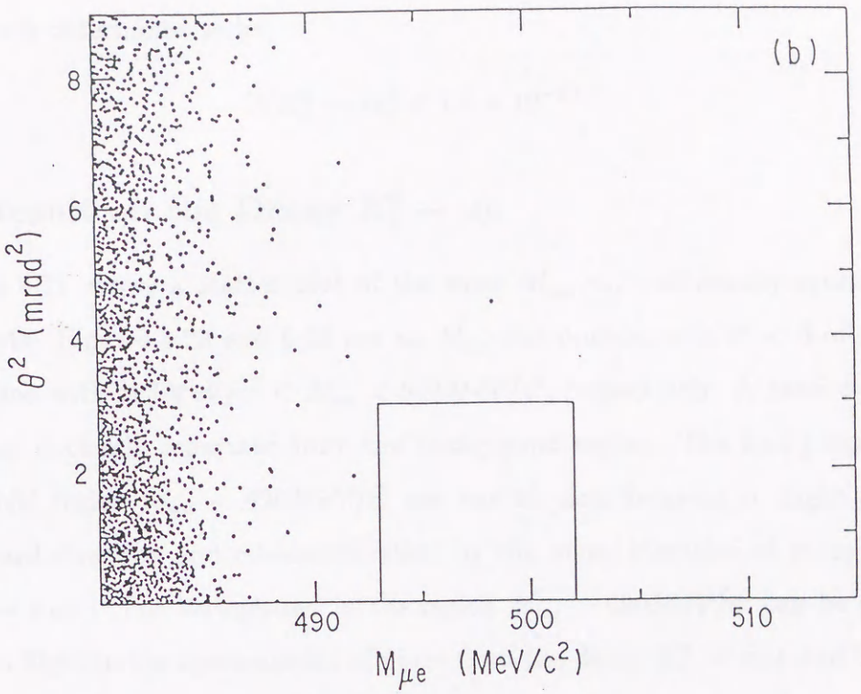

Figure 4.19: Scatter plot for μe events of the effective mass $M_{\mu e}$ vs. collinearity angle-squared θ^2.

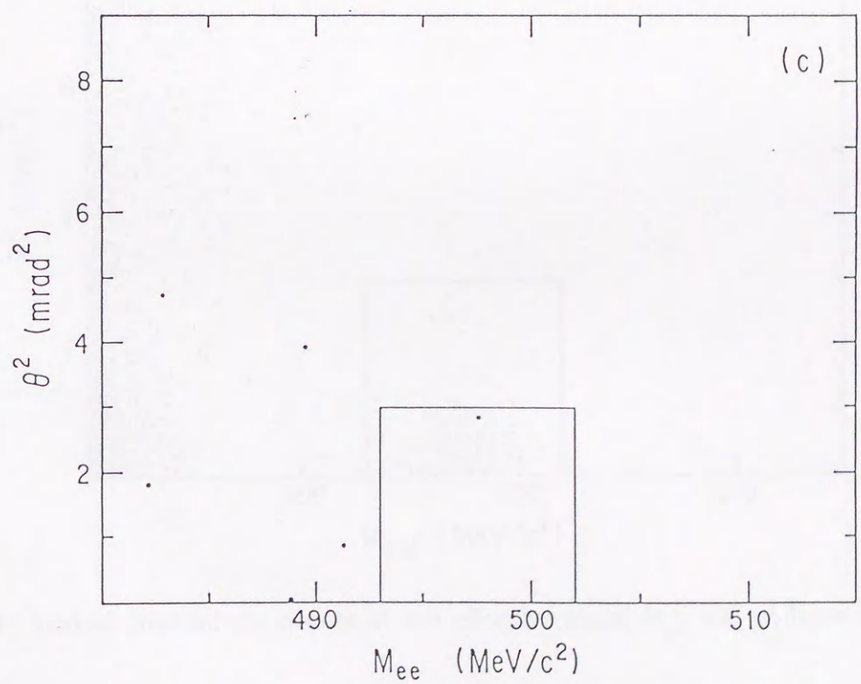

Figure 4.20: Scatter plot for ee events of the effective mass M_{ee} vs. collinearity angle-squared θ^2.

of 3.9 events is determined to be,

$$B(K_L^0 \to ee) < 1.6 \times 10^{-10}.$$

4.5.3 Result on the Decay $K_L^0 \to \mu\mu$

Figure 4.21 shows a scatter plot of the mass $M_{\mu\mu}$ vs. collinearity-squared θ^2 for the $\mu\mu$ events. Figures 4.22 and 4.23 are an $M_{\mu\mu}$-distribution with $\theta^2 < 3mrad^2$ and a θ^2-distribution with $493MeV/c^2 < M_{\mu\mu} < 502MeV/c^2$, respectively. A peak centered at the K_L^0 mass is clearly separated from the background region. The background events in the fiducial region $M_{\mu\mu} < 490MeV/c^2$ are due to pion decaying in flight to muons in the forward direction and misidentification by the muon identifier of pions from the decay $K_L^0 \to \pi\mu\nu$. The background in the region $M_{\mu\mu} > 490MeV/c^2$ can be explained by decays in flight in the spectrometer of pions from the decay $K_L^0 \to \pi\mu\nu$ and by double misidentification as muons of both pions and electrons from the decay $K_L^0 \to \pi e\nu$.

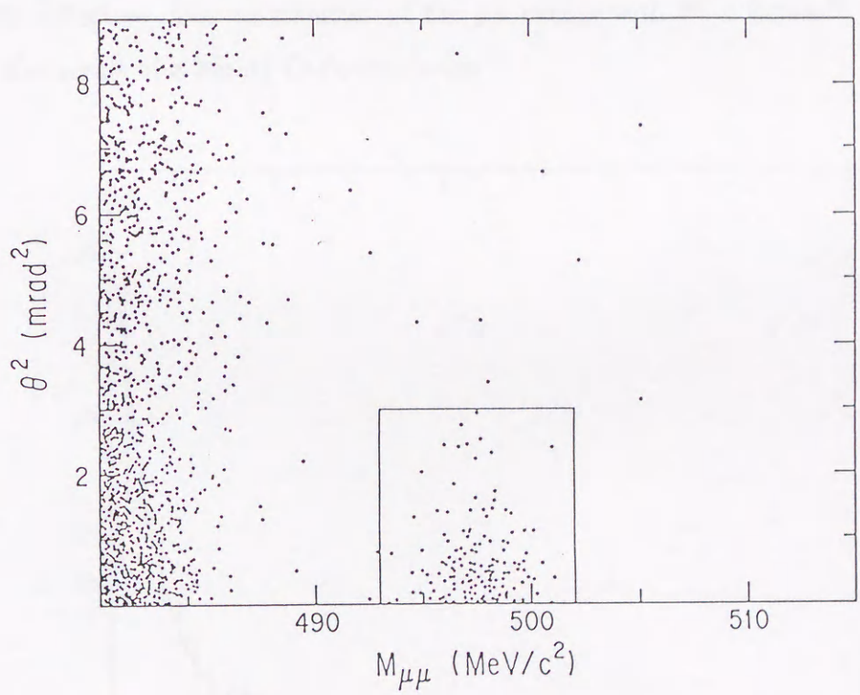

Figure 4.21: Scatter plot for $\mu\mu$ events of the effective mass $M_{\mu\mu}$ vs. collinearity angle-squared θ^2.

The number of $\mu\mu$ events in the fiducial region is 179. The number of $\mu\mu$ events in the region $493MeV/c^2 < M_{\mu\mu} < 502MeV/c^2$ and $3mrad^2 < \theta^2 < 9mrad^2$ is 5 and

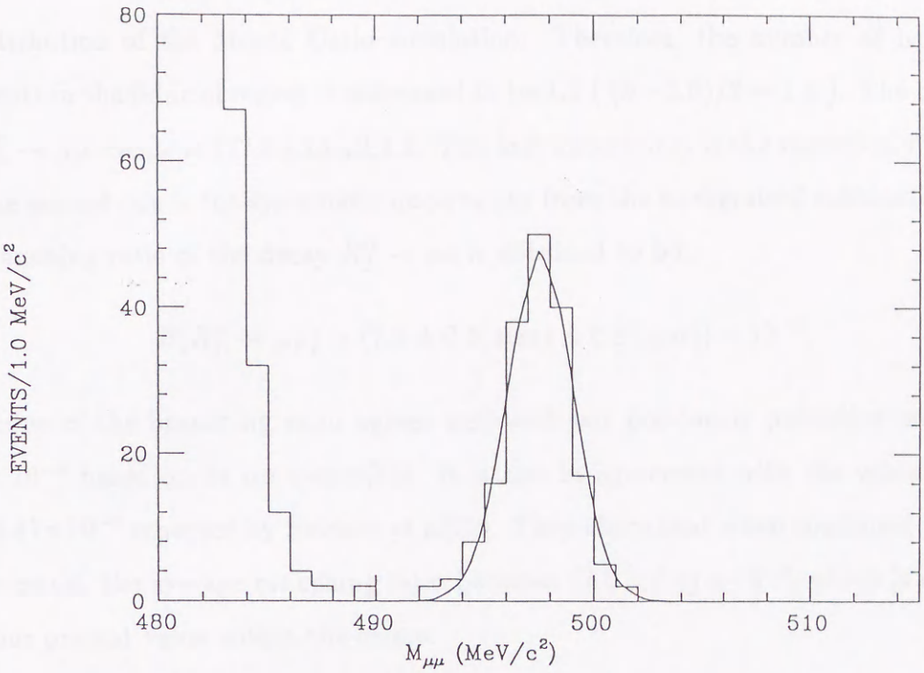

Figure 4.22: Effective mass distribution of the $\mu\mu$ events with $\theta^2 < 3mrad^2$. Solid line represents the result of a Monte Carlosimulation.

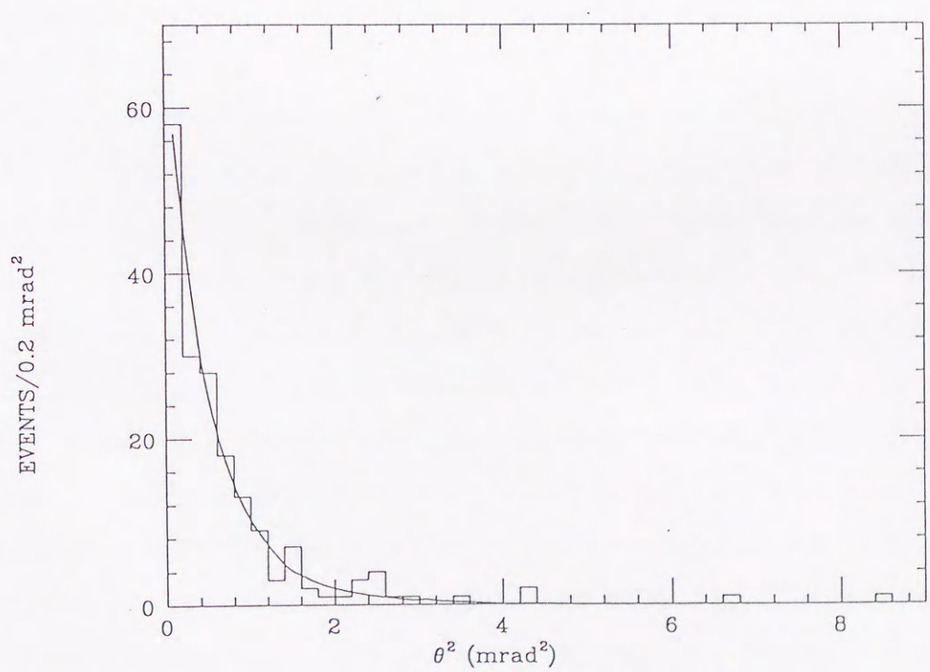

Figure 4.23: θ^2 distribution of the $\mu\mu$ events with $493MeV/c^2 < M_{\mu^+\mu^-} < 502MeV/c^2$. Solid line represents the result of a Monte Carlo simulation.

the number of real $K_L^0 \to \mu\mu$ events in the same region is expected to be 2.6 from the θ^2 distribution of the Monte Carlo simulation. Therefore, the number of background $\mu\mu$ events in the fiducial region is estimated to be 1.2 ($(5-2.6)/2 = 1.2$). The number of the $K_L^0 \to \mu\mu$ events is $177.8 \pm 13.4 \pm 1.2$. The first uncertainty is the statistical fluctuation and the second one is the systematic uncertainty from the background subtraction. Then the branching ratio of the decay $K_L^0 \to \mu\mu$ is obtained to be,

$$B(K_L^0 \to \mu\mu) = (7.9 \pm 0.6(stat) \pm 0.3(syst)) \times 10^{-9}.$$

Our value of the branching ratio agrees well with our previously published one: $(8.4 \pm 1.1) \times 10^{-9}$ based on 54 $\mu\mu$ events[15]. It is also in agreement with the value of $(7.6 \pm 0.5 \pm 0.4) \times 10^{-9}$ reported by Heinson et al[22]. They claim that when combined with their earlier result, the average branching ratio becomes $(7.0 \pm 0.5) \times 10^{-9}$, which is consistent with our present value within the errors.

Chapter 5

Background Study to $K_L^0 \to \mu e$ and $K_L^0 \to ee$

5.1 Background Study to $K_L^0 \to \mu e$

As described in the previous section 4.5, there are a few background events near to, but outside the fiducial region. In order to gain insight into the origin of this small residual background and its possible influence on the fiducial region, further investigations were made. This leads to increase confidence in the results.

To make clear the nature of the background events, a scatter plot of the effective mass $M_{\mu e}$ vs. P_t for μe events is made and is shown in Figure 5.1, where P_t is the transverse momentum of the μe system with respect to the target-to-vertex direction. Many events are seen clustering in the region of effective mass below $490 MeV/c^2$, where the events with low P_t come from $K_L^0 \to \pi e \nu$ decay with the pion misidentified as a muon, and the high P_t events come from the $K_L^0 \to \pi e \nu$ decay with the pion decaying to a muon in the decay chamber. There are some events with effective masses above $490 MeV/c^2$. They cannot be reproduced by the above two background sources according to the discussion in section 2.1. Most of the events with $M_{\mu e} > 490 MeV/c^2$ fall on the high P_t side of the line drawn in Figure 5.1. The line connects the two points $(M_{\mu e}, P_t) = (489.24 MeV/c^2, 8.36 MeV/c)$ and $(480.36 MeV/c^2, 0.00 MeV/c^2)$. Both points are obtained for the decay $K_L^0 \to \pi e \nu$ with the pion decaying to a muon having the same direction as the pion. One point is for the case that the electron neutrino is emitted with zero momentum (see Figure 5.2(a)), and the

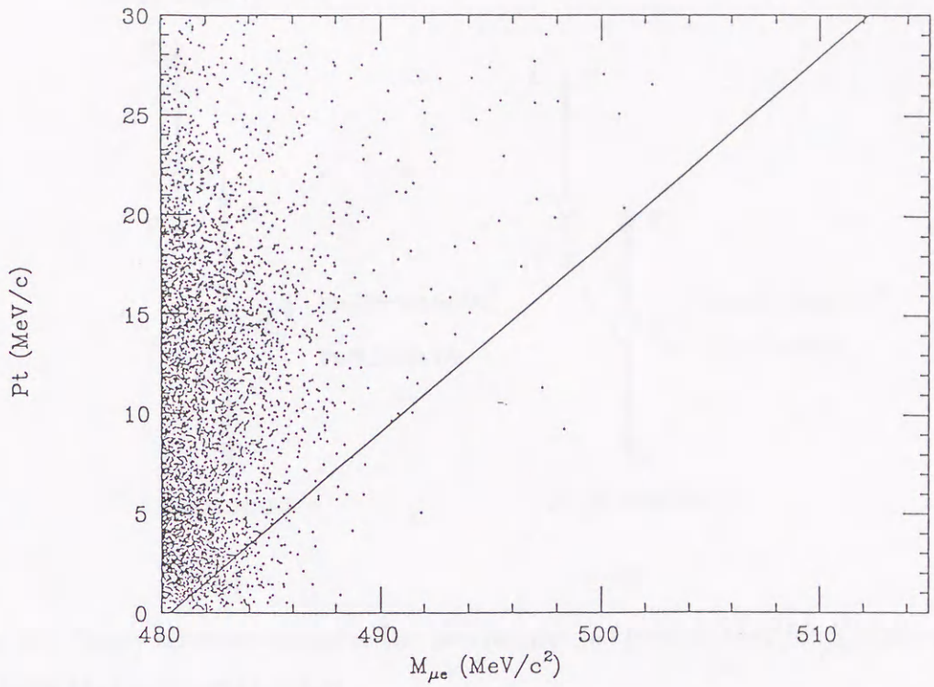

Figure 5.1: Scatter plot of M_{ee} vs. P_t for μe events. The straight line connects the two points $(M_{\mu e}, P_t) = (489.24 MeV/c^2, 8.36 MeV/c)$ and $(480.36 MeV/c^2, 0.00 MeV/c^2)$.

other is for the case that the electron neutrino from the K_L^0 decay and the muon neutrino from the subsequent pion decay compensate for the missing P_t (see Figure 5.2(b)). Most of the events with $M_{\mu e} > 490 MeV/c^2$ seem to die out before reaching the line. This suggests that they come from the $K_L^0 \rightarrow \pi e \nu$ decay with the pion decaying to a muon. However, several events are also present below the line. Therefore, of the two additional possible background sources, $\pi \rightarrow e$ and $e \rightarrow \mu$ double misidentification for the decay $K_L^0 \rightarrow \pi e \nu$, and the decay $K_L^0 \rightarrow \pi e \nu$ with the pion decaying to $\mu \nu$ in the *spectrometer*, the former one would be more serious. Based on the above discussion, the four background sources are considered below in turn.

First, the background events of $M_{\mu e} < 490 MeV/c^2$ are considered. Figure 5.3 shows a scatter plot of $M_{\mu e}$ vs P_t for Monte Carlo events based on the two background sources: $K_L^0 \rightarrow \pi e \nu$ decay with the pion misidentified as a muon and $K_L^0 \rightarrow \pi e \nu$ decay with the pion decaying to a muon in the decay chamber. They are normalized to the sensitivity of this experiment. The normalization factor for the decay $K_L^0 \rightarrow \pi e \nu$ with the pion decaying to a muon can be calculated using the values given in the previous section. For

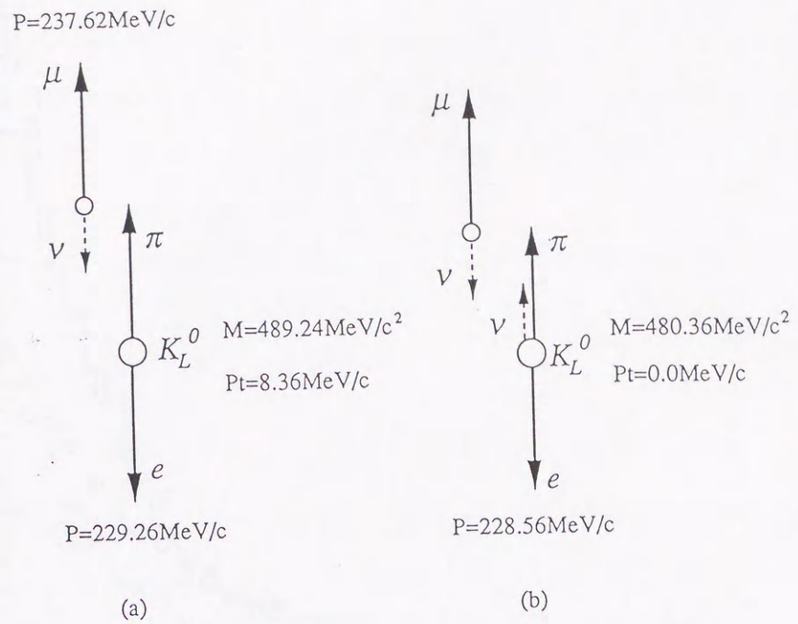

Figure 5.2: Decay schemes to derive the two points: (a) $(489.24 MeV/c^2, 8.36 MeV/c)$ and (b) $(480.36 MeV/c^2, 0.00 MeV/c^2)$.

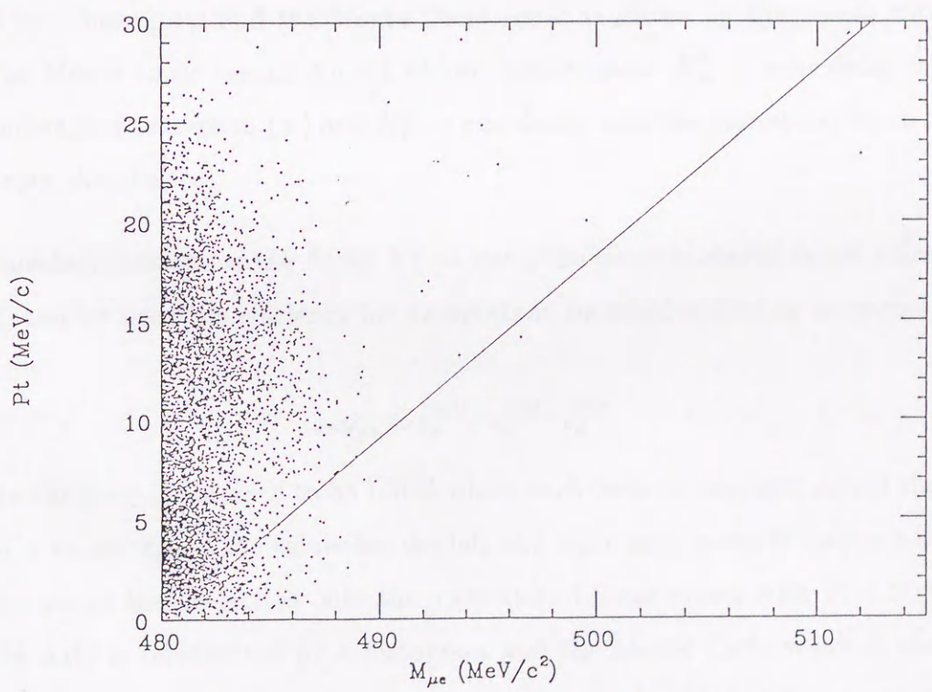

Figure 5.3: Scatter plot of $M_{\mu e}$ vs P_t for Monte Carlo events based on the two background sources: $K_L^0 \to \pi e \nu$ decay with the pion misidentified as a muon and $K_L^0 \to \pi e \nu$ decay with the pion decaying to a muon in the decay chamber.

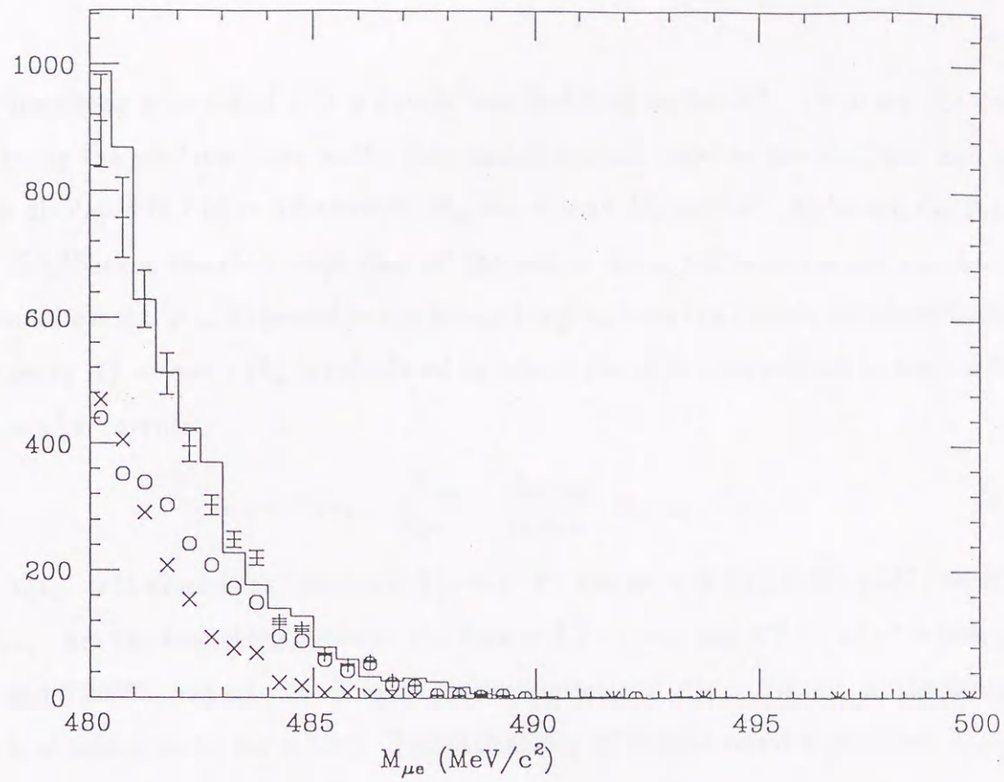

Figure 5.4: Mass distribution of μe events with $P_t < 20 MeV/c$, where the data is represented by a histogram and the Monte Carlo result is shown by the points with error bars. The Monte Carlo results consist of two components: $K_L^0 \rightarrow \pi e \nu$ decay with the pion misidentified as a muon ($\times$) and $K_L^0 \rightarrow \pi e \nu$ decay with the pion decaying to a muon in the decay chamber (o).

$\pi \rightarrow \mu$ misidentification for the decay $K_L^0 \rightarrow \pi e \nu$, the particle-identification efficiency is different, and we need the efficiency for πe events to be misidentified as μe events, which is given by,

$$\epsilon_{\pi e \rightarrow \mu e} = \epsilon_{\pi}^{MU} \cdot \epsilon_{e}^{EM} \cdot \epsilon_{e}^{CV}. \tag{5.1}$$

The efficiency is obtained to be 1.56% where each term on the right side of the above equation is an average of the values for the left and right arms given in Tables 4.2 to 4.4. Figure 5.4 shows the projection onto the mass axis of those events with $P_t < 20 MeV/c$, where the data is represented by a histogram and the Monte Carlo result is shown by the points with error bars. Each of the two components, the decay $K_L^0 \rightarrow \pi e \nu$ with pion misidentification and with the pion decay, is also shown in Figure 5.4. The shape of the event distribution is reproduced well.

Next, the background events with $M_{\mu e} > 490 MeV/c^2$ are considered. Monte Carlo

events describing $\pi \rightarrow e$ and $e \rightarrow \mu$ double misidentification for $K_L^0 \rightarrow \pi e \nu$ are obtained by assigning the electron mass to the pion and the muon mass to the electron, and the result is displayed in Figure 5.5 showing $M_{\mu e}$ vs. P_t and $M_{\mu e}$ and θ^2. Although the shape of the distribution disagrees with that of the actual data, we estimate the number of background events, $N_{\mu e}$, expected in the fiducial region from the double misidentification for the decay $K_L^0 \rightarrow \pi e \nu$. $N_{\mu e}$ is calculated by taking the ratio with respect to the number of $K_L^0 \rightarrow \pi^+ \pi^-$ events:

$$N_{\mu e} = N_{\pi^+\pi^-} \cdot \frac{B_{\pi e \nu}}{B_{\pi^+\pi^-}} \cdot \frac{A_{e\pi \rightarrow \mu e}}{A_{\pi^+\pi^-}} \cdot \epsilon_{e\pi \rightarrow \mu e} \cdot C, \tag{5.2}$$

where $N_{\pi^+\pi^-}$ is the number of detected $K_L^0 \rightarrow \pi^+ \pi^-$ events $-$ $(6.80 \pm 0.07) \times 10^7$ and $B_{\pi e \nu}$ and $B_{\pi^+\pi^-}$ are the branching ratios of the decays $K_L^0 \rightarrow \pi e \nu$ and $K_L^0 \rightarrow \pi^+ \pi^-$ which are 38.7% and 0.203%, respectively. The relative acceptance of $A_{e\pi \rightarrow \mu e}/A_{\pi^+\pi^-}$ in the fiducial region is obtained to be 9.1×10^{-6}. The probability of double misidentification, $\epsilon_{e\pi \rightarrow \mu e}$, is given by the following equation:

$$\epsilon_{e\pi \rightarrow \mu e} = (\epsilon_e^{MU} \epsilon_{\bar{e}}) \cdot (\epsilon_\pi^{EM} \epsilon_\pi^{CV}), \tag{5.3}$$

where the veto efficiency of electrons $\epsilon_{\bar{e}}$ is given by,

$$\epsilon_{\bar{e}} = (1 - \epsilon_e^{EM_{veto}})(1 - \epsilon_e^{CV}). \tag{5.4}$$

The definitions and the values of the terms on the right-hand side are given in Tables 4.2 to 4.4, and each term should be averaged over the left and right arms. We obtain the probability $\epsilon_{e\pi \rightarrow \mu e} = 4.2 \times 10^{-5}$. A correction term $C = 1.028$ consists of a dead time correction of 1.3%, a pion absorption rate for $K_L^0 \rightarrow \pi e \nu$ of 2.4% and that for $K_L^0 \rightarrow \pi^+ \pi^-$ of 6.0%. Then, $N_{\mu e}$ is calculated to be 5.2×10^{-5} which is negligibly small. Double misidentification for $K_L^0 \rightarrow \pi e \nu$ cannot explain the actual background events with high mass.

Figure 5.6 shows scatter plots of $M_{\mu e}$ vs. P_t and θ^2 for Monte Carlo events of $K_L^0 \rightarrow \pi e \nu$ with the pion decaying to a muon in the spectrometer. The shape of the events with $M_{\mu e} > 490 MeV/c^2$ is reproduced well by the Monte Carlo simulation. Therefore, the actual data can be satisfactorily explained by this background source. Since there is no Monte Carlo event in the fiducial region, here we calculate the number of expected events in the region supposing that N_d events were produced by the Monte Carlo simulation.

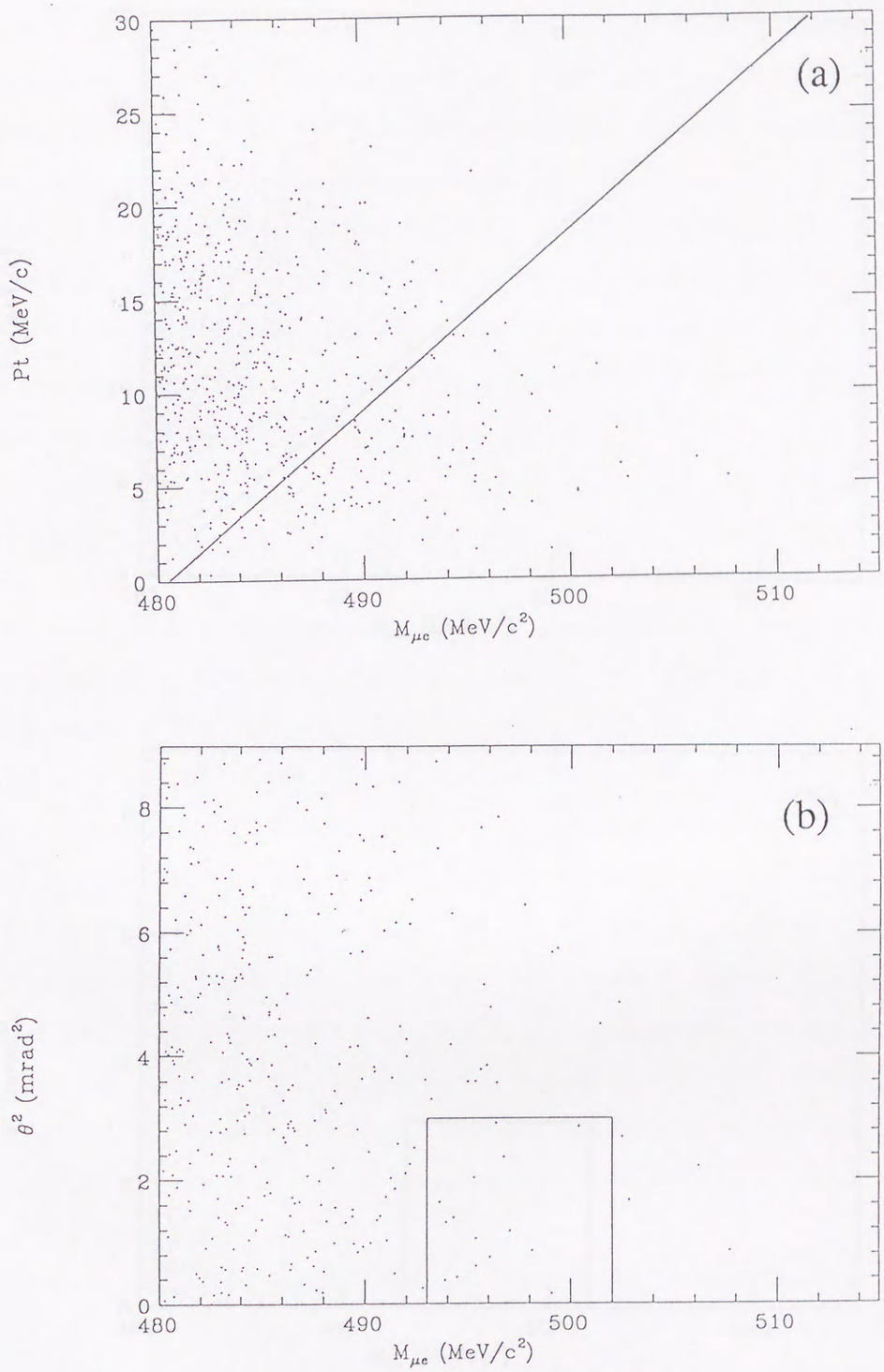

Figure 5.5: Scatter plot of $M_{\mu e}$ vs. (a)P_t and (b) θ^2 for Monte Carlo events on the basis of $\pi \to e$ and $e \to \mu$ double misidentification for $K_L^0 \to \pi e \nu$. It corresponds to 3.3×10^5 times our sensitivity.

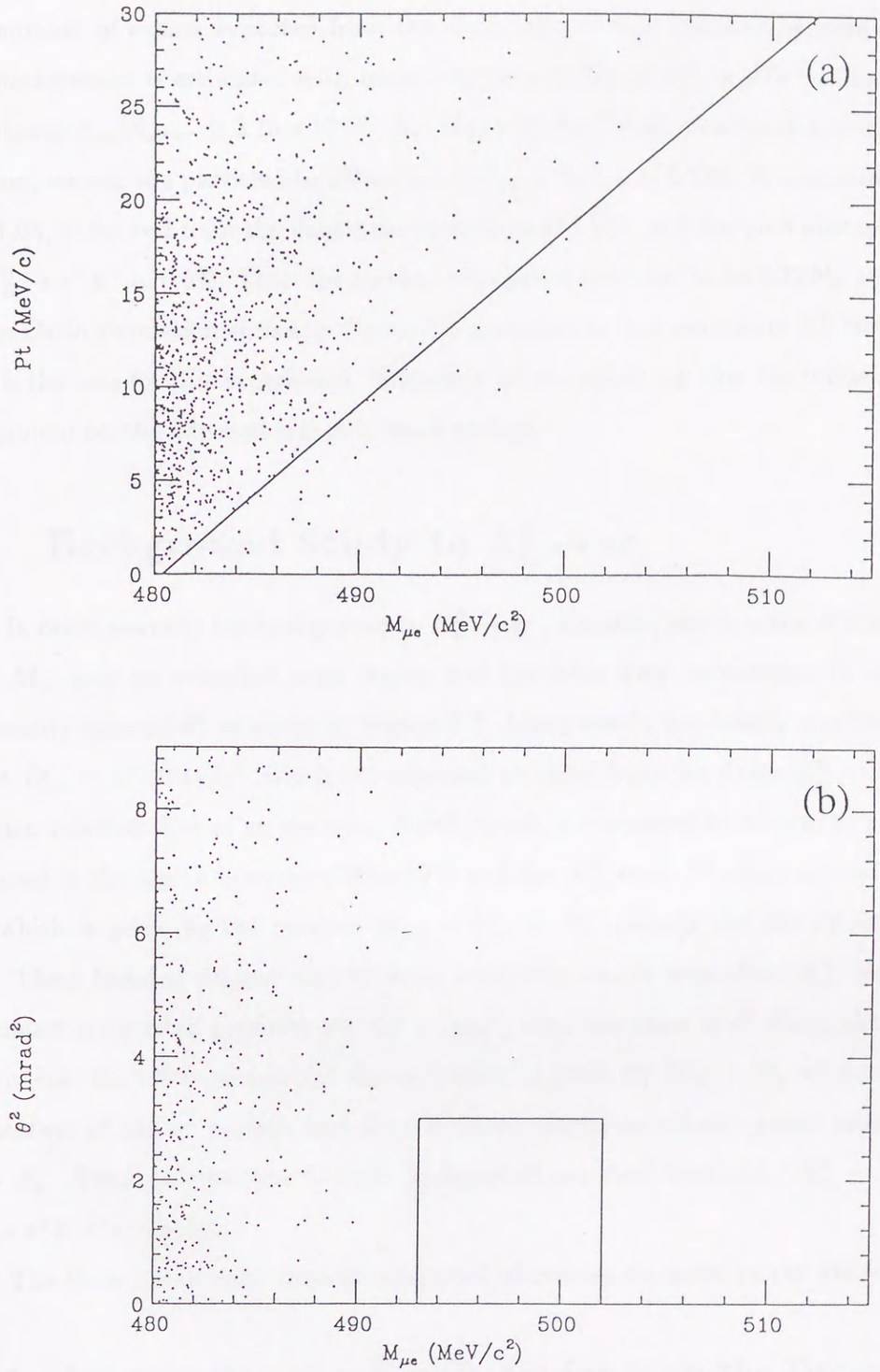

Figure 5.6: Scatter plots of $M_{\mu e}$ vs. (a) P_t and (b) θ^2 for Monte Carlo events of $K_L^0 \to \pi e \nu$ with the pion decaying to a muon in the spectrometer.

The number of events expected from the decay $K_L^0 \to \pi e\nu$ followed by pion decay in the spectrometer is estimated with respect to the number of $K_L^0 \to \pi^+\pi^-$. The relative acceptance $A_{\mu e}/A_{\pi^+\pi^-}$ is $3.13 \times 10^{-11} \cdot N_d$. Since the final state consists of a muon and an electron, we use the particle-identification efficiency for μe of 0.744. A correction factor, $C = 1.05$, is derived from the dead time correction of 1.3%, and the pion absorption rate for $K_L^0 \to \pi^+\pi^-$ of 6.0%. Then the number of events is expected to be $0.32N_d$, and so, the Monte Carlo simulation shown in Figure 5.6 corresponds to a sensitivity 3.2 times larger than is the case for this experiment. Therefore we can safely say that the influence of the background on the fiducical region is small enough.

5.2 Background Study to $K_L^0 \to ee$

In order to study the background to $K_L^0 \to ee$, a scatter plot is made of the effective mass M_{ee} over an extended mass region and the transverse momentum P_t instead of collinearity squared θ^2 as shown in Figure 5.7. Many events are thickly clustered in the region $M_{ee} < 470 MeV/c^2$, which are expected to come from the decay $K_L^0 \to \pi e\nu$ with the pion misidentified as an electron. Furthermore, a considerable number of events are scattered in the region between $470 MeV/c^2$ and the K_L^0 mass. The line shown in Figure 5.7, which is given by the relation $M_{K_L^0} - M_{ee} = P_t$, delimits the distribution rather well. These features suggest that these ee candidate events come from K_L^0 decays with associated undetected particles x^0, $K_L^0 \to eex^0$, with the mass of x^0 being almost zero. In this case the effective mass of the ee system is given by $M_{K_L^0} - P_x$ where P_x is the momentum of the x^0 particle and then these ee candidate events cannot have missing $P_t > P_x$. Two contributions to such background are considered, i.e. $K_L^0 \to ee\gamma$ and $K_L^0 \to e^+e^-e^+e^-$ decays.

The three background sources mentioned above are discussed in the following.

5.2.1 Investigation of ee Events Arising from the Decay $K_L^0 \to \pi e\nu$

Most of the events with effective mass less than $470 MeV/c^2$ come from the decay $K_L^0 \to \pi e\nu$ with the pion misidentified as an electron. That can be reproduced well by

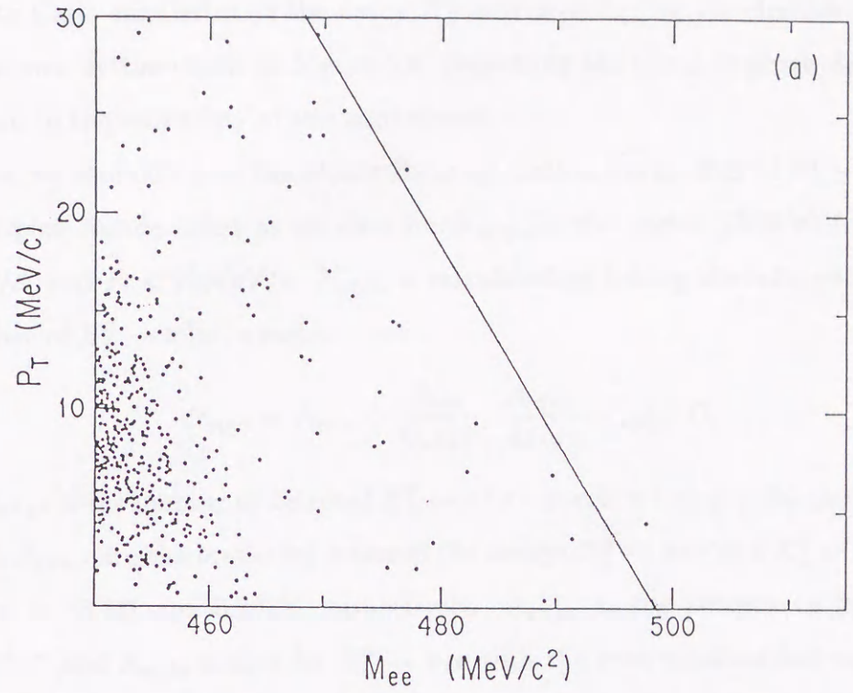

Figure 5.7: Scatter plot of M_{ee} vs. P_t for ee events.

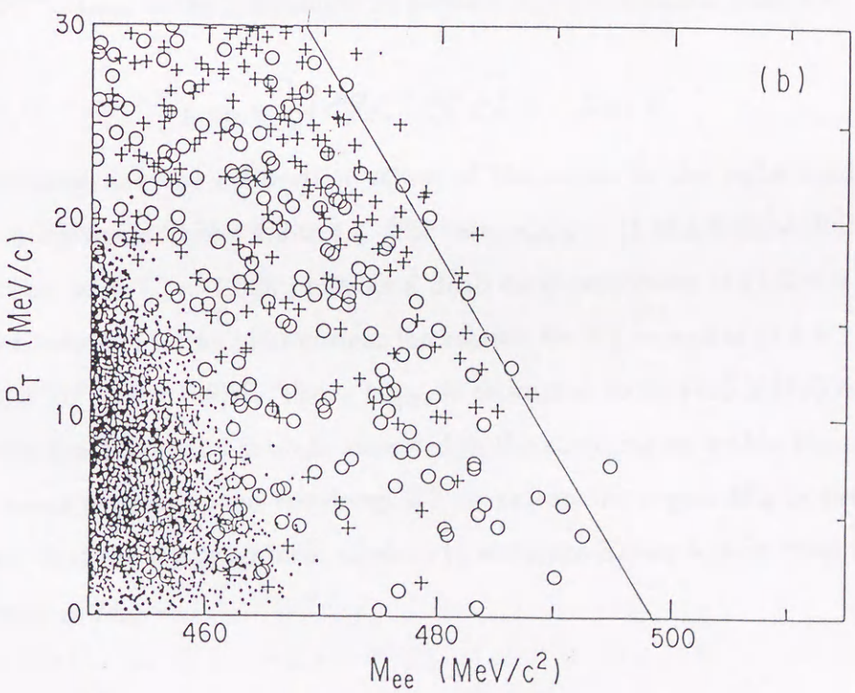

Figure 5.8: Scatter plot of M_{ee} vs. P_t for ee Monte Carlo events: contribution from decays $K_L^0 \to \pi e\nu$ $(\cdot)$, $K_L^0 \to ee\gamma$ $(+)$ and $K_L^0 \to e^+e^-e^+e^-$ $(\circ)$.

the Monte Carlo simulation of the decay $K_L^0 \to \pi e\nu$ assigning the electron mass to the pion as shown by the points in Figure 5.8, generating ten times as much data as would correspond to the sensitivity of this experiment.

Now, we estimate from the Monte Carlo simulation the number of $K_L^0 \to \pi e\nu$ events with the pion misidentified as an electron $N_{\pi(e)e}$ in the region $450MeV/c^2 < M_{ee} < 470MeV/c^2$ and $P_t < 20MeV/c$. $N_{\pi(e)e}$ is calculated by taking the ratio with respect to the number of $K_L^0 \to \pi^+\pi^-$ events:

$$N_{\pi(e)e} = N_{\pi^+\pi^-} \cdot \frac{B_{\pi e\nu}}{B_{\pi^+\pi^-}} \cdot \frac{A_{\pi(e)e}}{A_{\pi^+\pi^-}} \cdot \epsilon_{\pi(e)e} \cdot C, \tag{5.5}$$

where $N_{\pi^+\pi^-}$ is the number of detected $K_L^0 \to \pi^+\pi^-$ events which is $(6.80 \pm 0.07) \times 10^7$ and $B_{\pi e\nu}$ and $B_{\pi^+\pi^-}$ are the branching ratios of the decays $K_L^0 \to \pi e\nu$ and $K_L^0 \to \pi^+\pi^-$ which are given as 38.7% and 0.203%, respectively. $A_{\pi^+\pi^-}$ is the acceptance for the decay $K_L^0 \to \pi^+\pi^-$ and $A_{\pi(e)e}$ is that for $K_L^0 \to \pi e\nu$ with the pion misidentified as an electron and for which M_{ee} and P_t, fall into the region $450MeV/c^2 < M_{ee} < 470MeV/c^2$ and $P_t < 20MeV/c$. The relative acceptances are expressed as a ratio $A_{\pi(e)e}/A_{\pi^+\pi^-} = (2.69 \pm 0.04) \times 10^{-4}$. $\epsilon_{\pi(e)e}$ is the probability of particle misidentification from $\pi e\nu$ to ee and is given by:

$$\epsilon_{\pi(e)e} = \frac{1}{2}\left(\epsilon_{\pi L}^{EM}\epsilon_{\pi L}^{CV}\epsilon_{eR}^{EM}\epsilon_{eR}^{CV} + \quad L \leftrightarrow R \quad\right). \tag{5.6}$$

The definitions and the calibration values of the terms in the right-hand side of the equation are given in Tables 4.2 to 4.4. The value $\epsilon_{\pi(e)e} = (1.31 \pm 0.48) \times 10^{-4}$ is obtained. A correction term $C = 1.028$ includes a dead time correction of $(1.3 \pm 0.3)\%$, a pion absorption rate due to the pion-nuclear interaction for $K_L^0 \to \pi e\nu$ of $(2.4 \pm 1.9)\%$ and for $K_L^0 \to \pi^+\pi^-$ of $(6.0 \pm 0.6)\%$. Then, $N_{\pi(e)e}$ is estimated to be (470 ± 174) events, and it agrees with the 430 events actually detected in the same region within the errors. There is no ee event expected from the decay $K_L^0 \to \pi e\nu$ in the region $M_{ee} > 470MeV/c$ due to the fact that the misassignment of pions to electrons having lighter mass brings about the decrease of M_{ee}.

5.2.2 Estimating the Number of $K_L^0 \to ee\gamma$ Events

As shown above, the distribution as well as the absolute normalization of the ee candidate events in the region $M_{ee} < 470MeV/c^2$ is well reproduced by $\pi \to e$ misiden-

tification in the $K_L^0 \to \pi e \nu$ decay, however, the ee events with $M_{ee} > 470 MeV/c^2$ cannot be explained. Let us consider the contribution of the decay $K_L^0 \to ee\gamma$ to the regions $M_{ee} > 470 MeV/c^2$ and $M_{ee} > 480 MeV/c^2$. The decay $K_L^0 \to ee\gamma$ has the branching ratio $(9.1 \pm 0.5) \times 10^{-6}$ which is obtained averaging the results of NA31 and E845[23]. The number of ee candidate events expected from the decay $K_L^0 \to ee\gamma$ is estimated by taking also the ratio to the number of $K_L^0 \to \pi^+\pi^-$ events. For this estimation, Monte Carlo simulation is done using the following equation:

$$\begin{aligned} \Gamma_{\gamma\gamma}^{-1} \frac{d\Gamma}{dx} &= \left(\frac{4\alpha}{3\pi}\right) \frac{(1-x^2)^3}{x} \\ &\times \left(1 - \frac{4m_e^2}{x^2 M_K^2}\right)^{1/2} \left(1 + \frac{2m_e^2}{x^2 M_K^2}\right)^{1/2} |f(x)|^2, \end{aligned} \tag{5.7}$$

where $x = M_{ee}/M_K$. The form factor[24] can be written as

$$\begin{aligned} f(x) &= \frac{1}{1 - 0.418x^2} + \frac{C\alpha_{K^*}}{1 - 0.311x^2} \\ &\times \left[\frac{4}{3} - \frac{1}{1 - 0.418x^2} - \frac{1}{9(1 - 0.405x^2)} - \frac{2}{9(1 - 0.238x^2)}\right], \end{aligned} \tag{5.8}$$

in which the value $\alpha_{K^*} = -0.28$ is determined by two experiments. The results of the Monte Carlo simulation is shown in Figure 5.8 with the crosses. The relative acceptance $A_{ee\gamma}/A_{\pi^+\pi^-}$ is $(1.85 \pm 0.33) \times 10^{-5}$ in the region $M_{ee} > 470 MeV/c^2$ and $(3.50 \pm 0.70) \times 10^{-6}$ for $M_{ee} > 480 MeV/c^2$. The particle identification efficiency is obtained to be 0.722 ± 0.004 averaging over the momentum spectra of electrons from the decay $K_L^0 \to ee\gamma$. With the above values and the correction factor $C = 1.053$ including a dead time correction and a pion absorption rate for $K_L^0 \to \pi^+\pi^-$, the number of events expected from the decay $K_L^0 \to ee\gamma$ in the region $M_{ee} > 470 MeV/c$ is 4.3 ± 0.8 and that for $M_{ee} > 480 MeV/c^2$ is 0.8 ± 0.2, while there are 18 and 6 events in the actual data in the respective regions. The actual data events cannot be satisfactorily explained by the decay $K_L^0 \to ee\gamma$.

5.2.3 Estimating the Number of $K_L^0 \to e^+e^-e^+e^-$ Events and the Branching Ratio

In order to explain the excess of data in the region $M_{ee} > 470 MeV/c^2$, we consider the contribution from the decay $K_L^0 \to e^+e^-e^+e^-$. The decay $K_L^0 \to e^+e^-e^+e^-$ is theoret-

ically predicted using the Kroll-Wada formula[25] for double internal conversion through the intermediate state of $\gamma^*\gamma^*$ and a similar calculation for the decay $\pi^0 \to e^+e^-e^+e^-$ is confirmed by experiment[26]. According to their work, the $K_L^0 \to e^+e^-e^+e^-$ decay rate is written as

$$\Gamma_{total} = \Gamma_1 + \Gamma_2 + \Gamma_{12}, \tag{5.9}$$

and Γ_1 is given by

$$2\Gamma_{\gamma\gamma}^{-1}\frac{d^2\Gamma_1}{dx_1dx_2} = \left(\frac{2\alpha}{3\pi}\right)^2 \frac{(1-(x_1+x_2)^2)^{3/2}(1-(x_1-x_2)^2)^{3/2}}{x_1x_2} \times\left[\left(1-\frac{4m_e^2}{x_1^2M_K^2}\right)^{1/2}\left(1+\frac{2m_e^2}{x_1^2M_K^2}\right)^{1/2}\right]\quad\left[\quad x_1 \leftrightarrow x_2\quad\right], \tag{5.10}$$

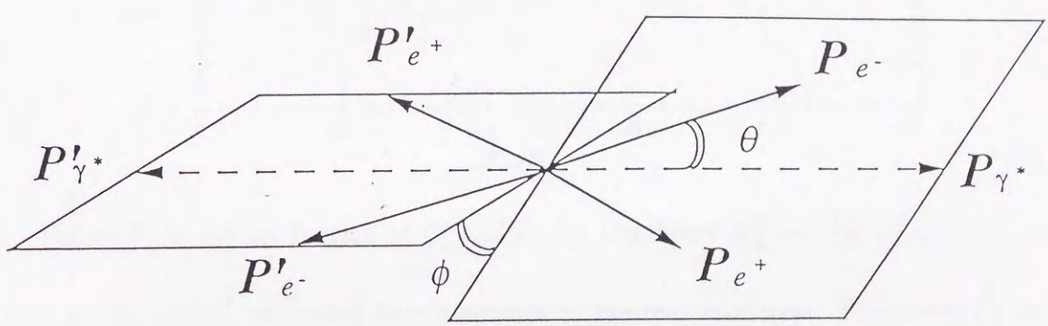

Figure 5.9: Decay scheme in the decay $K_L^0 \to e^+e^-e^+e^-$.

where $\Gamma_{\gamma\gamma}$ is the width of the decay $K_L^0 \to \gamma\gamma$, α is the fine structure constant and x_1 and x_2 are the effective masses of an e^+e^- pair divided by the K_L^0 mass and that of the other pair, respectively. The energy sharing between the e^+ and e^- in a pair and the correlation between the two planes made by two e^+e^- pairs follows the probability distribution:

$$\begin{aligned} g(x_1,x_2,y_1,y_2,\phi) &= \left[1+(y_1^2+\frac{4m_e^2}{x_1^2})(y_2^2+\frac{4m_e^2}{x_2^2})\right]\sin^2\phi \\ &+ \left[(y_1^2+\frac{4m_e^2}{x_1^2})+(y_2^2+\frac{4m_e^2}{x_2^2})\right]\cos^2\phi. \end{aligned} \tag{5.11}$$

y is given by $y = \sqrt{1 - 4m_e^2/x^2}\cos\theta$ where θ is the angle between the momentum direction of a virtual gamma and that of an electron, and ϕ is the angle between two e^+e^- pairs (see Figure 5.9). Γ_2 is defined as:

$$\Gamma_2(p_+, p_-, p'_+, p'_-) = \Gamma_1(p_+, p'_-, p'_+, p_-), \tag{5.12}$$

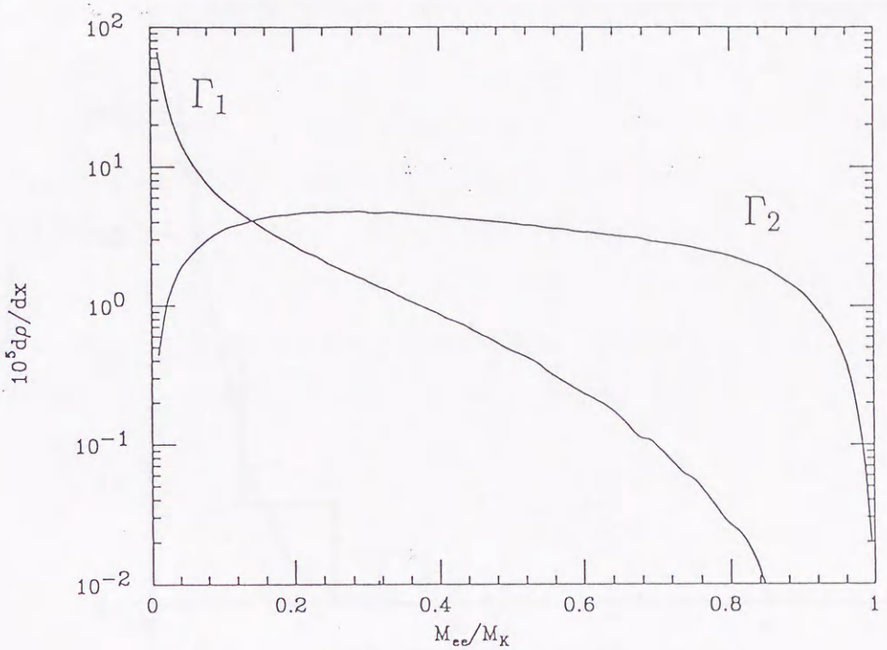

Figure 5.10: Decay spectra of Γ_1 and Γ_2 for the decay $K_L^0 \to e^+e^-e^+e^-$.

where p_+, p_-, p'_+ and p'_- represent four momenta of the four electrons. Therefore, Γ_2 can be obtained by exchanging the combinations of electron-positron pairs in Γ_1. The cross term Γ_{12} is negligibly small. We generate the $K_L^0 \to e^+e^-e^+e^-$ events using only Γ_1 with a Monte Carlo simulation. The contribution from Γ_2 is automatically taken into account by including all e^+e^- combinations in the acceptance calculation, and the result is shown in Figure 5.8 with the open circles. The decay spectra given in Ref.[25] are reproduced well using the generated events as shown in Figure 5.10. The acceptance ratio $A_{eeee}/A_{\pi^+\pi^-}$ is obtained from the Monte Carlo simulation to be $(8.54 \pm 0.21) \times 10^{-3}$ for $M_{ee} > 470 MeV/c^2$ and $(2.85 \pm 0.12) \times 10^{-3}$ for $M_{ee} > 480 MeV/c^2$. An average particle identification efficiency for the $K_L^0 \to e^+e^-e^+e^-$ events is 0.719 ± 0.00547. With the branching ratio given in Ref.[25], then the number of events expected from the decay $K_L^0 \to e^+e^-e^+e^-$ is calculated to be 7.4 for $M_{ee} > 470 MeV/c^2$ and 2.5 for $M_{ee} > 480 MeV/c^2$.

The distribution of the vertex distance is examined for the high mass e^+e^- events and is found to be similar to that for the $K_L^0 \to e^+e^-e^+e^-$ events, as shown in Figure 5.11. This confirmed that the contamination from the accidental overlap of two decays and external conversion of gamma rays from the decays $K_L^0 \to \gamma\gamma$ and $K_L^0 \to ee\gamma$, which can make such high mass ee events, is very small.

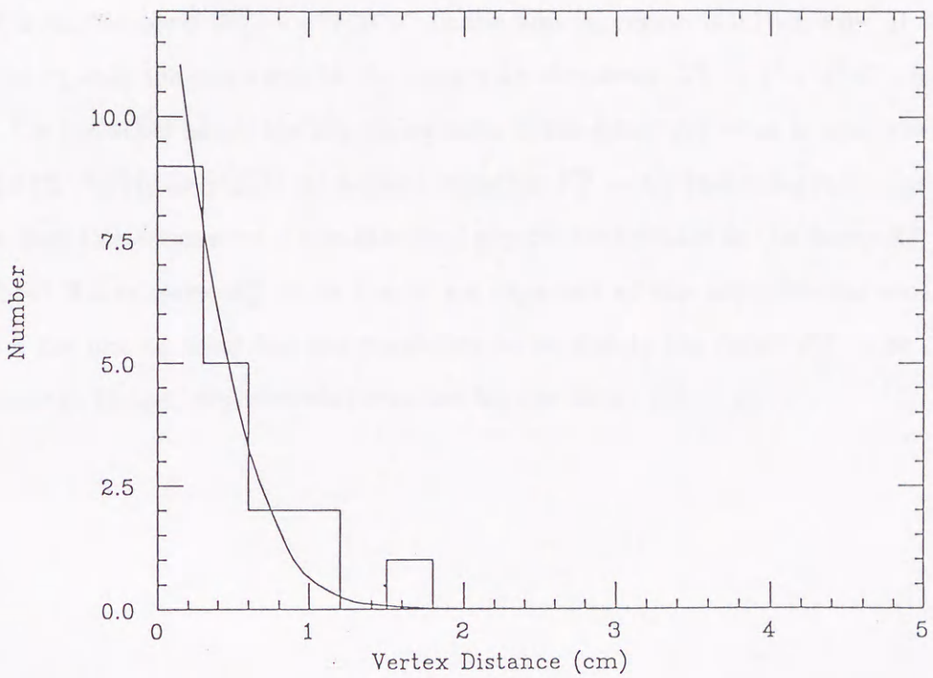

Figure 5.11: Distribution of the distance of closest approach of the two tracks for ee events with $M_{ee} > 470 MeV/c^2$.

The branching ratio of the decay $K_L^0 \to e^+e^-e^+e^-$ can be calculated using the 18 events in the region $M_{ee} > 470 MeV/c^2$. After subtracting the 4.3 events expected from the decay $K_L^0 \to ee\gamma$, it is obtained to be $(6 \pm 2 \pm 1) \times 10^{-8}$ for $M_{ee} > 470 MeV/c^2$ and $(7 \pm 3 \pm 1) \times 10^{-8}$ for $M_{ee} > 480 MeV/c^2$, respectively. The systematic uncertainty is estimated by the quadratic sum of the errors described below. There is 3% ambiguity in the acceptance calculation due to the Monte Carlo statistics, and 3% ambiguity in the particle identification. The ambiguity of the subtracted $K_L^0 \to ee\gamma$ yield is estimated to be 5% including both the statistical error of the acceptance calculation and the error contribution due to varying α_{K^*} within its experimental error. The branching ratio of the decay $K_L^0 \to e^+e^-e^+e^-$ is consistent within errors with that measured by NA31 and

E845[27] who have detected 2 and 6 events, respectively.

5.2.4 Discussion of the One ee Candidate Event in the Fiducial Region

Using the branching ratio obtained in the previous section, the number of events expected from the decay $K_L^0 \to e^+e^-e^+e^-$ in the fiducial region is 0.10 ± 0.04. It may be possible to explain the one event in the data with the decay $K_L^0 \to e^+e^-e^+e^-$, but it is difficult. On the other hand, the branching ratio of the decay $K_L^0 \to ee$ is estimated to be around 3×10^{-12}[7] from a QED calculation using the $K_L^0 \to \gamma\gamma$ branching ratio, and might be larger than this estimation if non-standard physics contributed to the decay $K_L^0 \to ee$. Then, about 0.1 or more $K_L^0 \to ee$ events are expected at this experimental sensitivity. Therefore, the one ee event has the possibility to be due to the decay $K_L^0 \to ee$, which may encourage further experimental searches for the decay $K_L^0 \to ee$.

Chapter 6

Conclusions and Future Prospects

6.1 Conclusions

A search for the $K_L^0 \to \mu e$ and $K_L^0 \to ee$ decays has been performed at the sensitivity of 4×10^{-11}. No $K_L^0 \to \mu e$ event has been observed, and a new upper limit of the branching ratio at the 90% confidence level has been given as,

$$B(K_L^0 \to \mu e) < 9.4 \times 10^{-11},$$

with a systematic error of 3%. The systematic error is very small because the sensitivity is determined by the ratio of two decay modes measured simultaneously using the same detector. We have been able to understand all the background events to $K_L^0 \to \mu e$ observed in this experiment. The events in the neighborhood of the fiducial region are expected from the decay $K_L^0 \to \pi e \nu$ whose pion has decayed into a muon in the spectrometer, while the other background from the double misidentification of $K_L^0 \to \pi e \nu$ is negligibly small. The background from the decay $K_L^0 \to \pi e \nu$ with the pion decaying can be reduced by the redundant measurement of the momentum to a small level compared to the sensitivity of this experiment. Using the upper limit obatined for the branching ratio of $K_L^0 \to \mu e$, the lower limit for the mass of the horizontal gauge boson can be set as $M_X > 71 GeV/c^2$

One ee event has been observed in the fiducial region. In the ee effective mass region $M_{ee} > 480 MeV/c^2$, five more events have been observed. They are expected mainly from the decay $K_L^0 \to e^+e^-e^+e^-$ according to the background study for $K_L^0 \to ee$. The one event in the fiducial region cannot be distinguished from the background events.

Therefore, a upper limit for the branching ratio of $K_L^0 \to ee$ has been determined to be,

$$B(K_L^0 \to ee) < 1.6 \times 10^{-10},$$

at 90% confidence level.

179 events of the decay $K_L^0 \to \mu\mu$ have also been also observed including 1.2 background events. Then the branching ratio of the decay $K_L^0 \to \mu\mu$ has been determined to be,

$$B(K_L^0 \to \mu\mu) = (7.9 \pm 0.6 \pm 0.3) \times 10^{-9},$$

where the first uncertainty is statistical and the second one is the systematic uncertainty. It agrees with all other experimental results within the errors.

6.2 Future Prospects

It is obvious that the three generations in the quark and lepton sectors exist, but this is not explained by the Standard Model. One of the unified schemes for explaining the number of generations will be to introduce a quantum number for the generation number and to make a multiplet such as $(G_1, G_2, G_3, ...)$ where G denotes the generation. Such a scheme leads to predictions of interactions between different generations and lepton flavour changing processes such as $K_L^0 \to \mu e$.

This provides a motivation for the searching for the decay $K_L^0 \to \mu e$ with the sensitivity higher than the present level. It suggests that experiments should be performed with a sensitivity at the level of $10^{-12} \sim 10^{-14}$. Such an experiment with a sensitivity of 10^{-12} will be performed at BNL from 1993 to 1994. Another experiment will be performed at the KAON factory which is proposed at Triumph in Canada, and whose construction has been approved recently. The proton intensity is one thousand times higher than that of the KEK-PS.

I have considered an experimental apparatus in the future to search for the decay $K_L^0 \to \mu e$. A detector should satisfy the following requirements for the experiment to be successful:

- suppressing background for the decay $K_L^0 \to \mu e$ from the decay $K_L^0 \to \pi e \nu$ followed by $\pi \to \mu\nu$ in the spectrometer, and that for the decay $K_L^0 \to ee$ from the decay $K_L^0 \to e^+e^-e^+e^-$;

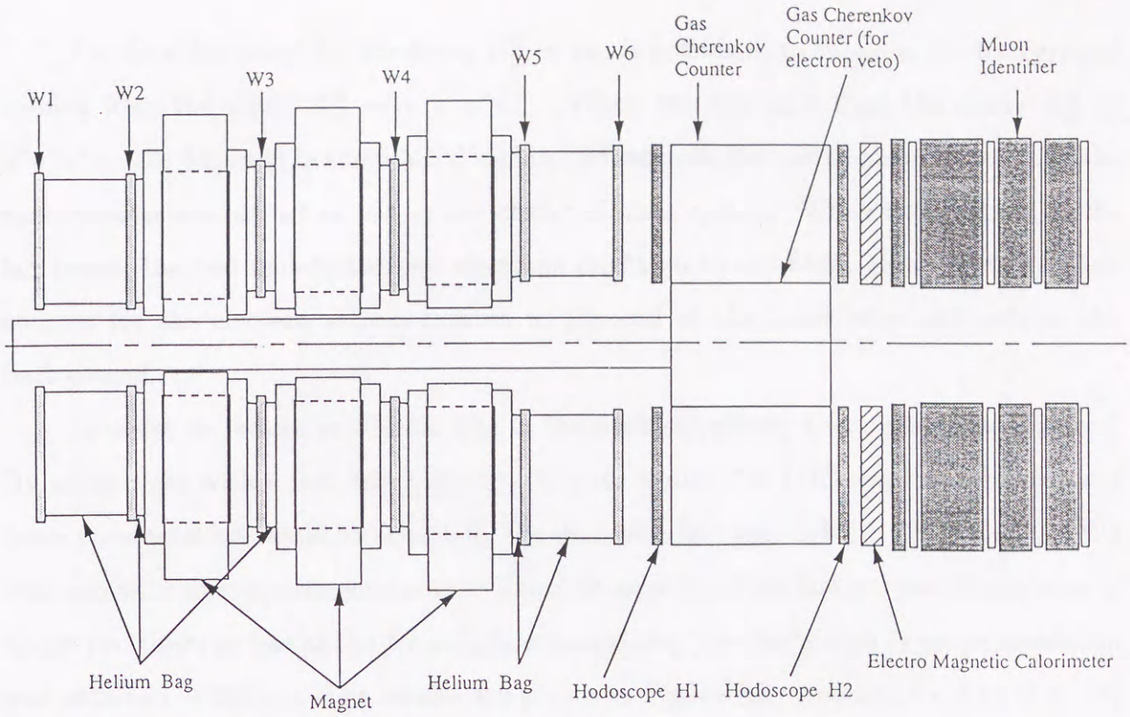

Figure 6.1: Plane view of the new detector system.

- reducing accidental hits in drift chambers leading to mistracking because the influence of track reconstruction errors cannot be completely suppressed by kinematical cuts;

It is indicated in this thesis that the background for the decay $K_L^0 \to \mu e$ comes from the decay $K_L^0 \to \pi e \nu$ with the pion decaying in the spectrometer. In order to suppress the background at the level of $10^{-13} \sim 10^{-14}$, the further redundant measurement of the momentum is desirable. The suppression might be accomplished by a triple-stage spectrometer as shown in Figure 6.1. The pion decaying in a magnet would lead to mismeasurement of the track, and this would produce background. Therefore, if the momentum is precisely measured using the other two magnets, the background will be reduced. The magnetic field of one magnet corresponds to a momentum kick of $238 MeV/c$, the first and third magnets have a same polarity, and second one has an opposite polarity. Then the momentum directions of leptons decaying in the direction nearly transverse to the K_L^0 beam are almost parallel to the z-axis after traversing the magnetic field. We can use a parallel trigger for the trigger system which is simple and has small acceptances for the main three-body decays.

On the other hand, for the decay $K_L^0 \to ee$, it is difficult to suppress the background coming from the decay $K_L^0 \to e^+e^-e^+e^-$. When two electrons from the decay $K_L^0 \to e^+e^-e^+e^-$ are detected in the fiducial region, the residual two electrons undetected by the spectrometer are almost at rest in the center of mass system. When transformed to the lab frame, the two undetected two electrons might go to the beam pipe. The Čerenkov counter for the electron veto is located at the end of the beam pipe and reduces the background.

In order to reduce accidental hits in the drift chambers, a fast gas might be used. By using a gas with a fast drift velocity, the gate width of a TDC can be narrowed, and fewer accidental hit would be accepted. We studyed a fast gas, $C_2H_6 + CF_4$, using the W3 chamber with this experimental setup. The drift velocity of the fast gas was $20\mu m/nsec$ of about two times as fast as the $Ar + C_2H_6$ gas mixture, however a slightly worse resolution was obtained $- 290\mu m$. The results are shown in Figure 6.2. Another solution is to use He gas. The He gas has some advantages. Since He has a low atomic number, the gas is insensitive to gammas, and the accidental hits might be able to decrease. Further we can reduce the material in the spectrometer by He, and obtain better mass resolution. However, the He gas also some disadvantages. The drift velocity is small and is half of that of the $Ar + C_2H_6$ gas, which increase accidental hits due to wider gate width. The collected charge is small due to the small atomic number, which causes to the worse chamber resolution.

It is essential to study the spectrometer and the chamber gas, and additionally, the electronics (which was not mentioned above) to obtain a sensitivity of 10^{-13} to 10^{-14}.

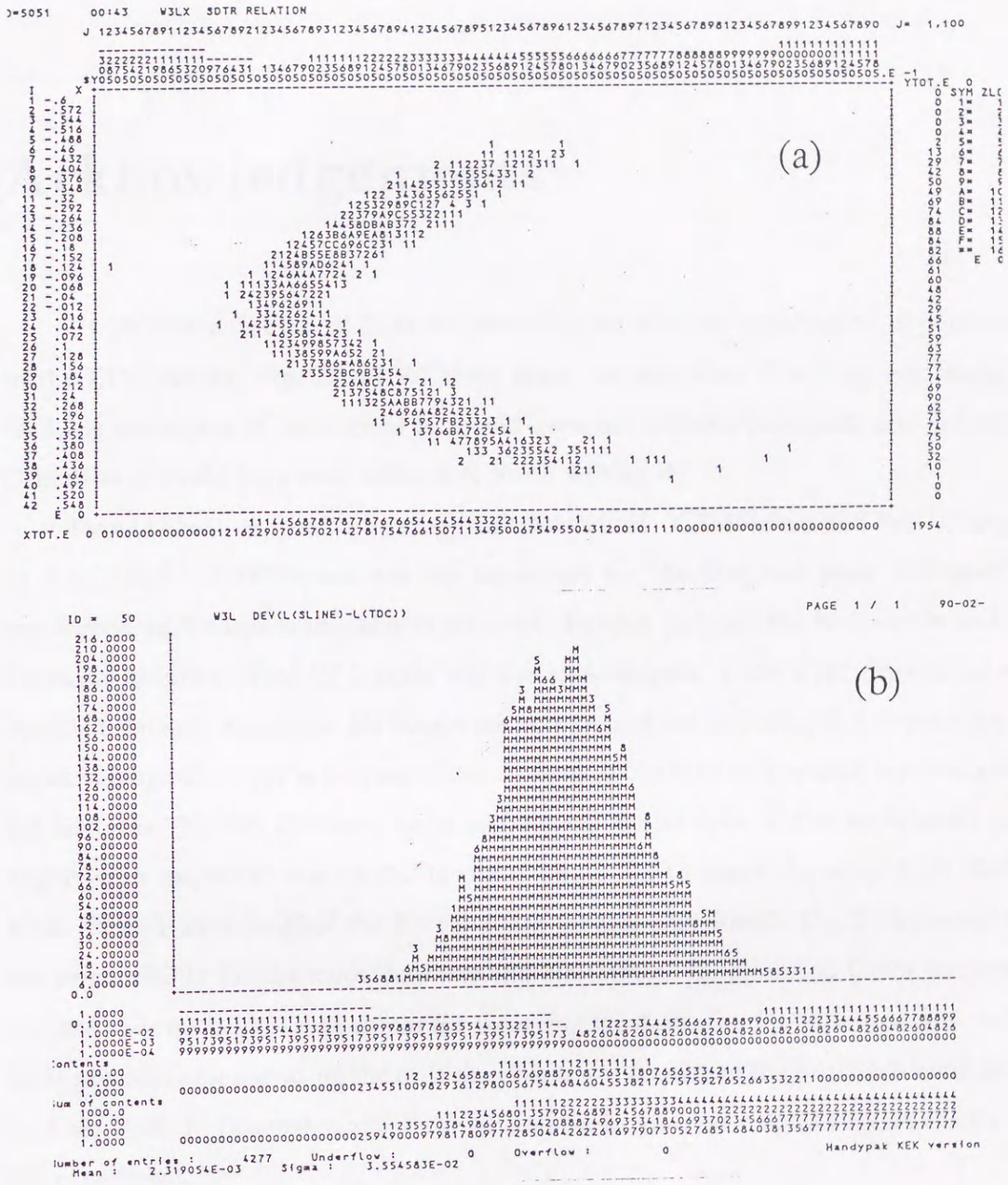

Figure 6.2: (a) $x - t$ distribution of a fast gas, $C_2H_6 + CF_4$, for which the drift velocity was determined to be $20\mu nsec$, and (b) distribution of the sum of drift lengths for which the resolution was determined to be $290\mu m$.

Acknowledgements

I wish to thank Prof. H.Yuta for providing me with an opportunity to participate in the E137 counter experiment for three years. In the stage of writing my thesis, he read the entire text in its original form and gave me valuable comments and criticisms. Otherwise it would have been difficult to finish writing it.

I would like to express my special gratitude to Prof. Y.Yoshimura and Prof. T.Inagaki at KEK. Prof. Y.Yoshimura was my supervisor for the first two years and gave me much good advice concerning this experiment. He also designed the hodoscopes and the Čerenkov counters. Prof. T.Inagaki was the spokesperson of the E137 experiment and designed the drift chambers. He taught me how to perform and analyze a counter experiment through the E137 experiment, and undertook the task of directing my research in the last year. He also discussed many problems of the analysis of this experiment thoroughly with me, which was helpful to me. I would like to thank the other E137 staff of KEK. Prof. T.Sato designed the K0 beam line for this experiment. Dr. T.Shinkawa took the responsibility for the muon counters and electronics. He discussed the analysis with me, and gave me helpful suggestions for analyzing the data. Dr. F.Suekane taught me the basic procedure for operating the drift chambers, and developed the electron identification routine. Prof. K.Takamatsu and Prof. M.Kobayashi gave me helpful suggestions during the experiment.

I would like to express my thanks to the collaborators of this experiment from the University of Tokyo and Kyoto University. First of all, I wish to thank Prof. S.S.Yamamoto for giving me helpful suggestions in performing this experiment. Dr. Y.Hemmi designed the shower counter. Dr. M.Kuze, who was the first doctoral candidate to write a doctor thesis in the experiment, introduced to me the guidelines of the experiment during the data taking, and made many efforts to establish the data-taking system and analysis

methods. Mr. T.K.Komatsubara calculated the drift chamber parameters every cycle and processed the enormous Monte Carlo data for calculating various corrections in the experiment. He also processed the unbelievably large number of data tapes which were acquired. Dr. T.Kishida discussed with me the analysis and physics of this experiment and gave me useful suggestions. I wish to thank Dr. F.Sai, Mr. K.Ishikawa and Mr. J.Toyoura for their efforts in the early stage of this experiment, and Mr. Fukuhisa for developing the online data taking system using 8mm video tape.

I am grateful to the operating crew of the KEK 12GeV PS and the members of the Beam-Channel and Counter-Hall Groups, the Electronics and On-line Groups, the Computing Center, the Mechanical Engineering Center at KEK for their indispensable assistance. I express my sincere gratitude to Prof. T.Nishikawa, Prof. H.Sugawara, Prof. K.Nakai, Prof. S.Iwata, and the members of the physics departments of KEK.

I would like to thank the members of the bubble chamber physics laboratory. My thanks are due to Prof. T.Kitagaki, Prof. S.Tanaka, Prof. A.Yamaguchi, Prof. K.Abe, Prof. K.Hasegawa, and Dr. T.Hayashino, who are the staff of the laboratory, for their encouragement. My special thanks are due to Prof. J.MacNaughton for reading my thesis and correcting long complicated sentences. I owe my thesis in English to his effort. Thanks are also due to Mrs. K.Taguchi, Mr. S.Chida and Mrs. Y.Nagai, who are office staff, Mr. T.Takayama, Mr. J.Katayama, Mr. H.Hanada, and Mr. T.Nakajima, who are technicians, Mrs K.Tamae and Miss Y.Suzuki, who are research assistants, for their support to my research. Furthermore, thanks are due to graduate and undergraduate students: Dr. H.Kurino, Dr. M.Sasaki, Mr. H.Suzuki, Mr. K.Sakai, Mr. R.Takahashi, Mr. H.Kawamoto, Mr. K.Neichi, Mr. Okuno, Mr. Y.Iwasaki, Mr. Y.Hasegawa, Mr. M.Ito, Mr. M.Ogura, Mr. M.Kuriki, Mr. K.Suzuki, Mr. T.Matsumoto, and etc. , for their support in making my doctor thesis. I express my appreciation to Dr. C.S.Lim, Dr. H.Murayama and Mr. S.Ishihara for their theoretical support.

Finally I would like to acknowledge the fellowship support provided by the Japan Scholarship Foundation, and JSPS Fellowship for Japanese Junior Scientists.

Appendix A

Theoretical Reviews for the Decay $K_L^0 \to \mu e$

In this appendix, some models are described which predict the decay $K_L^0 \to \mu e$ to be of the order of the experimentally achievable sensitivity.

A.1 Left-right Symmetric Model

In $SU(2)_L \otimes SU(2)_R \otimes U(1)_Y$ models, the decay $K_L^0 \to \mu e$ proceeds via a diagram as shown in Figure A.1 and its rate is not experimentally small due to the large Majorana masses for the right-handed neutrinos. But the branching ratio is still small because of the large mass of the right handed charged gauge boson W_R. If the left-right symmetry is exact, the branching ratio for the decay $K_L^0 \to \mu e$ is less than 10^{-15} for the bound on $M_{W_R} \geq 1.4 TeV$ constrained by the $K_L - K_S$ mass difference. However, with the relaxed bound of $300 GeV$ on M_{W_R} for broken left-right symmetry, one obtains a branching ratio less than 2×10^{-13} [1][2]. This mechanism also gives an enhancement to the rate of the decay $K_L^0 \to ee$.

A.2 Multiple Higgs Doublets

Another extension of the Standard Model which can lead to lepton flavor violation is to incorporate two Higgs doublets. Of the eight Higgs particles that occur with two

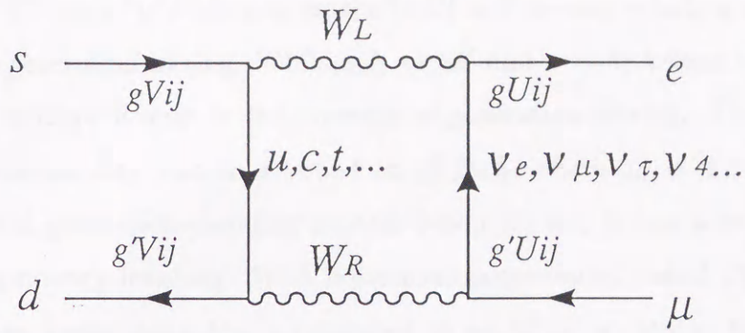

Figure A.1: $K_L^0 \to \mu e$ in the left-right model.

doublets, two charged particles and one neutral particle are eaten by the W and Z bosons through the usual Higgs mechanism. Two charged scalar particles and three neutral ones, which can induce lepton flavor violation, remain as physical particles. The decay $K_L^0 \to \mu e$ can occur through such Higgs particles with a diagram as shown in Figure A.2. Then, the branching ratio of $K_L^0 \to \mu e$ is estimated to be in the range 10^{-10} to 10^{-13} with the constraint coming from the $K_L - K_S$ mass difference [2].

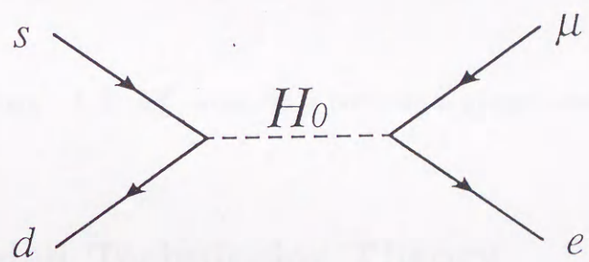

Figure A.2: $K_L^0 \to \mu e$ via multiple Higgs doublets.

A.3 Horizontal Gauge Symmetry

This model is constructed on the basis of a gauge symmetry connecting the different generations. The horizontal symmetry implies that the net generation numbers(G) are conserved in interactions. In the limit of vanishing "generation-mixing" angles, the generation number is well defined. The first generation consisting of (u, d, ν_e, e) has generation number$G = 1$; the second of (c, s, ν_μ, μ) has $G = 2$; the third of (t, b, ν_τ, τ) has $G = 3$. The generation changing processes may be classified according to their ΔG. The decays

$K_L^0 \to \mu e$ and $K^+ \to \pi^+ \mu^+ e^-$ belong to the $|\Delta G| = 0$ process which is allowed even in the limit of no generation mixing. While, $\mu N \to eN$ and $\mu \to 3e$ belong to the $|\Delta G| = 1$ process which is allowed only in the presence of generation mixing. The decay rate of above rare processes may lead to a bound on g_H^2/M_H^2, where g_H is the gauge coupling of the horizontal generation-changing neutral boson H, and it has a mass M_H due to spontaneous symmetry breaking. With horizontal gauge model linked CP-violation, the horizontal gauge boson mass M_H is estimated to be $5TeV < M_H < 66TeV$ from the magnitudes of the observed CP-violation and the $K_L - K_S$ mass difference. Then, the decay $K_L^0 \to \mu e$ is mediated by a horizontal gauge boson as shown in Figure A.3, and the branching ratio is expected to be greater than 10^{-10}[3].

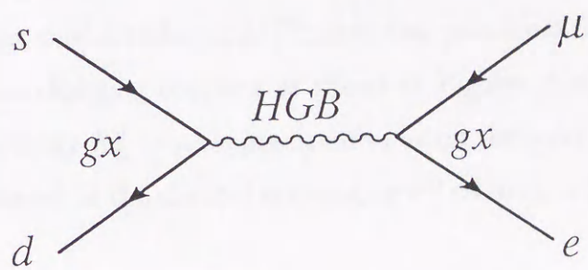

Figure A.3: $K_L^0 \to \mu e$ via a horizontal gauge boson.

A.4 Extended Technicolor Theory

The technicolor interaction scheme comes from the analogy to the $SU(3)$ color symmetry. In this scheme, elementary scalar fields such as Higgs are absent and instead of them new gauge interactions and new exotic fermions which are called technifermions are introduced to solve the gauge hierarchy problem. When the technicolor interactions become strong, the chiral flavor symmetry is spontaneously broken, and the technifermions pick up a vacuum expectation value Λ_{TC}^3 which is about $250GeV$. As a result of chiral symmetry breaking, one gets (pseudo-) Nambu-Goldstone bosons, namely technipions, which are bound technifermion and anti-technifermion pairs. The technipion takes place of the Higgs. But this dynamical symmetry breaking scheme itself runs into problems with large flavor changing neutral currents and small fermion masses. One solution is

to introduce additional "Extended" technicolor (ETC) interactions coupling between the ordinary fermions to technifermions. Then, the ordinary fermions get masses of order $(g_{ETC}/M_{ETC})^2\Lambda_{TC}^3$. The large hierarchy of fermion masses is supposed to be produced due to the ETC gauge bosons with different masses. However, the order of magnitude of flavor changing neutral currents cannot be narrowed down because of the hierarchy of ETC gauge boson masses. Generally, these ETC forces are accompanied by phenomenologically interesting "horizontal" extended technicolor (HETC) interactions between ordinary fermions like those shown in Figure A.4(a) , which may even include leptoquark gauge bosons of the Pati-Salam (PS) type as shown in Figure A.4(b) which change a quark into a lepton and vice versa. The decay $K_L^0 \rightarrow \mu e$ is mediated by these ETC and HETC vector bosons in Figure A.4(a), and the branching ratio is predicted to be on the order of 10^{-11}[4]. The light color singlet technipion, P^0, including pseudoscalar leptoquark bosons, P_{LQ}, induces the flavor changing coupling as shown in Figures A.4(c) and (d), and the branching ratio of the decay $K_L^0 \rightarrow \mu e$ is predicted to be on the order of 10^{-12}. The decay $K_L^0 \rightarrow ee$ may be enhanced in the channel exchanging P^0 relative to the decay $K_L^0 \rightarrow \mu e$.

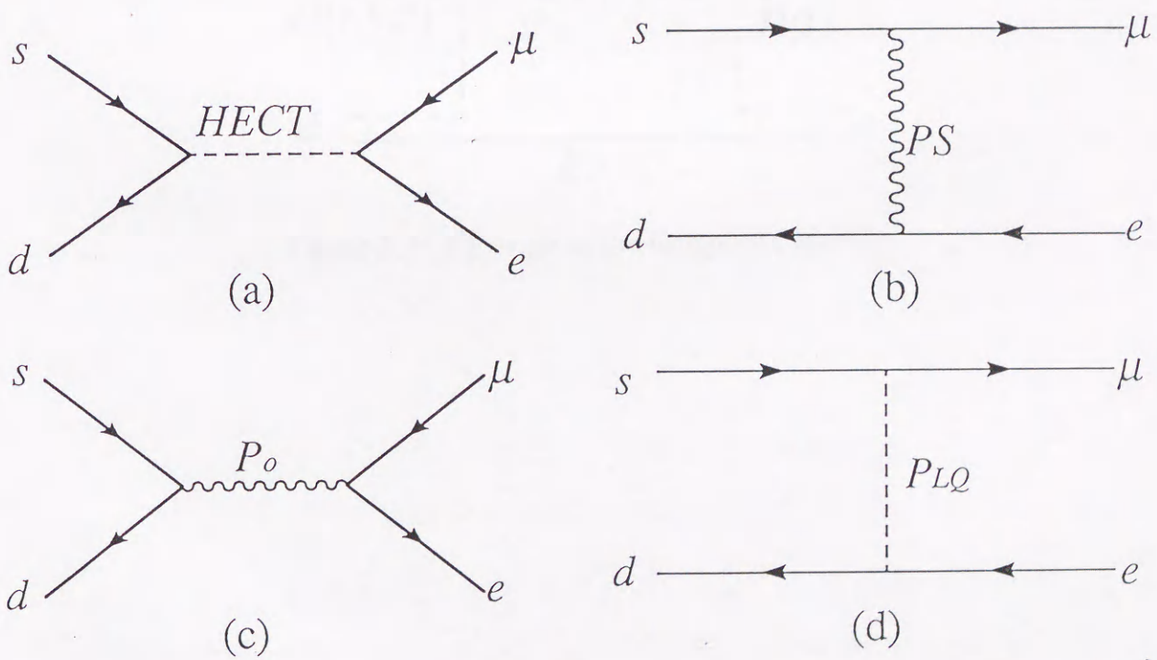

Figure A.4: $K_L^0 \rightarrow \mu e$ via (a) an ETC boson, (b)a leptoquark gauge bosons of the Pati-Salam, (c)a technipion and] (d) pseudoscalar leptoquark boson.

A.5 Composite Models

Composite Models of quarks and leptons provide a natural extension of the technicolor scheme to include the problem of the generations. In these models, quarks and leptons are replaced by more fundamental subconstituents, whose bound states can include multiple copies of quark and lepton generations. In principle, these models combine the merit of the natural family replication and dynamical symmetry breaking, through which the weak interaction scale is naturally protected against large radiative corrections. Generally, the composite models would be expected to induce lepton flavor violations through the exchange of massive composite states. In a specific model combining natural family replication with the automatic suppression of $\Delta S = 2$ processes, the decay $K_L^0 \to \mu e$ induced through the diagram shown in Figure A.5 is predicted to occur with a branching ratio of the order 10^{-11}[5].

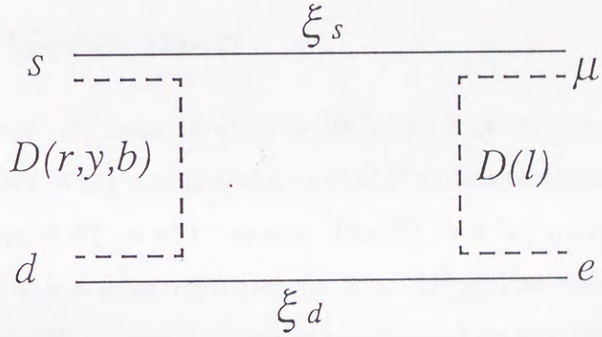

Figure A.5: $K_L^0 \to \mu e$ in the Composite Model.

Appendix B

Monte Carlo Simulation

The Monte Carlo simulation is described here. It consists of event generation and reconstruction.

B.1 Event Generation

The momentum of K_L^0 from $1GeV/c$ to $10GeV/c$ is generated according to a spectrum based on Sandford-Wang's empirical formula[17] and corrected by the experimentally obtained K_L^0 spectrum of $K_L^0 \to \pi^+\pi^-$ events. The $K_L^0 \to \pi^+\pi^-$ events are obtained from the data taken with a low intensity beam ($\sim 1 \times 10^{11} ppp$) to reduce intensity effects. The spectrum of the $K_L^0 \to \pi^+\pi^-$ events are compared to the Monte Carlo events of $K_L^0 \to \pi^+\pi^-$, and the difference is corrected with two cubic polynomials. Then the spectrum is given by

$$\begin{aligned} \frac{d\sigma}{dp} &= f(p) \cdot 3.22e^{(-0.136p)} \\ &\times (0.9823 + 0.0766p - 0.0327p^2 + 0.0033p^3) \\ &\times (0.9139 + 0.0730p - 0.0182p^2 + 0.0013p^3), \end{aligned} \tag{B.1}$$

where $p = p_{K_L}(MeV/c)/500(MeV/c)$, and $f(x)$ is given empirically. The K_L^0 's are generated in the Cu target uniformly, and the directions are determined by the collimator.

The K_L^0 decays are generated according to the K_L^0 lifetime and only decays within the decay chamber are accepted. The two-body decay occurs isotropically in the rest frame of K_L^0 and is Lorentz-transformed to the laboratory system. The daughter particles

are tracked in the spectrometer using the information on the measured magnetic field. The trajectories of the daughter particles are determined at 46 planes including the 20 chamber planes by a Runge-Kutta method. All the detector elements are realistically simulated and the multiple Coulomb scattering by the detector material is also taken into account. The scattering angle is simulated plane by plane with the formula as:

$$\theta_0 = \frac{13.6MeV}{p\beta} z\sqrt{t}\,[1 + 0.38\ln(t)]\,, \tag{B.2}$$

where p, β and z are the momentum (in MeV/c), velocity and charge number of the particle, and t is the thickness of the material measured in units of radiation lengths. Since the tail of the scattering angle distribution cannot be perfectly simulated due to the very thin material between two planes, we introduce a correction for θ_0 called the Molieré tail[28]. The correction factor is given by $1/\sqrt{1/2(1-1.2/B)}$, where B depends on the material. The trajectories of the daughter particles are extrapolated to trigger counters and events satisfying the trigger conditions are accepted. The responses of the particle identification counters are not simulated.

B.2 Event Reconstruction

When the trajectories of the daughter particles are determined, they are converted into the actual data format for reconstruction with the drift chamber resolution obtained from the experimental data. Then actual data of accidental hits are superimposed on the Monte Carlo events. They were collected as events triggered periodically unassociated with the actual event triggers. They lead to mistakes in tracking, and the mistracking is included in the Monte Carlo. A chamber signal is often destroyed or disappears due to an accidental hit (false signal) occupying the true signal, so-called "occupation". If the noise signal comes before the true signal, the drift time will be shortened. The occupation causes the true signal to disappear if the following conditions are satisfied simultaneously:

1. the false signal come at the same time as the chamber gate start, then the TDC does not work correctly,

2. the false signal is near the true signal within $\Delta W + 10nsec$, where ΔW denotes the pulse width.

The counting rate of the drift chamber is about $1M_{Hz}$ for the hottest wire. A TDC in the TKO crate TDC starts with the chamber signal and stops with the common signal made from the delayed master trigger. The start signal is accepted only within a gate width of $175nsec$ which also comes from the master trigger. The model scheme is shown in Figure B.1. A signal which comes at the same time as the gate start is not accepted which decrease the counting rate of the chambers. In the Monte Carlo simulation, the start time of an accidental signal is taken to be earlier by one pulse width than the start time of the TDC information of the real data. The pulse width is taken as $160nsec$ in this simulation. The Monte Carlo data, on which the accidental hits are superimposed, are reconstructed by the same tracking procedure used in the actual analysis. Finally the kinematical variables are obtained and the events are checked by the selection criteria.

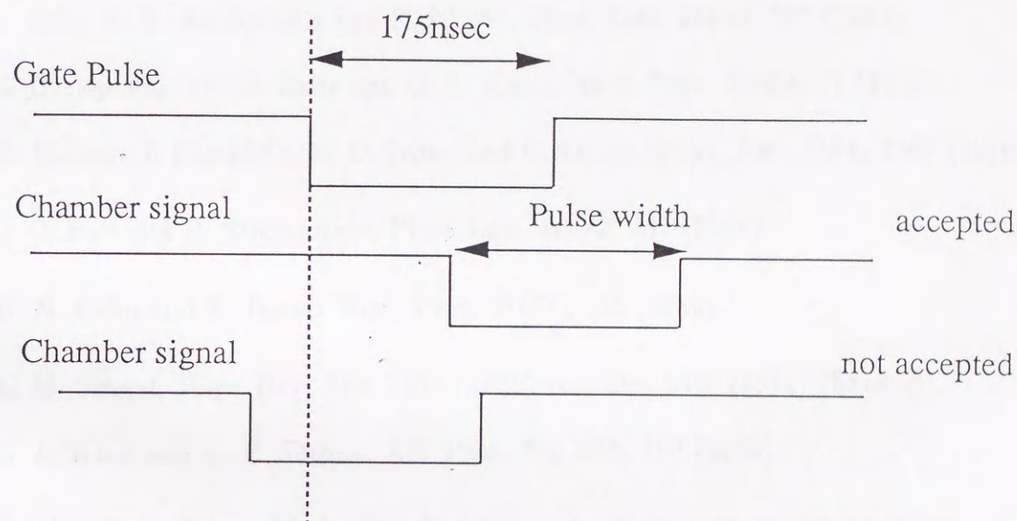

Figure B.1: Model scheme of occupation.

References

[1] P. Langacker, S. U. Sankar and K. Schlicher, Phys. Rev. **D38**, 2841 (1988).

[2] A. Barroso, G. C. Branco and M. C. Bento, Phys. Lett. **B134**, 123 (1984).

[3] W.-S. Hou and A. Soni, Phys. Rev. Lett. **54**, 2083 (1985).

[4] J. Ellis, D. V. Nanopoulos and P. Sikivie, Phys. Lett. **B101**, 387 (1981);
S. Dimopoulos and S. Raby and G. L. Kane, Nucl. Phys. **B182**, 77 (1981);
E. Eichten, I. Hinchliffe, K. D. Lane, and C. Quigg, Phys. Rev. **D34**, 1547 (1986).

[5] J. C. Pati and H. Stremnitzer, Phys. Lett. **B172**, 441 (1986).

[6] R. N. Cahn and H. Harari Nucl. Phys. **B176**, 135 (1980).

[7] L. M. Sehgal, Phys. Rev. **183**, 1511 (1969) and **D4**, 1582 (1971) (Errata);
G. L. Kane and R. E. Shrock, AIP Proc. No. **102**, 123 (1983).

[8] Particle Data Group, M. Aguilar-Benitez *et al.*, Phys. Lett. **B170**, 14 (1986).

[9] V. L. Fitch *et al.*, Phys. Rev. **164**, 1711 (1967).

[10] A. R. Clark *et al.*, Phys. Rev. Lett. **26**, 1667 (1971).

[11] W. C. Carithers *et al.*, Phys. Rev. Lett. **30**, 1336 (1973);
W. C. Carithers *et al.*, Phys. Rev. Lett. **31**, 1025 (1973);
Y. Fukushima *et al.*, Phys. Rev. Lett. **36**, 348 (1976);
M. J. Shochet *et al.*, Phys. Rev. **D19**, 1965 (1979).

[12] S. F. Schaffner *et al.*, Phys. Rev. **D39**, 990 (1989).

[13] E. Jastrzembski *et al.*, Phys. Rev. Lett. **61**, 2300 (1988).

[14] C.Mathiazhagan *et al.*, Phys. Rev. Lett. **63**, 2181 (1989);
C.Mathiazhagan *et al.*, Phys. Rev. Lett. **63**, 2185 (1989).

[15] T. Inagaki *et al.*, Phys. Rev. **D40**, 1712 (1989).

[16] T. Akagi *et al.*, Phys. Rev. Lett. **4**, 2614 (1991);
T. Akagi *et al.*, Phys. Rev. Lett. **4**, 2618 (1991).

[17] J. R. Sanford and C. L. Wang, BNL reports **11279** and **11479** (*unpublished*) (1967).

[18] H. Wind, Nucl. Instr. and Meth. **115**, 431 (1974).

[19] T. K. Komatsubara, Master Thesis, Univ. of Tokyo (*in Japanese*) (1989).

[20] M. Kuze, Doctor Thesis, Univ. of Tokyo (1990).

[21] P. A. Aarnio, J. Ranft and G. R. Stevenson, CERN Internal Report TIS-RP/106-Rev (1984).

[22] A. P. Heinson *et al.*, Phys. Rev. **D44**, R1 (1991).

[23] G. D. Barr *et al.*, Phys. Lett. **B240**, 283 (1990);
K. E. Ohl *et al.*, Phys. Rev. Lett. **65**, 1407 (1990).

[24] L. Bergström, E. Massó, P. Singer, Phys. Lett. **B131**, 229 (1983).

[25] N. M. Kroll and W. Wada, Phys. Rev. **98**, 1355 (1955);
T. Miyazaki and E. Takasugi, Phys. Rev. **D8**, 2051 (1973).

[26] N. P. Samios *et al.*, Phys. Rev. **126**, 1844 (1962).

[27] G. D. Barr *et al.*, Phys. Lett. **B259**, 389 (1991);
W. M. Morse *et al.*, BNL reports **46282** (*unpublished*) (1991).

[28] J. B. Marion and B. A. Zimmerman, Nucl. Instr. and Meth. **51**, 93 (1967).

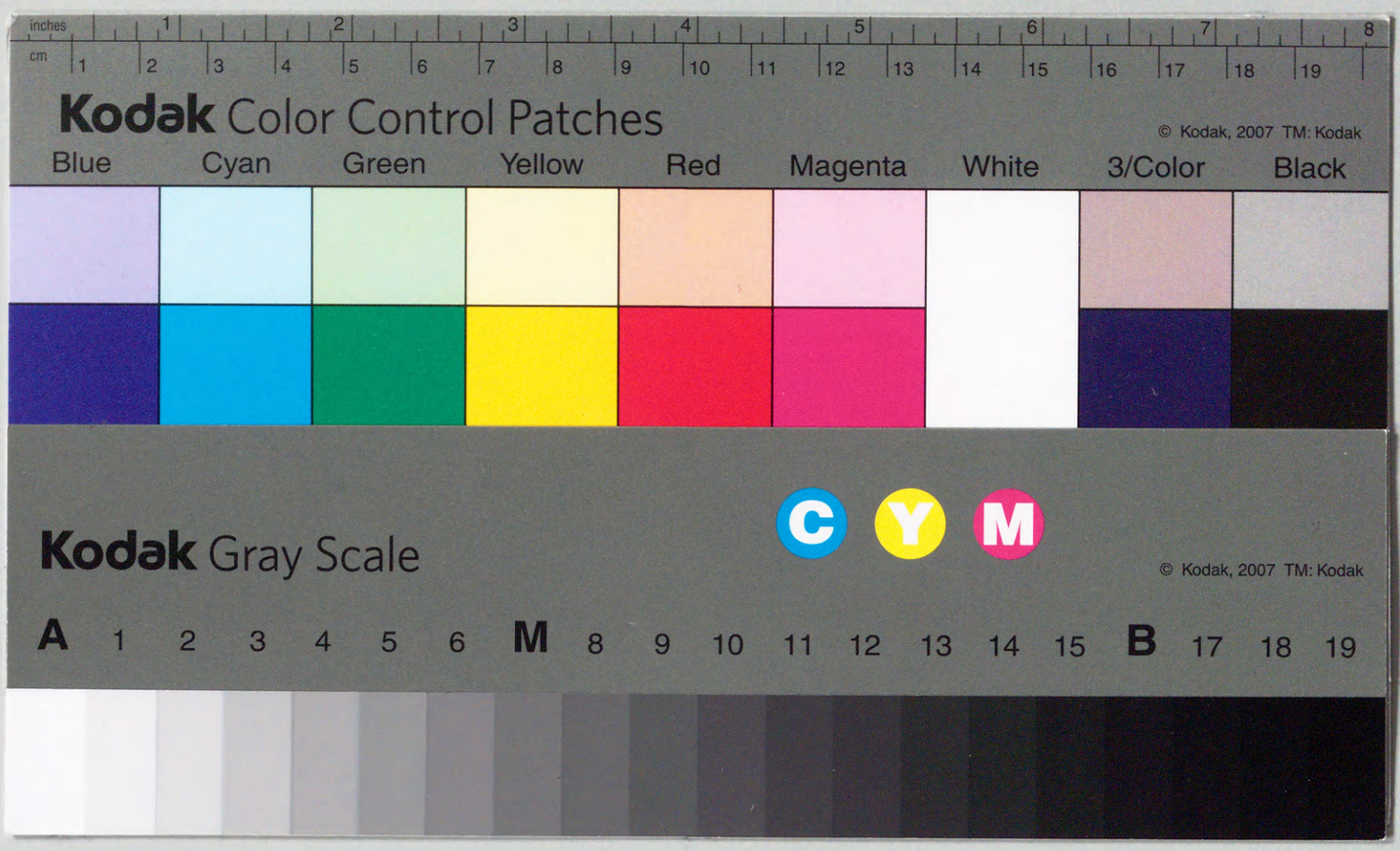
inches
cm
Kodak Color Control Patches
© Kodak, 2007 TM: Kodak
Blue
Cyan
Green
Yellow
Red
Magenta
White
3/Color
Black
Kodak Gray Scale
C
Y
M
© Kodak, 2007 TM: Kodak
A 1 2 3 4 5 6 M 8 9 10 11 12 13 14 15 B 17 18 19